CORROSION OF REINFORCING STEEL IN CRACKED CONCRETE

by

MINGDONG BI

A dissertation submitted to the Graduate Faculty in Engineering in partial fulfillment of the requirements for the degree of Doctor of Philosophy, The City University of New York

2008

This manuscript has been read and accepted for the
Graduate Faculty in Engineering in satisfaction of the
dissertation requirement for the degree of Doctor of Philosophy.

Prof. Kolluru V. Subramaniam

Date	Chair of Examining Committee

Dean Mumtaz Kassir

Date	Executive Officer

Prof. Michel Ghosn

Prof. Anil K. Agrawal

Prof. Fengbao Lin

Prof. Ronald L. Birke

Supervision Committee

THE CITY UNIVERSITY OF NEW YORK

ABSTRACT

CORROSION OF REINFORCING STEEL IN CRACKED CONCRETE

by

MINGDONG BI

Advisor: Prof. Kolluru. V. Subramaniam

Cracks are often produced in concrete structures due to the action of loads or for other reasons such as restrained shrinkage and thermal movements. Once a crack is formed, it provides an easy and fast access for ingress of ions to the steel surface. A crack in concrete also introduces spatial variations in the concentrations of oxygen and chloride ions at the steel surface, which results in a spatial inhomogeneity in the state of steel along the length of the rebar. Predicting the rate of corrosion of steel in cracked concrete is therefore particularly challenging and conventional electrochemical techniques tend to under-predict the rate of corrosion.

The main objective of this research is to investigate the influence of a crack in concrete on the corrosion of a steel bar. The mechanism of corrosion in a steel bar which is intersected by a crack along its length is investigated using beam specimens. A representation of the macrocell corrosion system, which forms along the length of the steel bar, is developed using an Evans diagram considering the Tafel polarization responses of active and passive steel in concrete. A fundamental relationship between the

local microcell and macrocell corrosion rates which result in metal loss at the crack is developed using the Evans diagram representation of the system. An equivalent distributed element circuit model for the system is developed to predict the rate of steel corrosion. The proposed circuit model is shown to provide reasonable prediction of the macrocell corrosion in cracked concrete.

Results of an experimental program investigating the polarization response of steel in cracked concrete are reported. The equivalent circuit model provides favorable prediction of the current distribution in the specimen. An implementation procedure for the proposed circuit model for predicting the rate of corrosion of steel in cracked concrete from a polarization test is developed. A practical approach to obtain the area of anode and the macrocell corrosion rate in the field measurements is presented.

This thesis is for my father, YuanShan Bi, the memory of my mother, WeiBing Wang, my wife, Shenghong and my daughter, Amelie

ACKNOWLEDGMENTS

I would like to express my gratitude to my mentor, Prof. Kolluru V. Subramaniam, for his guidance, support and encouragement throughout my entire PhD study and the writing of the thesis. The thesis could not have been completed without his inspiration, criticism and his guidance to explore the complex problem, identify the key factors and turn into practical steps. Those experiences will benefit me not only in my PhD study, but also in my future career path.

I would like to thank my wife Shenghong, my father and my mother for their encouragement and support. They are the motivation for me to complete the thesis.

I would like to thank Prof. Anil Agrawal for providing some of the experimental instruments and Prof. Ronald Birke for his instruction about electrochemistry.

I would like to thank my officemates and friends, Mr. Marco Frias, Dr. Jaejun Lee, Mr. Weimin Nian, Mr. Hadi Kamyab, Mr. Xiaojun Wang, Dr. Minwei Gong and Dr. Sheng Lu for their help and support in laboratory work and discussion.

TABLE OF CONTENTS

LIST OF TABLES

LIST OF FIGURES

CHAPTER 1
INTRODUCTION

1.1 BACKGROUND

Reinforced concrete is the most widely used construction material especially in transportation infrastructure. The value of concrete structures in the United States is estimated to be six trillion dollars. Yet, many of these concrete structures, especially highway bridges, exhibit early deterioration caused by corrosion. Corrosion damage in reinforced concrete is estimated to be a multi-billion dollar problem in the United States and is the leading factor contributing to the deterioration of the nation's highway infrastructure. In 2001, Federal Highway Administration (FHWA) reported that the total direct cost of corrosion was $279 billion per year (Report FHWA-RD-01-156, 2001), which is 3.2 percent of the U.S. gross domestic product (GDP). In 1997, it was estimated that the cost of corrosion damage in US highway bridges exceeded $150 billion. In 1991, the transportation research board (TRB) estimated the cost of repairing and protecting concrete bridge decks and parking garages from steel corrosion to be in the range of $200 - $500 million per year (Transportation research board special report 235, 1991). In the United Kingdom, the cost of maintaining the highways and bridges is about $225 million per year. In Europe, about $1.6 billion is spent every year to deal with the

problem of corrosion of steel reinforcement (Arya 1994). The annual expenditure for repair and rehabilitation of concrete structures in the 1990s exceeded fifty percent of the total construction costs (Mailvaganam 1996) and it is expected that this trend will continue in the future. Detection and characterization of corrosion of steel in concrete, therefore, is very important for the condition assessment and initiation of timely repairs in reinforced concrete structures.

Previous research on corrosion of steel reinforcement in concrete has primarily focused on initiation and propagation of corrosion in uncracked concrete. The factors influencing corrosion and the methods for determining the rate of corrosion of steel embedded in concrete have been extensively researched (Alonso, 1998; Andrade, 1978; Ayra, 1995, 1996; Broomfield, 1997; Carino, 1999; Elsener, 2002, 2001, 1995, 1998; Feliu, 1998, 1989, 1986; Gonzalez, 1996, 1985; John, 1981; Gu, 2000; Raupach, 1996, 1996; Schiessl, 1989; Stern and Geary, 1957; Tuutti, 1982). In these studies, it is implicitly assumed that concrete cracking is the result of expansion stresses due to corrosion product. The alkalinity of concrete provides good chemical protection to steel against corrosion. Therefore, in the absence of a crack, the steel reinforcement in reinforced concrete structures usually exhibits a prolonged corrosion initiation period. However, non-corrosion related cracks are often found in concrete structures. These cracks are introduced due to the action of loads, restrained shrinkage or thermal gradients. Once a crack is formed in reinforced concrete (Borgard et al, 1989), it provides an easy and fast access for ingress of ions such as chlorides, oxygen and water to the steel surface.

Steel in the crack zone is thus readily depassivated. Further, once corrosion is initiated, the continued loading of the structure produces repeated opening and closing of the crack, thereby potentially influencing the corrosion rate. Relatively little work has been done to study corrosion of steel embedded in cracked concrete. Available literature suggests that the corrosion of steel is non-uniform along the length of the bar and the rate of metal loss at the crack is influenced by parameters away from the crack. A clear understanding of the corrosion process in such a situation and the influence of the different variables on the local rate of metal loss at the crack are currently lacking. Application of established methods such as linear polarization resistance measurement have been shown to be unreliable for predicting the rate of corrosion because of problems associated with interpretation of the test data. Application of established procedures for predicting the rate of corrosion often leads to severely underestimating of the local corrosion rate. Models which allow for interpreting results of external polarization and provide estimates of rate of metal loss are currently not available. This gap in the existing knowledge provides motivation for the study outlined in this dissertation, which is focused on investigating the corrosion of steel in cracked concrete.

1.2. RESEARCH OBJECTIVES AND SCOPE

The main objective of this study is to investigate the corrosion of steel in cracked concrete. A fundamental understanding of the corrosion of steel in cracked reinforced concrete will be developed to establish the mechanism of charge transfer and metal loss due to corrosion in this system. The spatial and temporal variation of corrosion potential

and corrosion current, the ratio of macrocell/microcell corrosion components and the distribution and type of corrosion products will be determined. A test procedure for on-site measurement of the corrosion rate of reinforcement in cracked concrete will be established.

1.3. OUTLINE OF THE DISSERTATION

A study of the corrosion of steel in cracked concrete is proposed, which leads to achieve the above-stated research objects. The study will involve: (a) a review of the literature on the state-of-the-art on monitoring corrosion of reinforcement in concrete, with or without a crack; (b) an experimental investigation to provide a direct experimental determination of a circuit representation for the steel-concrete interface using measurements at the steel surface and embedded near steel-concrete interface; (c) an experimental investigation evaluation of macrocell and microcell rates using Tafel response; (d) A equivalent circuit model to predict the macrocell corrosion rate and simulate the spatial variation of the macrocell system. (e) An experimental program investigating the polarization response of steel in cracked concrete and a practical approach to obtain the area of anode and the macrocell corrosion rate in the field measurement. The brief description of the proposed research work is summarized in the following paragraphs.

Chapter 2: Literature Review. This chapter presents a review of the state-of-the-art in corrosion of reinforcement in concrete, with or without a crack. The literature review is divided into three main sections: (a) the first section reviews the cause, processes

involved, electrochemical nature and mechanism of corrosion in concrete; (b) the second section reviews methods/techniques used to investigate corrosion and determine the rate; (c) the third section reviews the existing literature on the influence of crack on the corrosion of steel in concrete.

Chapter 3: Experiments in uncracked concrete: CPE (Constant Phase Element) behavior of steel-concrete interface. This chapter aims to provide a direct experimental determination of a circuit representation for the steel-concrete interface using measurements from a reference electrode at the concrete surface and an embedded electrode near steel-concrete interface. From simultaneous potential measurements on the concrete surface and at the steel-concrete interface, an equivalent circuit representation is developed for the steel-concrete interface. A parallel combination of charge transfer resistance and a constant phase element (CPE) to represent the double layer capacitance is found to be suitable for both active and passive steel. It is shown that concrete has significant influence on the impedance spectrum measured from the concrete surface at both the low and the high frequencies. The steel-concrete interface presented CPE predominantly contributes in the low frequency.

Chapter 4: Corrosion in cracked concrete: Evaluation of macrocell and microcell rates using Tafel response. In this chapter, the results of an experimental investigation of the macrocell corrosion system in steel bar embedded inside cracked concrete are presented. The magnitudes of the microcell and macrocell mechanisms in a macrocell system are determined in terms of the fundamental electrochemical principles. A

representation of the macrocell corrosion system is developed using the polarization responses of active and passive steel in concrete in Evan diagram. The predicted state of the system is shown to compare favorably with the experimental result.

Chapter 5: Model of Corrosion in Cracked Concrete. A distributed element equivalent circuit is presented to simulate the spatial variations of current and potential in the macrocell system. A variable polarization resistance is introduced to capture the real behavior of the steel-concrete interface which is removed from its rest potential. The proposed circuit model provides favorable prediction of the macrocell corrosion in cracked concrete. From a parametric analysis, key factors which influence the formation and state of macrocell are identified. It is shown that concrete resistivity determines the magnitude and the physical extent of the macrocell corrosion mechanism.

Chapter 6: Polarization of macrocell. Results of an experimental program investigating the polarization response of steel in cracked concrete are reported. The results of polarization are predicted using the equivalent circuit model for the macrocell corrosion system. It is shown that interpretation of LPR data assuming uniform corrosion would severely underestimate the local corrosion rate. A practical approach for field implementation the equivalent circuit model to predict the LPR response of a macrocell corrosion system is developed. The proposed approach for implementing the equivalent circuit model provides reasonable estimates of metal loss and presents a significant advancement of the current state of the art. This represents a considerable contribution of the work presented in this thesis.

Chapter 7: Conclusions. The main conclusions of the work presented in this dissertation are summarized. The original contribution of the work, which represents advancement of our current understanding of corrosion in macrocell systems, is highlighted. Areas of future research, which emerge from this work, are discussed.

CHAPTER 2

LITERATURE REVIEW

2.1 INTRODUCTION

Reinforced concrete is one of the most utilized building materials because it offers several advantages such as high strength, durability and low-cost. Many facilities and structures, such as buildings, bridges, highways, factories, dams and marine structures, are built using reinforced concrete. As a material that offers good long-term performance, reinforced concrete is expected to last for decades. However, it is not always possible to prevent concrete from deteriorating, especially due to the corrosion of steel reinforcements in concrete. Insufficient concrete cover, poor design or workmanship, and the presence of aggressive agents can all potentially lead to corrosion of the steel rebar.

2.2 CAUSE, PROCESS AND MECHANISM OF CORROSION IN CONCRETE

2.2.1 Process and Mechanism

Corrosion is the result of a chemical reaction between a metal and its environment. Tuutti (1982) differentiated two distinct stages in the corrosion of steel in the concrete: the

initiation period, which involves the ingress of aggressive ions from environment into concrete, and the propagation stage, which involves the metal loss resulting from the corrosion process.

2.2.1.1 Initiation Period

Corrosion of a steel bar embedded in concrete is different from the corrosion of steel in air. Steel bars embedded in concrete are protected against corrosion by both physical and chemical barriers (Aligizaki, 1999). Concrete contains a highly alkaline solution (pH 12~13) within the pores of the hardened cement paste that surrounds the aggregate particles and the reinforcement. The pore solution normally also contains a significant amount of oxygen. The high alkalinity of the pore solution is due to the presence of sodium, potassium and calcium hydroxides derived from reaction between the mixing water and the cement particles. In this alkaline environment, a protective iron oxide film forms which adhere strongly to the steel surface and maintains the steel bars in a passive condition with an insignificantly low corrosion rate. This protected state of steel in concrete against corrosion is known as passivity. Passivity requires a minimum pH value approximately 11.5 to be maintained. The quality and the thickness of concrete cover affect the stability of the passive layer around the reinforcement. The loss of passivity is often a result of the loss of alkalinity of the surrounding concrete or the presence of chloride ions. These two factors are discussed in detail in the subsequent section.

(a) Carbonation

Carbonation results in a decrease in the alkalinity and hence causes an overall drop in the pH of the concrete surrounding the steel. Carbonation involves diffusion of carbon dioxide (CO_2) from the surrounding air into concrete. The reaction of CO_2 with the cement paste compounds in the presence of water results in the consumption of $Ca(OH)_2$ and hence an overall decrease in the pH (Schiessl 1989). This is given as:

$$Ca(OH)_2 + CO_2 \rightarrow CaCO_3 + H_2O$$

Since concrete is a porous material, the diffusion of CO_2 into concrete is determined by the pore structure of the cementitious phase and the humidity inside concrete. If the concrete pores are dry, diffusion of CO_2 does not result in carbonation. On the other hand, if the pores are filled with water, there is hardly any carbonation because of the low diffusion rate of CO_2 in water (diffusion rate of CO_2 is about 10^4 times lower in water than in air). If the pores are only partly filled with water, which is normally the case close to the concrete surface, carbonation proceeds rapidly to the depth at which the concrete pores are filled with water.

(b) Chloride Attack.

The chloride ions break down the protective oxide film at localized sites on the steel surface and results in pitting corrosion. The exact mechanism of breakdown of passivity by chloride ions is still a topic of research. One theory suggests that chloride ions penetrate the oxide film through pores or defects easier than other ions (Uhlig, 1985). According to another theory Cl^- ions colloidally disperse the oxide film and increase its permeability

(Uhlig, 1985). The theory proposed by Uhlig suggested that the absorbed chloride ions increase the exchange current and decrease the overpotential for anodic dissolution (Uhlig, 1985).

There are several sources of chloride ions in reinforced concrete structures. They are sometimes cast into the concrete (with mixing water, aggregate, setting accelerators) or they can be from the environment and diffuse into concrete (deicing salts, sea water etc). The mechanism of pitting corrosion has been described by various models and most recently by the point defect model, developed by Macdonald, (1992). The chloride ion attacks the passive layer but, unlike carbonation, there is no overall drop in pH. Chloride ions act as a catalyst to corrosion when they are present in sufficient concentrations at the rebar surface to break down the passive layer. They are not consumed in the process but help to break down the passive layer of oxide on the steel and allow the corrosion process to proceed quickly. This illustrated in Figure 2-1.

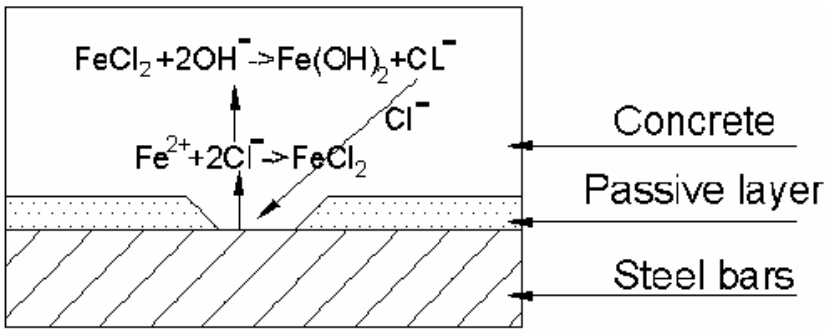

Figure 2-1: Chloride attack and chloride recycle

2.2.1.2 Propagation Period

The propagation period starts after depassivation of the steel oxide layer. The corrosion of steel reinforcement results in a reduction in the cross sectional area of steel and the formation of corrosion products on the surface of steel.

2.2.2 Electrochemical Nature of Corrosion

The corrosion processes involve chemical reactions and electronic charge transfer between the metal and its environment. Such reactions are known as electrochemical reactions. A brief review of the different reactions introduced in the corrosion of steel is provided in the next few sections.

2.2.2.1 Half Cell Reaction

When a piece of metal is immersed in a solution, a potential difference arises at the liquid/solid interface (Ramachandran and Beaudoin 2001). This is because of the uneven charge distribution in both solid and liquid phases. It is impossible to determine the absolute value of the potential difference at single interface; therefore, a second electrode must be introduced to complete an electrical circuit. The potential measured across the two electrodes is called the cell potential, which is the sum of two half-cell potentials.

Considering iron dissolution in an acid. The cell reaction is written as:

$$Fe + 2H^{+} \rightarrow Fe^{++} + H_2$$

The above reaction represents summation of the following two half-cell reactions:

$2H^{+} + 2e^{-} \rightarrow H_2$ Cathodic reaction

$Fe \rightarrow Fe^{++} + 2e^{-}$ Anodic reaction

A fixed potential difference can be obtained with reference to a so-called reference electrode that has a half-cell potential defined as zero. The half-cell potential of a system in which the reaction is not at unit activity can be easily calculated from the Nernst equation as follows:

For reaction: $O + ne^{-} \leftrightarrow R$

$$E = E^{0} + \frac{RT}{nF}\ln\left(\frac{C_O}{C_R}\right)$$

where E is the half-cell potential, E_0 is the standard half-cell potential, R is the gas constant, T is absolute temperature, n is the number of electrodes transferred, F is Faraday's constant and C_O, C_R are the concentrations of species O and R. (Ramachandran and Beaudoin 2001)

Cathodic current occurs when reduction takes place at the working electrode. If the working electrode potential is driven negative from equilibrium potential, a cathodic current will be created. The polarity of the cathodic current is usually considered to be negative.

2.2.2.2 Butler-Volmer Equation

Considering an iron half-cell reaction, e.g. an iron electrode in a solution containing ferrous ions, two reactions will likely happen: the Fe atoms dissolve into the solution and ferrous ions in the solution deposit back to the solid phase:

$$Fe \Leftrightarrow Fe^{2+} + 2e^{-}$$

The forward (rightward) reaction is the anodic reaction since it represents an oxidation process, and the backward (leftward) reaction is the cathodic reaction since it is a reduction reaction. If no external potential is applied, the iron electrode/ferrous solution system will reach equilibrium when the anodic reaction rate is equal to the cathodic reaction or:

$$i_o = i_{(anodic)} = i_{(cathodic)}$$

where i_o is the exchange current density (Ramachandran and Beaudoin 2001). The corresponding potential at equilibrium is called the reversible (or half-cell) potential. The reaction rate across a metal-solution interface depends on the potential difference between the actual non-equilibrium and equilibrium potentials. The relationship between the current density across the metal-solution interface and the applied potential are given by the Butler-Volmer equation, one of the most fundamental equations in electrode kinetics.

$$i = i_0\left(\exp(\frac{(1-\beta)\eta F}{RT}) - \exp(\frac{-\beta\eta F}{RT})\right)$$

The first exponential term in the Butler-Volmer equation describes the anodic reaction and the second term the cathodic reaction. The 1- β and - β are the energy fractions of the

reaction in the anodic and cathodic direction, respectively; the term η, called the overpotential, measures how far the electrode potential is shifted away from the equilibrium potential. Depending on the direction of the shift, it can be an anodic or cathodic overpotential, e.g.:

$$\eta_a = E - E_0$$

$$\eta_c = E_0 - E$$

If the external potential is large enough, the Butler-Volmer equation can be simplified according to either anodic or cathodic polarization (Ramachandran and Beaudoin 2001).

2.2.2.3 Mixed Potential Theory

Considering the Fe/Fe^{++} half-cell reaction ($Fe = Fe^{++} + 2e^-$), if iron dissolution and re-deposition are the only pair of reversible reactions that take place on the surface of the iron electrode, there will be no corrosion of the iron electrode because the system is reversible and the loss of iron is redeposited back to the electrode at the same rate. However, if other half-cell reactions exist and consume the electrons generated by the iron dissolution reaction, for example, the hydrogen evolution reaction ($2H^+ + 2e^- = H_2$) in the case of the iron electrode in hydrochloric acid containing ferrous ions, the iron electrode corrodes, accompanied by the generation of hydrogen gas. The hydrogen evolution reaction thus makes the iron dissolution reaction irreversible, leading to a loss of metal and hence results in corrosion of iron. The electrode will fail to remain at reversible potentials

of either Fe/Fe^{++} or H_2/H^+, but must lie at a potential in between the two. This potential is achieved when the hypothesis of the mixed-potential theory is satisfied: the total rate of oxidation must equal the total rate of reduction. The principle of charge conservation must be satisfied by any number of half-cell reactions occurring simultaneously on an electrode surface (Jones, 1996).

The mixed potential theory is illustrated in Figure 2-2 for iron corrosion in acid, which contains two reversible reactions, the Fe/Fe^{++} and the H_2/H^+. Both reversible reactions are associated with reversible equilibrium potentials $E_{Fe/Fe^{++}}$ and E_{H_2/H^+}. The intersection between the iron dissolution curve (the anodic branch of the Fe/Fe^{++} reversible reaction) and the hydrogen evolution curve (the cathodic branch of the H_2/H^+ reversible reaction) represents the condition at which the anodic (oxidation) and cathodic (reduction) currents are equal and no net external current flows. The current value at such a point is defined as the corrosion current i_{corr} and the corresponding potential is the "mixed-potential" or corrosion potential, E_{corr}.

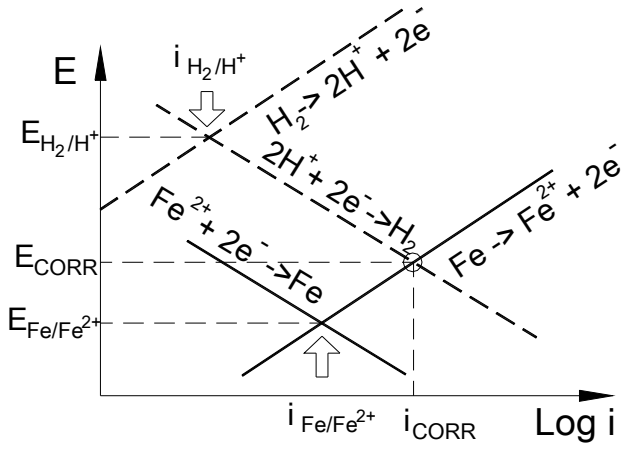

Figure 2-2: Description of mixed potential theory

2.2.2.4 Corrosion of Steel in Concrete

Concrete Properties

Concrete is a heterogeneous material which is characterized by the high alkalinity and high electrical resistivity. In addition concrete has a very complex microstructure comprising of cement hydration products which has a porous structure. Mass transport of moisture and ions through concrete is a slow process which is governed by the diffusion mechanism (Gjørve 1976).

Corrosion of steel in concrete is associated with anodic and cathodic reactions which consist of the dissolution of ion into solution and reduction of oxygen respectively (Ramachandran and Beaudoin 2001).

Anodic reaction: $Fe \rightarrow Fe^{2+} + 2e^-$

The standard electrode potential of this reaction is -0.44 V vs. NHE (Normal. Hydrogen Electrode) or -0.682 V vs. SCE (Saturated Calomel Electrode).

Cathodic reaction: $\frac{1}{2}O_2 + H_2O + 2e^- \rightarrow 2(OH)^-$

The standard electrode potential of this reaction is 0.401 V (vs. NHE) or 0.159 V (vs. SCE). In the absence of oxygen and at a pH value less than 9, the reduction reaction occurs with an evolution of hydrogen as shown below.

$2H_2O + 2e^- \rightarrow H_2 + 2(OH)^-$

The standard electrode potential of this reaction is -0.828 V (vs. NHE) or -1.070 V (vs. SCE).

After oxidation, iron will change to different types of oxides, depending on the availability of oxygen, e.g., $Fe(OH)_3$, FeO(OH), HFeOOH, $HFeO_2$, $FeSO_3$, and especially black rust Fe_3O_4 as given in the following equations (Vesikari, 1988).

$3Fe + 8(OH)^- \rightarrow Fe_3O_4 + 8e^- + 4H_2O$

$4Fe(OH)_2 + 2H_2O + O_2 \rightarrow 4Fe(OH)_3$

$Fe^{2+} + 2(OH)^- \rightarrow Fe(OH)_2$

The iron oxides formed and their corresponding volumes compared to the volume of

iron are shown in Figure 2-3.

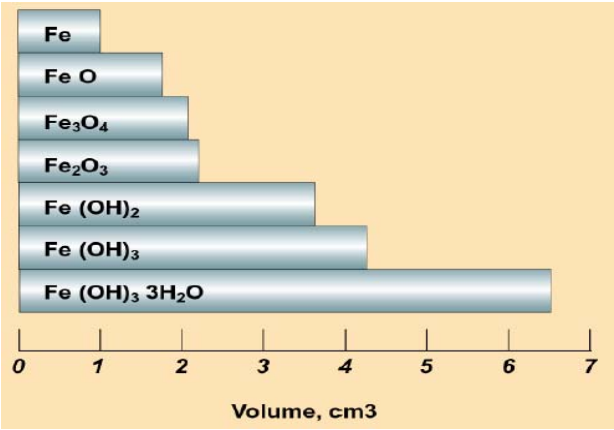

Figure 2-3: Relative volume for various oxides of iron. The volumes of all oxides are expressed per iron-atom.

There are three main types of iron corrosion products which could be distinguished by appearance (Aligizaki 1999).

Red rust: $Fe(OH)_3$, Fe_2O_3.

Black rust: Fe_3O_4.

Green rust: formed when chlorides are present.

2.2.3 Two Mechanisms: Localized Corrosion and Distributing (Uniform) Corrosion

In reinforced concrete structures, anode and cathode may be microscopically adjacent or spatially separated. In the case of chloride induced corrosion, the sites of anodic and cathodic reactions have been observed to be up to a few meters apart. The anodic reaction is confined to steel surface zones where the critical chloride content causing depassivation

is exceeded, the cathodic reaction may occur in all areas that are not permanently water-saturated (Schiessl and Raupach, 1997). Researchers refer to the two mechanisms of corrosion as microcell and macrocell corrosion as shown in Figure 2-4 (Arya 1995, Schiessl and Raupach 1997 and Sagues 1996).

In microcell corrosion mechanism, the anodes and cathodes are extremely small and located closely side by side. In macrocell corrosion mechanism, the anode is very small and the passive steel surface surrounding the anode zone forms the cathode. In this case, much higher local corrosion rates are to be expected than in microcell mechanism, since the steel surface involved in the cathodic subprocess is much larger.

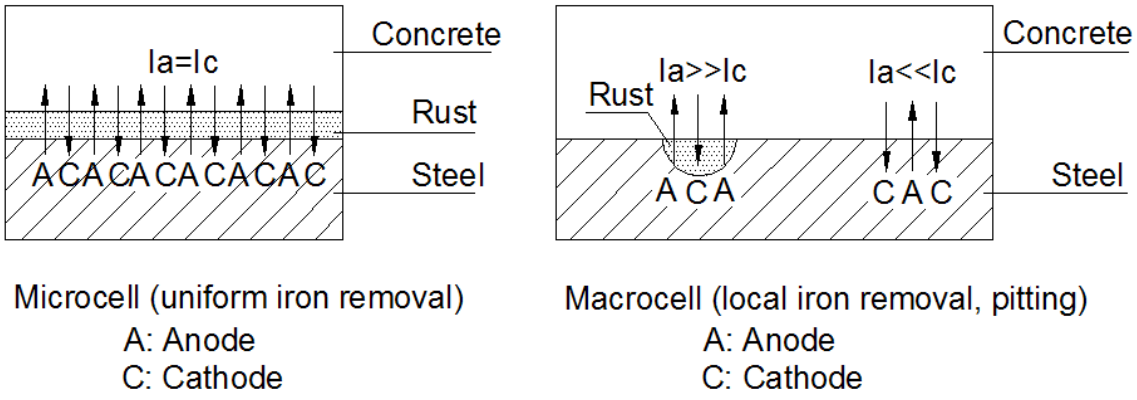

Figure 2-4: Schematic representation of microcell and macrocell corrosion.

In most cases, both microcell corrosion and macrocell corrosion exist in structures as shown in Figure 2-5.

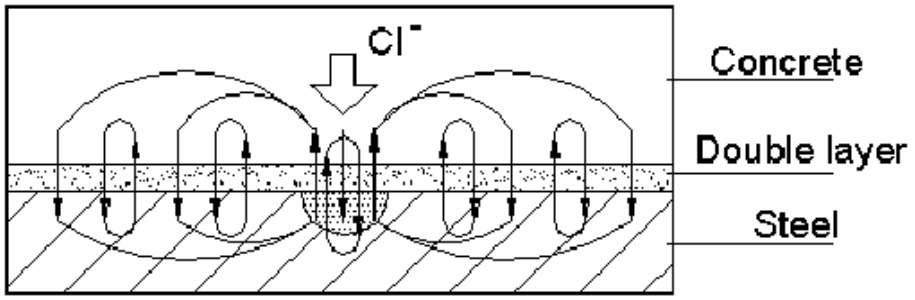

Figure 2-5: Combination of microcell and macrocell corrosion.

Elsener (2002) studied the influence of conductivity and cover depth on potential and macrocell current distribution in open circuit conditions and under external anodic polarization. The macrocell was made by small steel anode and surrounding large stainless steel immersed in electrolytes and mortar. The results of half-cell potential measurement have shown that the high concrete resistivity and low cover allow for locating the presence of the macrocell anode from surface measurements. In the linear polarization resistance (LPR) measurement, most of the DC current flows to the local anode despite the large area of the cathode and the value of polarization resistance (R_p) can be in error by a factor of 10.

2.3 METHODS TO DETECT CORROSION

A number of techniques have been developed during the last decade in order to determine the corrosion rate of steel embedded in concrete. Many electrochemical techniques have been used in reinforced concrete corrosion studies. The advantages of

electrochemical techniques are rapid, non-destructive and easy to perform.

2.3.1 Visual and Microscopic Observation

The visual or microscopic observation of the corrode surface may provide the first indication of a corrosion problem and approximate the depth of the attack, the number of pits or the proportion of the attacked area. But this information by itself is not sufficient because it may lead to erroneous and subjective conclusions and usually must be completed with other results. (Schiessl 1989)

2.3.2 Weight Loss

The principle of this technique consists of weighing the steel bars before and after being introduced in the concrete to be tested. The difference in weight is a quantitative average of the metal loss due to corrosion (Schiessl 1989). The test method has been standardized in ASTM G31 (standard practice for laboratory immersion corrosion testing of metals) and NACE standard TM-01-69 (Laboratory corrosion testing of metals for the process industries, 1976 Version). This technique is very time-consuming and numerous specimens are necessary for studying the evolution of the process. Although it is only applicable in the laboratory it has been revealed as a useful tool to check the accuracy of electrochemical techniques that are able to measure quantitatively the corrosion rate, such as Linear Polarization Resistance (LPR) and electrochemical Impedance Spectroscopy

(EIS) discussed in the following sections.

2.3.3 Half Cell

By measuring the potential difference between a standard half-cell placed on the surface of the concrete and the steel rebar underneath as shown in Figure 2-6, an indication of the relative probability of corrosion activity can be obtained. When there is active corrosion, current flow (ion migration) through the concrete between anode and cathode is accompanied by an electric potential field surrounding the corroding bar. The equipotential lines intersect the surface of the concrete and the potential at any point can be measured using the half-cell potential method. By mapping equipotential contours on the surface, those portions of the steel bars where there is a high likelihood of corrosion activity are identified (Carino 1999).

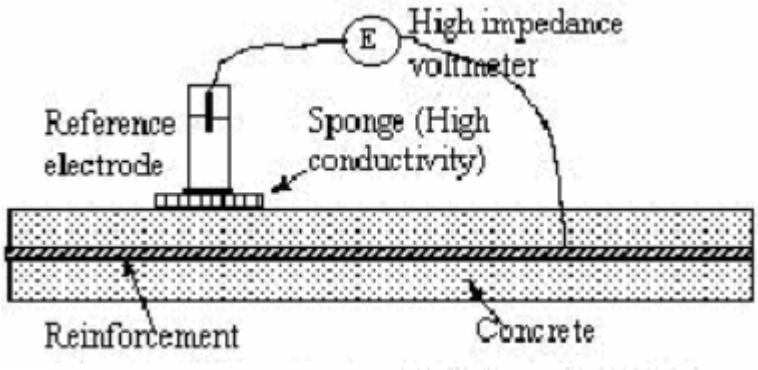

Figure 2-6: Principle of half-cell method.

The test procedure for obtaining half-cell potential is given in ASTM C876. The half-cell potential readings are indication of the probability of corrosion activity of the reinforcing steel located beneath the copper-copper sulfate reference cell. The ASTM standard provides guideline for interpreting the half-cell potential measurement as shown in Table 2-1.

Table 2-1: Interpretation of corrosion potential measurements

Cu/CuSO4	Calomel (SCE)	Ag/AgCl	Interpretation
E>-200mV	E>-126mV	E>-119mV	Greater than 90% probability that no corrosion is occurring
-200mV < E < -350mV	-126mV < E < -276mV	-119mV < E < -269mV	Corrosion activity is uncertain
E<-350mV	E<-276mV	E<-269mV	Greater than 90% probability that corrosion is occurring

2.3.3.1 Application of Half Cell measurements

The half-cell potential measurement is the most commonly used corrosion monitoring method in field assessment (Stratfull 1973). Evaluation of rebar corrosion considering only the "absolute" half-cell potential values may be misleading and cause errors in judgment (U.S. Department of transportation 1992). For example, a variation of 100 mV (from –150 mV to –250 mV) in half-cell potential reading may indicate more active rebar corrosion at a given section with a 30 mV variation (from –250 mV to –280 mV). Data

analysis and interpretation of half-cell potential measurement is complicated. Factors such as concrete moisture content, chloride content, oxygen content, temperature, cover thickness and cell placement are known to have a significant influence on half-cell potential readings (Elsener 2001). Therefore, to locate ongoing corrosion potential differences or gradients between active and passive areas are more important as shown in Figure 2-7.

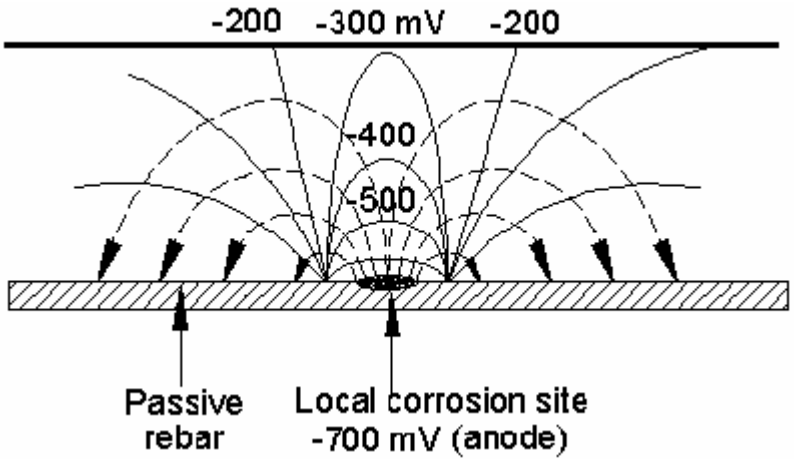

Figure 2-7: Schematic of the electric field and current flow of an active/passive macrocell on steel in concrete

2.3.4 Linear Polarization Resistance (LPR)

The main drawback of the half-cell potential method is that it only provides information about the likelihood of active corrosion, but not the corrosion rate. Several approaches have been investigated for measuring the in-place corrosion rate. Among these methods, linear polarization resistance (LPR) appears to be gaining the most acceptances.

2.3.4.1 Principle

The linear polarization resistance method involves measuring the change in the open-circuit potential of the short-circuited electrolytic cell when an external current is applied to the cell. Stern and Geary (1957) showed that for a small perturbation about the open-circuit potential, there is a linear relationship between the change in voltage (ΔE) and the change in applied current pre unit area of electrode (Δi) given as:

$$R_p = \frac{\Delta E}{\Delta i} = \frac{\Delta E}{\Delta I / Area}$$

where R_p is the polarization resistance. The relationship between the corrosion rate and the polarization resistance was obtained by Stern and Geary (1957) as:

$$i_{corr} = \frac{B}{R_p}$$

$$B = \frac{\beta_a \beta_c}{2.303(\beta_a + \beta_c)}$$

Where: i_{corr} = corrosion current density in $\mu A/cm^2$.

B = a constant in V (assumed as 26 mV for passive steel and 52 mV for active steel by Andrade 1978).

R_p = polarization resistance in $\Omega.cm^2$.

β_a = the Tafel slope of the anodic reaction.

β_c = the Tafel slope of the cathodic reaction.

2.3.4.2 Application of LPR to Reinforced Concrete

Considerable work has been done in applying LPR techniques to obtain corrosion rate of steel embedded in concrete (Andrade, Feliu and co-workers 1978, 1985, 1989). A typical configuration used for obtaining linear polarization measurement from steel in concrete is shown in Figure 2-8. This setup is referred to as the 3LP system. In a typical measurement, R_p is determined from the slope of potential-current density curve. Broomfield (1994) gave the guideline for estimation of extent of corrosion extentfrom the measured R_p as shown in Table 2-2.

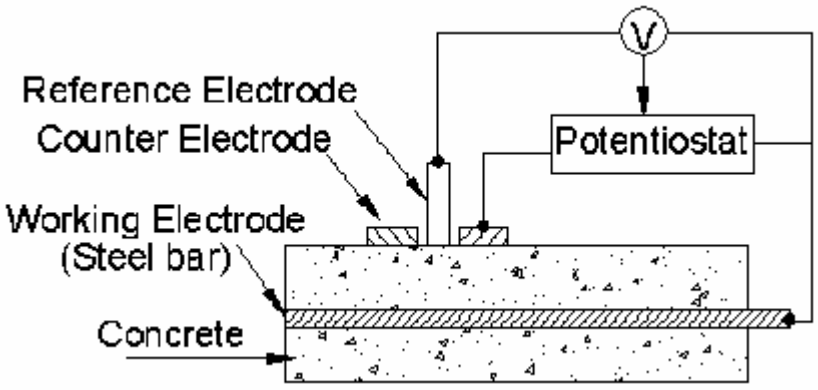

Figure 2-8: Schematic of polarization resistance measurement.

Table 2-2: Guideline for estimation of corrosion extent using I_{corr}

Rp (Ohms*cm^2)	Corrosion current density, (μA/cm^2)	Extent of corrosion
$R_p > 260{,}000$	$I_{corr} < 0.1$	P: passive condition
$10000 < R_p < 260{,}000$	$0.1 < I_{corr} < 0.5$	L: low to moderate corrosion
$5000 < R_p < 260{,}000$	$0.5 < I_{corr} < 1$	M: moderate to high corrosion
$R_p < 5000$	$I_{corr} > 1$	H: high corrosion

Corrosion current densities can be converted to metal loss by using Faraday's law (ASTM G102: corrosion current density of 100 μA/cm^2 results in a steel metal loss of 1.16 mm/year.). The assumption is that the corrosion is uniform along the metal surface.

Several difficulties are encountered in applying LPR to estimate the corrosion rate of reinforcing steel in concrete. The two most important problems are: (a) the difficulty in determining the area of the working electrode; (b) the current distribution between the working electrode and counter electrode is not uniform because the area of WE is normally much larger than that of the CE (Feliu 1989). Two approaches have been followed to overcome this difficulty. The first uses a "guard ring", a second electrode surrounding the first counter electrode as shown in Figure 2-9. The same potential is applied at the guard electrode to confine the current paths between the WE and CE. Thus, the area of WE polarized by the CE is equal to the area of CE. The second approach consists of using a transmission line model to determine the true local polarization resistance according for the

spread of the electrical current.

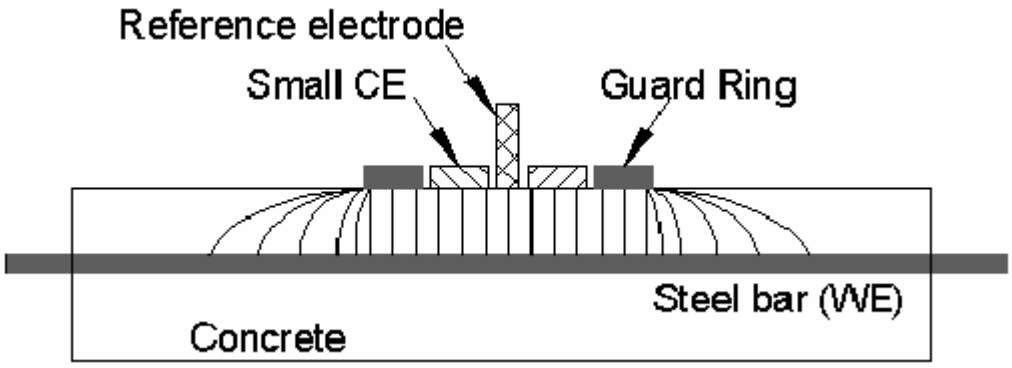

Figure 2-9: Scheme of guard ring

Gonzalez et al (1985) compared the results of different electrochemical methods to evaluate the corrosion rate such as: LPR, potential step, charging curve analysis, coulostatic pulse method and electrochemical impedance. They concluded that linear polarization resistance measurement is the most successful and reliable method, which is suitable for laboratory and on-site use. Feliu and Gonzalez (1989) obtained typical values of polarization resistance per unit area of steel surface, R_T. From their measurements, R_T of steel in active steel and passive states were found to be in the range 10^3~10^4 ohm.cm^2 and 10^5~10^6 ohm.cm^2 respectively.

2.3.5 Electrochemical Impedance Spectroscopy (EIS)

Electrochemical Impedance Spectroscopy is a powerful method for characterizing

many of the electrical properties of materials and interfaces. It is widely used for solid materials, both fundamental and applied electrochemical studies, including aspects of electrode kinetics, battery performance, corrosion and high temperature electrochemistry. The use of this technique in reinforced concrete corrosion study was initiated only in the 1980's. Since then, this technique has been used by an increasing number of corrosion researchers. However, interpretation of an impedance spectrum is difficult due to the complexity of cement chemistry and concrete microstructures changes taking place on steel surfaces. The analysis is strongly dependent on how the electrical components are selected and the extent to which they represent the microstructure of steel-concrete interface.

Crentsi et al (1992) have proposed a physical model to describe the steel/concrete interface as shown in Figure 2-10. Many equivalent circuit models have been proposed to describe the steel concrete interface and to interpret the impedance spectrum. RC parameters can be determined through a computer simulation of the experimental spectra using the selected equivalent circuit.

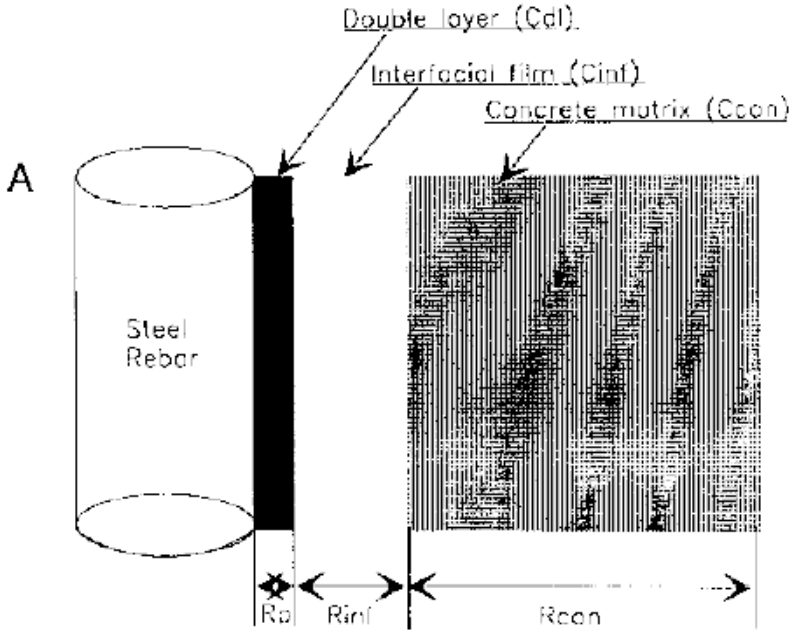

Figure 2-10: Physical model to describe the steel/concrete interface.

High frequency range in an impedance spectra provides information about the dielectric properties of concrete, while the low frequency range contains information about dielectric properties of passive film on the steel. In spite of these possibilities, the method has not had wide application in reinforced concrete, because the impedance spectra are often complex and difficult to interprete.

Monteiro, Morrison and Frangos (1998) present a new method using a multi-electrode array as give in Figure 2-11 to measure the complex impedance along the surface of a concrete structure to determine the position of the reinforcing bars and their corrosion state. The equivalent circuit of four-electrode array is given in Figure 2-12.

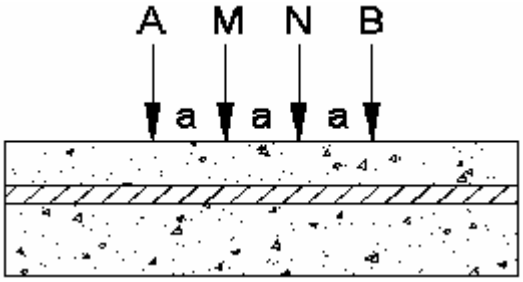

Figure 2-11: Four-electrode array to measure the resistivity of concrete

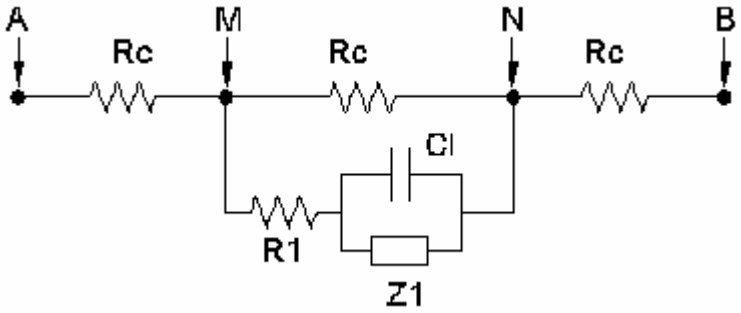

Figure 2-12: Equivalent circuit of four electrode array

2.4 INFLUENCE OF CRACK ON CORROSION OF STEEL IN CONCRETE

2.4.1 Impact of Crack on Corrosion of Steel in Concrete

Cracks are often introduced in concrete structures due to the action of loads and other causes such as restrained shrinkage, thermal gradients et al (Borgard et al, 1989). Cracks in concrete structures reduce the overall strength, stiffness of concrete structures and

accelerate the ingress of oxygen, water and other aggressive ions, leading to other types of the corrosion and much higher corrosion rate comparing with uncracked ones. Once a crack is formed in reinforced concrete, it will provide an easy access for ingress ions such as chloride, oxygen and water to the steel surface. The main transport mechanism for chloride ingress in cracked concrete is convection due to capillary suction of deicing water, while it is diffusion in uncracked concrete. Therefore, the chloride will attack the passive layer of steel at the crack zone and lead to corrosion much earlier than expected. Furthermore, a macrocell will be formed by a small anode at the crack supported by large cathode around the crack.

Schiessl and Raupach (1997) studied the cell measurement on cracked reinforced concrete specimens and found that the chloride-induced steel corrosion in the crack zone involves the formation of a macrocell. The steel in crack zone acts as the anode and the steel between the cracks, up to a distance of several decimeters from the cracks, forms the cathode. The corrosion rate of steel in the crack zone was shown to be influenced considerably by the factors such as resistivity of concrete, crack spacing, cover depth and crack width.

2.4.2 Influence of Crack Width, Crack Distance, Cover Depth and Concrete Resistance

Arya (1995) studied the influence of cathode-to-anode area ratio and separation

distance on the corrosion current in concrete and found that the current increased with increasing cathode/anode area but the rate of increasing decreased with increasing cathode/anode ratio. The current decreased with increasing separation between the anode and cathode although the cathode elements most distant from the anode contributed a significant current.

Arya (1996) studied the influence of crack frequency on corrosion and found that the smaller the frequency of cracks, the smaller is the amount of corrosion. This suggests that an effective way to control corrosion in cracked concrete may be to limit the frequency of crack, by increasing the cover depth of concrete, rather than by controlling surface crack width.

Berke, et al. (1991) found that the addition of calcium nitrite in concrete reduces overall and pitting corrosion of rebar in cracked concrete. Francois and Arliguie (1999) studied the effect of microcracking and cracking on the development of corrosion in RC under service load, They found that it is not the width of cracks or the crack themselves, but the tensile microcracking in concrete, that increases the penetration of chloride ions and then reduces the service life of reinforced concrete. Firstly, the loading causes an increase in chloride penetration because of the paste-aggregate interface damage, and secondly, it encourages the development of corrosion on the tensile reinforcement because of the steel-concrete interface damage.

Mohammed et al (2002) found that the presence of gaps/voids at the steel-concrete

interface leads to macrocell and microcell corrosion. Mohammed and Otsuki (2001) compared the corrosion performance of plain and deformed bars. They found that the oxygen permeability of cracked concrete with deformed bars is much higher than one with plain bars. In the vicinity of a flexural crack, a macrocell was formed and the local corrosion rate increased remarkably. Without cracks, in the upper side of the stirrup that had the largest corrosion rate, the microcell corrosion rate was five times as large as the macrocell corrosion rate; with cracks, at the main reinforcing bars intersecting the crack had the largest corrosion rate, the macrocell rate was 70 times as large as the microcell rate. The corrosion rate of main reinforcing bars intersecting the crack was 0.02 mm/year, which was three times faster than the case without a crack.

The influence of crack width in the corrosion of reinforcing steel is controversial. Some studies have shown that cracks less than approximately 0.3 mm (0.012 in.) wide have little influence on the corrosion of reinforcing steel (Atimay and Ferguson, 1974). However, other investigations have shown that there is no relationship between crack width and corrosion (Tremper, 1947; Martin and Schiessel, 1969; Raphael and Shalon, 1971).

2.5 INTERPRETIVE MODELS FOR ELECTROCHEMICAL TECHNIQUES

Application of standard electrochemical techniques such as LPR and EIS requires the

use of models to interpret the measured response. For example, the use of a counter electrode which is much smaller than the concrete structure produces a non-uniform distribution of current (as shown in Figure 2-13). In such a situation, R_p of the steel bar cannot be directly determined from he measured response. Feliu et al (1988, 1989) introduced a "transmission line model" to solve the problem. In this model an equivalent circuit representation, as shown in Figure 2-14 is developed for the reinforced concrete structure. The electrical responses of steel-concrete interface and the concrete medium are represented using a distribution of resistances. By solving the model, the distribution of current along the steel bar the local polarization resistance Rp can be obtained.

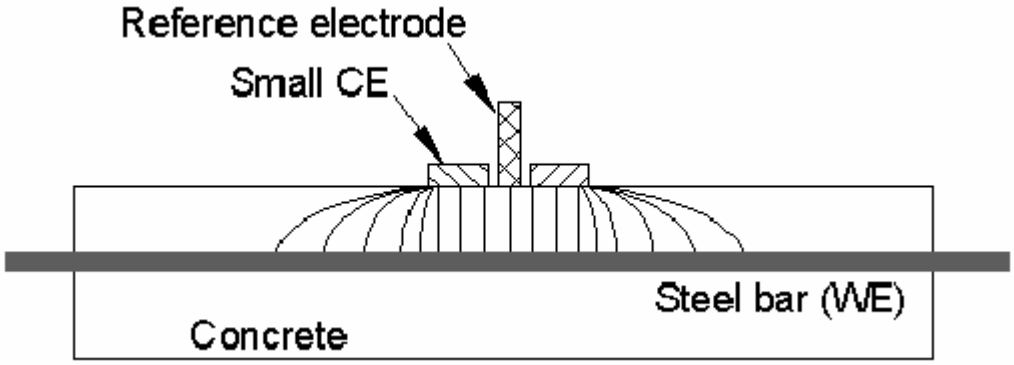

Figure 2-13: Non-uniform electrical field produced by a small counter electrode.

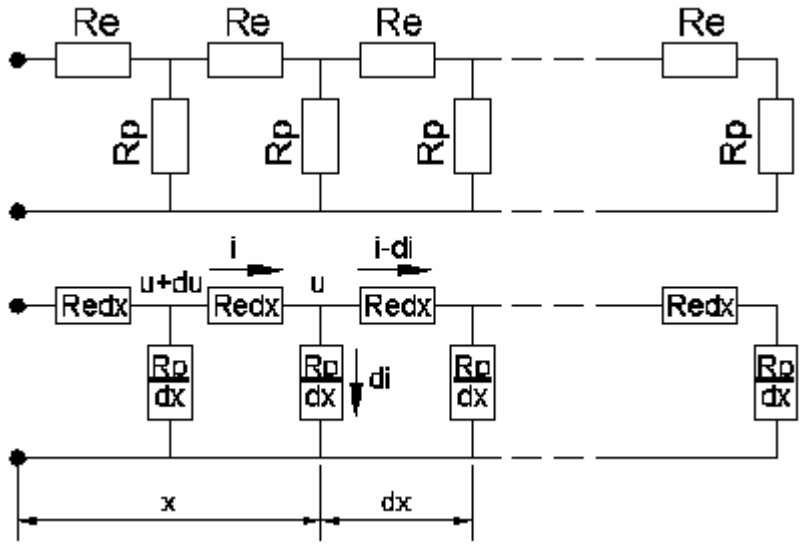

Figure 2-14: Beam represented by the transmission line model

Electrical circuits with well-defined elements have often been used to describe the transient response of the steel-concrete interface and concrete medium to an applied potential or current perturbation. The elements of the circuit such as resistances and capacitances provide a convenient way to represent the underlying phenomena which influence the flow of charge at the steel interface. For instance, the Randle's circuit has been used to explain the response of steel corroding in an electrolyte. In the case of reinforced concrete, however, the simple Randles circuit has been shown to diverge from the real response of the steel-concrete interface (Feliu, 2002).

Different circuit representations have been proposed to explain the observed response of the steel embedded in concrete to an external potential or current perturbation. Newton

and Sykes (1988) proposed a circuit with three time constants, each associated with one parallel resistor-capacitance (RC) combination, to represent the response of the steel-concrete system to a current step. While one time constant was related to concrete, the remaining two time constants were associated with the electrochemical processes at the steel-concrete interface. The use of a series combination of resistor-capacitance pairs to model the response of the steel-interface has also been explored by other researchers (Agarwal, 1992; Law, Millar and bungey, 2000). Interpreting the significance of the parameters and ascribing the elements of such circuits to underlying physical phenomena is often very challenging. A circuit for the steel-concrete interface comprising of a parallel combination of a constant phase element (CPE) and a resistor has been proposed by Sagues et al (1995, 1996) based on the observations of depressed semi-circles in impedance diagrams and a slow evolution of pulse transients in time domain. The resistor in the equivalent circuit representation can be identified with the charge transfer resistance of the interface. Feliu et al. (1998, 2005) suggested a modified version of the circuit proposed by Sagues et al. (1996) by including the Warberg impedance to account for the diffusion resistance of some reacting species.

Sagues and Kranc (1992) reported a numerical equivalent model of a LPR experiment. The model, which was built by finite-difference method, was used to predict the shape of polarization curves of macrocell corrosion. The calculation result showed that current interruption couldn't be relied upon as the main method to reduce measurement deviations because of ohmic potential drops within concrete. Furthermore, the calculations reveal that

current distribution effects can result in overestimation of the anodic Tafel slope.

Dhouibi-Hachani (1996) developed a new model of electrical impedance of steel-concrete interface. In this model, a part of the impedance is related with the products formed directly on steel. Another part of impedance corresponds to the transition zone between steel and concrete, and the third part corresponds to the inhomogeneity of the products formed at the interface.

It is generally accepted that the physical model of the steel/concrete interface consists of a layer of a compact iron oxide film (in the passive stage) and an interfacial film adjoined to the concrete matrix. The interface film consists of $Ca(OH)_2$ deposits and other cement hydration products deposited onto the surface of the steel, it also involves the change of dielectric constants due to the diffusion of iron oxides into the steel/concrete interface. Gu (1997) presented a modified electrical equivalent circuit, as shown in Figure 2-15, to simulate the response of reinforcing steel in an EIS measurement. This circuit consists of three parallel combinations of a pure resistors and frequency dependent capacitor (which is also called a constant phase element (CPE) introduced to account for the shape of the depressed complex plot) to represent the concrete matrix, interface film and steel/concrete corrosion process arcs in the Nyquist plot.

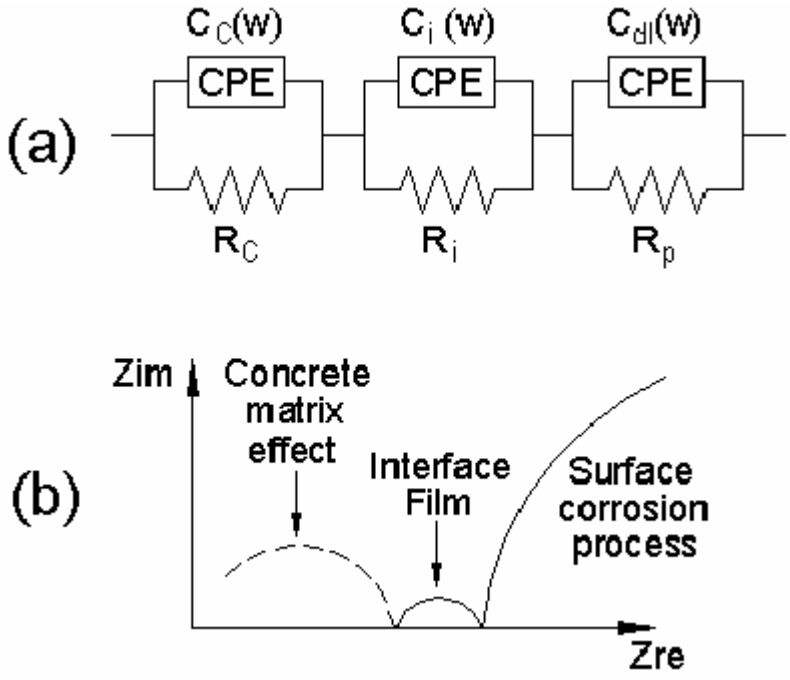

Figure 2-15: (a) the equivalent circuit consists of three parallel combinations of a pure resistor and a frequency dependent capacitor; (b) Corresponding impedance plot in the complex plane (Nyquist plot).

CHAPTER 3
EXPERIMENTS IN UNCRACKED CONCRETE: CPE BEHAVIOR OF STEEL-CONCRETE INTERFACE

3.1 INTRODUCTION

Understanding the transient response of a corroding steel interface subjected to an external potential or current is essential for determining the rate of corrosion. Electrical circuits with well-defined elements have often been used to describe the transient response of the steel interface to an applied potential or current perturbation. The elements of the circuit such as resistances and capacitances provide a convenient way to represent the underlying phenomena which influence the flow of charge at the steel interface. For instance, the Randle's circuit has been used to explain the response of steel corroding in an electrolyte. In the case of reinforced concrete, however, the simple Randles circuit has been shown to diverge from the real response of the steel-concrete interface (Feliu, 2002).

Different circuit representations have been proposed to explain the observed response of the steel embedded in concrete to an external potential or current perturbation. Newton and Sykes (1988) proposed a circuit with three time constants, each associated with one parallel resistor-capacitance (RC) combination, to represent the response of the steel-concrete system to a current step. While one time constant was related to concrete, the remaining two time constants were associated with the electrochemical processes at the steel-concrete interface. The use of a series combination of resistor-capacitance pairs to

model the response of the steel-interface has also been explored by other researchers (Agarwal, 1992; Law, Millar and bungey, 2000). Interpreting the significance of the parameters and ascribing the elements of such circuits to underlying physical phenomena is often very challenging. A circuit for the steel-concrete interface comprising of a parallel combination of a constant phase element (CPE) and a resistor has been proposed by Sagues et al (1995, 1996) based on the observations of depressed semi-circles in impedance diagrams and a slow evolution of pulse transients in time domain. The resistor in the equivalent circuit representation can be identified with the charge transfer resistance of the interface. Feliu et al. (1998, 2005) suggested a modified version of the circuit proposed by Sagues et al. (1996) by including the Warberg impedance to account for the diffusion resistance of some reacting species.

In typical measurements on reinforced concrete, behavior of the steel-concrete interface is inferred from the potentials recorded at the concrete surface. The measured response contains contributions from both concrete and the steel interface. The influence of concrete on the measured response often complicates the analysis of data. It is difficult to clearly ascribe aspects of the measured response to individual contributions from the concrete and the steel-concrete interface.

This chapter aims to provide a direct experimental determination of a circuit representation for the steel-concrete interface using measurements at the steel surface. The changes in the potential close to the steel surface in response to an applied external potential on the concrete surface are measured using an embedded reference electrode (ERE). The steel-concrete interface response is investigated using a test system which allows simultaneous measurements at the steel-concrete interface and on the concrete

surface. The transient response of the steel-concrete interface is obtained from two measurements: a) linear variation of the applied potential (linear polarization); and b) an AC measurement with a frequency sweep (impedance measurements). In all tests the applied excitation is varied relative to the potential recorded on the concrete surface. From the frequency sweep tests, the impedance of the steel-concrete was determined at discrete frequencies. The impedance of the steel-concrete interface was directly determined from the potential changes recorded at the steel-concrete interface using the ERE. An equivalent circuit representation comprised of a parallel combination of a CPE and a resistor (R_t) was found to be suitable for both active and passive steel. The validity of the equivalent circuit representation was verified using the linear potential scan measurements. The parameters obtained from the frequency sweep measurements for the idealized R_t-CPE response were found to provide an acceptable prediction of the measured time-domain response in the linear potential scan.

3.2 OBJECTIVES

The objectives of the work presented in this chapter are:

1. To study the changes in the measured potential at the steel-concrete interface for a given external potential change at the concrete surface.
2. To identify an equivalent circuit representation for the steel-concrete interface that captures its response to a transient potential input.
3. To provide a validation for the circuit representation of the steel-concrete interface from the direct potential measurements close to the steel surface.

3.3 MATERIALS AND METHODS

Two series of concrete specimen, labeled A and B, respectively were cast. In specimens B, NaCl was added to the mix water to provide a chloride concentration of 3.7% by mass of cement. Type 1 Portland cement (ASTM C 150[9]) was used for all specimens. The cement : sand : coarse aggregate ratio of concrete by weight was 1 :1.70 : 2.42 and the water/cement ratio was 0.45. Ordinary tap water was used for mixing the concrete. An air entraining agent, MB-VR by Master Builders (ASTM C 494, 2000), was used. Three specimens were cast for each series. The specimen geometry is shown in Figure 3-1. Plain carbon steel reinforcing bars, 12.8 mm in diameter, was used in the specimen. The rebar area was approximately 100 cm^2. The concrete cover depth for all specimens was 25.4 mm.

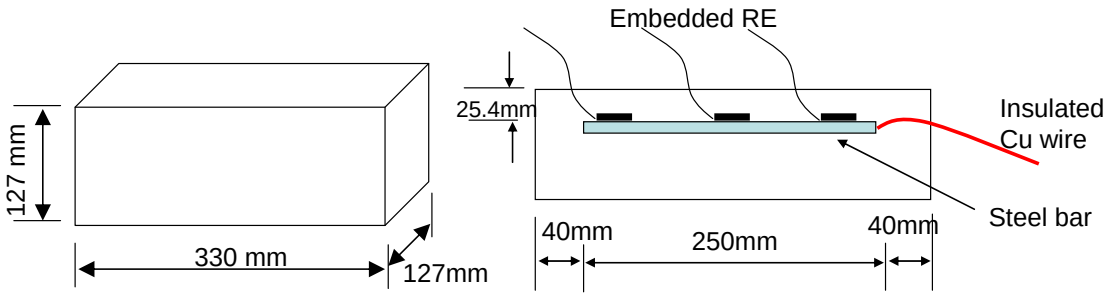

Figure 3-1: Specimen geometry and dimensions.

The steel bars were cleaned with acetone and polished using 600-grit Sic paper. Electrical connections were made with each steel bar by soldering a copper wire close to one of its ends. A commercially available Ag/AgCl embedded reference electrode, V-2000™, was used. The ERE comprises of a silver wire coated with AgCl, which is

housed inside a pervious Teflon braiding. The reference electrode was electrically connected with an insulated conducting lead-out wire using a butt-crimp connector. The electrical connection was sealed using liquid electric tape and a shrink wrap Teflon (as shown in Figure 3-2(b). All the electrical connections were performed inside a dessicating chamber under flowing Nitrogen gas. The ERE and the lead-out wire were attached to the rebar using Nylon ties as shown in Figure 3-2(a).

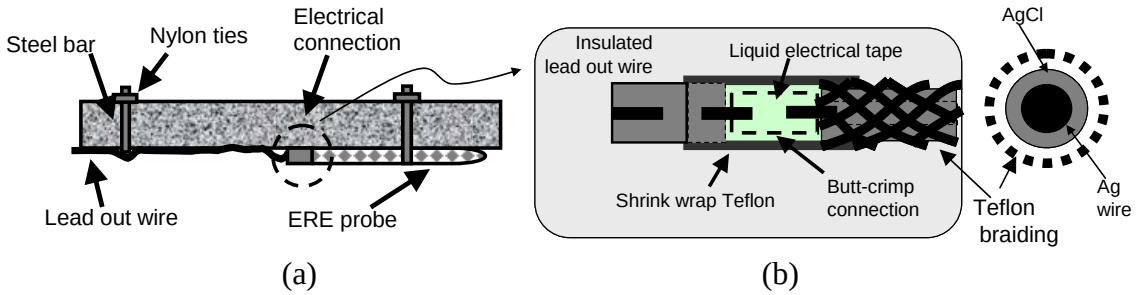

Figure 3-2: (a) Attachment of ERE to steel bar; (b) Ag/AgCl embedded reference electrode.

All specimens were demolded 24 hours after casting and cured in a 100% relative humidity (RH) chamber for 28 days following which they were subjected to periodic wetting and drying cycles. Each wetting-drying cycle involved three days of wetting followed by a four-day drying period. During wetting, the specimens were subjected to 100% RH at 23 ºC. The drying comprised of exposing the specimens to the laboratory environment, which was maintained at 50% RH and 23º C.

Measurement procedures

Test configuration used for simultaneous potential measurement at the steel-concrete interface to an applied potential on the concrete surface is shown in Figure 3-3. A stainless steel counter electrode (CE) with a length larger than the steel bar was used. In all tests the applied excitation is varied relative to the potential recorded on the concrete surface using a saturated calomel electrode (SCE). The ERE was used for monitoring the potential at the steel-concrete interface. The external polarization was applied between the counter electrode and the working electrode using a commercially available potentiostat with a built in frequency response analyzer (FRA). The standard three-electrode setup shown in Figure 3-3 was used for connecting the potentiostat with the reinforced concrete specimen. During a test, data was collected using a high speed data acquisition system. Three channels of differential potentials, labeled CH1, CH2 and CH3, were simultaneously sampled, discretized and recorded (shown in Figure 3-3). Channel CHl was used to record the current flow between CE and WE. The current was calculated by dividing the potential reading of CH1 by 10 ohms. CH2 and CH3 were used to record the potential between the WE and SCE and ERE, respectively. The potentials were recorded using IOtech^{TM} WaveBook^{TM} data acquisition system. The data collection was initiated just prior to starting the scan and continued until the end of the scan.

Using the test system, the local change in the potential at the steel-concrete interface was investigated for two different forms of applied potential at the concrete surface. Linear potential scan and AC frequency sweep tests were performed on each specimen. The linear potential scan experiments were conducted at a rate of 0.1 mV/s. Potential scans were initiated 10 mV below the open circuit potential and ramped up to 10 mV above the open-circuit potential. For the AC frequency sweep, the excitation applied to

the electrodes by the potentiostat/FRA comprised of a sinusoidal voltage signal of fixed amplitude equal to 10mV. A typical test involved stepping through a number of frequencies starting at the highest frequency. The range spanning 1 kHz to 0.01 Hz was applied in 30 discrete frequencies, which were equally spaced on the logarithmic scale. The sampling rates for the data acquisition were equal to 100 Hz and 100 kHz for the linear potential scan and the frequency sweep measurements, respectively.

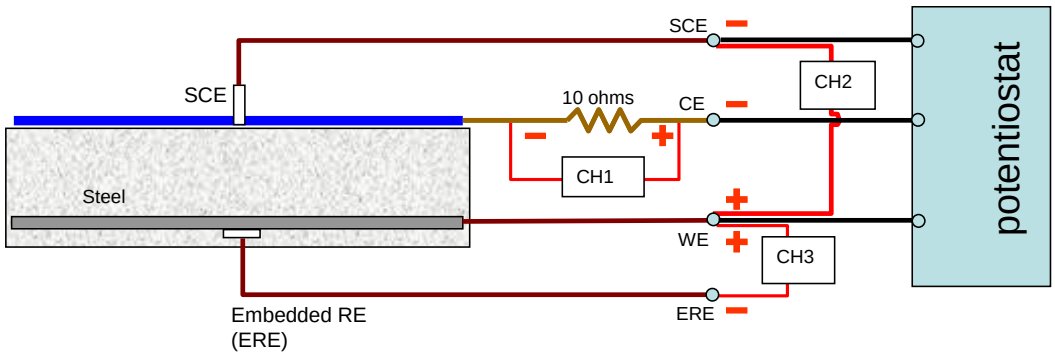

Figure 3-3: Test setup for simultaneous measurements at the steel-concrete interface and the concrete surface.

Data Processing and Analysis Procedures

The raw signals collected from all the channels were digitized and stored for analysis. The time domain signals collected from the linear potential sweep measurement were filtered using a low-pass FIR filter. The data from the frequency sweep measurements comprised of potential and current signals recorded at multiple frequencies. The data was processed in the frequency domain to obtain the impedance of the steel-concrete system and the steel-concrete interface. The magnitude and phase of the impedance were obtained by applying digital Fourier analysis to the voltage and current signals. The

current and the frequency signals recorded in a test were transformed into the frequency domain using the FFT algorithm (Oppenheim and Willsky 1983; Yoo and Park, 2005). The degree of shift between the current (output) and the voltage (input) waveforms was obtained from the phase spectrum of the Fourier transform of the two signals. The absolute magnitude of the impedance was obtained by dividing the magnitude of the amplitude spectrum of the voltage signal at the discrete frequencies by the corresponding values of the current signal. The in-phase and out-of-phase components of the total impedance were then determined at the discrete frequencies applied in the scan.

3.4 EXPERIMENTAL RESULTS

The half-cell potentials were recorded weekly at the end of the wetting period from the ERE and using an SCE reference electrode. The potentials recorded using the ERE and the SCE are shown in Figure 3-4. It was found that the half-cell potentials attained a stable value nine months after casting. The half-cell potentials indicate that the steel in Specimens A is in a passive state while the steel in Specimens B is actively corroding. This was later verified by examining the steel bar extracted from the specimens. The steel bar was extracted 420 days after casting and the steel surface was examined. No visible sign of corrosion was detected on the steel bar from specimens A. The surface of the steel bar from specimens B was coated with a layer of dark brown corrosion products, when observed by the unaided eye.

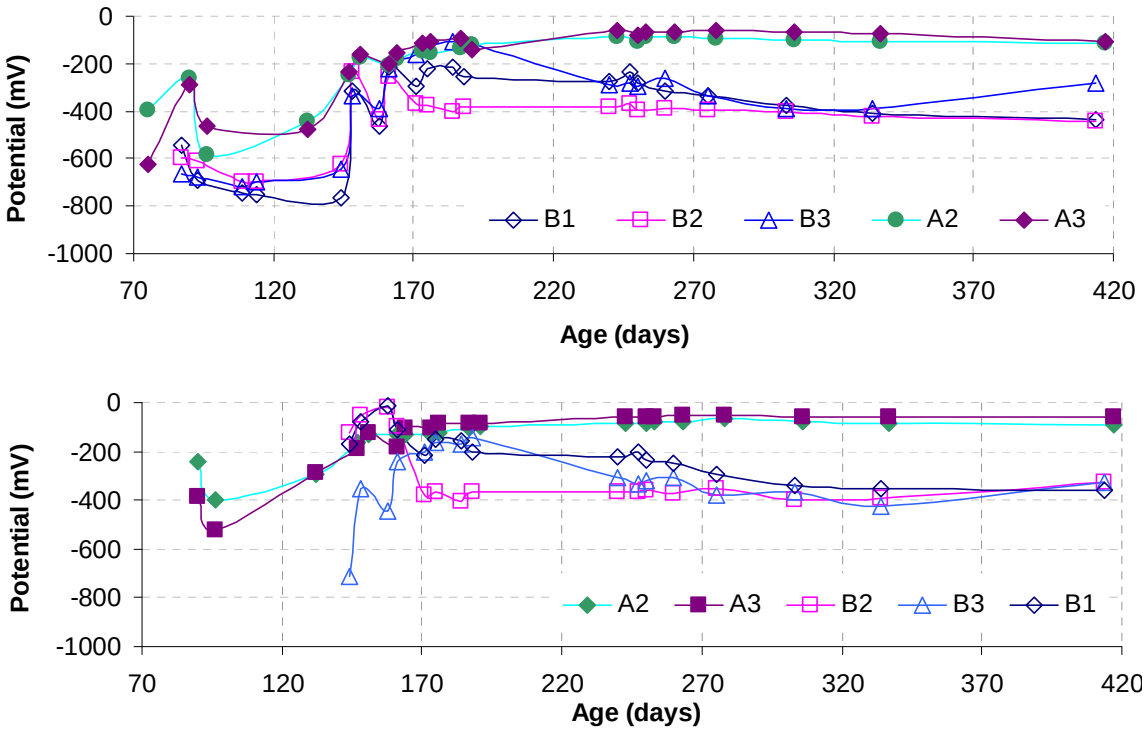

Figure 3-4: Half-cell potentials as a function of age after casting; (a) measured on the concrete surface using SCE; (b) measured at the steel-concrete interface using ERE.

The electrochemical measurements were initiated when the half-cell potential values recorded from the specimens stabilized over a two-month period. All the measurements were performed between 330 and 360 days of age. The impedance measured using the ERE and the SCE (on concrete surface) in a typical frequency sweep experiment from a specimen of series B (with chlorides) is shown in a Nyquist plot in Figure 3-5. The Nyquist plot using the measured potential on the concrete surface indicates the presence of a high frequency arc and an almost straight line response at the lower frequencies. The low frequency tail may be ascribed to diffusion control (John et al. 1981; Hope et al. 1986). The impedance determined from the embedded electrode however shows the presence of a single arc. This suggests that in the measured response from the concrete surface the high frequency arc at frequencies higher than 10 Hz is due to concrete. The

low frequency tail obtained in surface measurement indicates that the diffusive behavior in measurements obtained from concrete surface may also be attributed to concrete. Therefore the influence of concrete is clearly evident in the impedance spectrum at both the high and the low frequencies. Comparing the Nyquist plots from SCE and ERE, the contribution of the steel-concrete interface is predominantly in the frequency range spanning 10Hz and lower. This confirms the observations of Ford et al (1998) that the product layers and the electrochemical reactions at the electrode (steel-concrete interface) predominantly contribute in the low frequency region of the impedance spectrum spanning mHz – Hz (Ford, 1998).

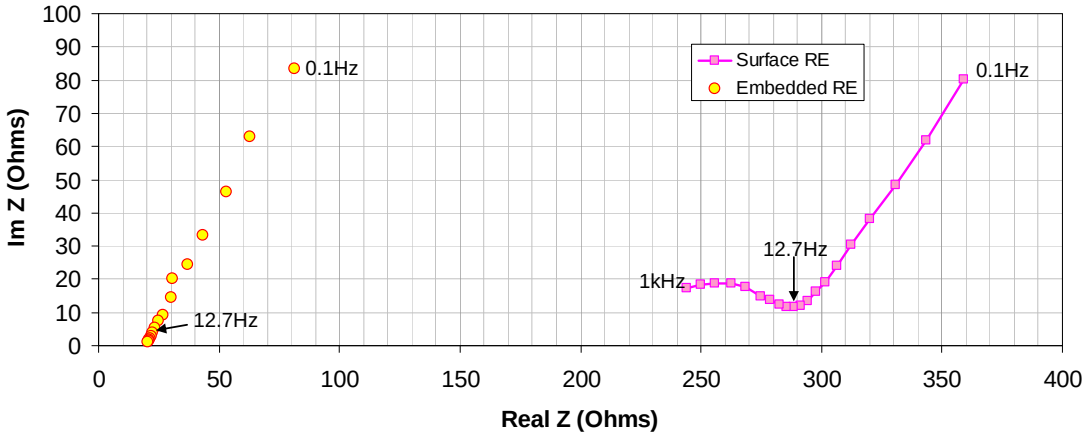

Figure 3-5: Comparison of local and global response from EIS measurements.

A comparison of the Nyquist plot using the impedance determined from ERE potential measurement is shown in Figure 3-6. The appearance of a single arc resembling a portion of a depressed semi-circle is evident in the impedance spectra of both active (Specimen B) and passive steel (Specimen A). The curvature of the Nyquist plot is very apparent in both cases. The tangent to the arc at its intersection with the real axis appears to be less than $\pi/2$ for both cases, which suggests a CPE response. It is interesting to note

that the intercept of the arc with the real Z axis is identical for both active and passive steel. The rapidly rising arc for the passive steel suggests an arc with a larger radius. The active steel in specimen with chlorides gives rise to a better defined arc.

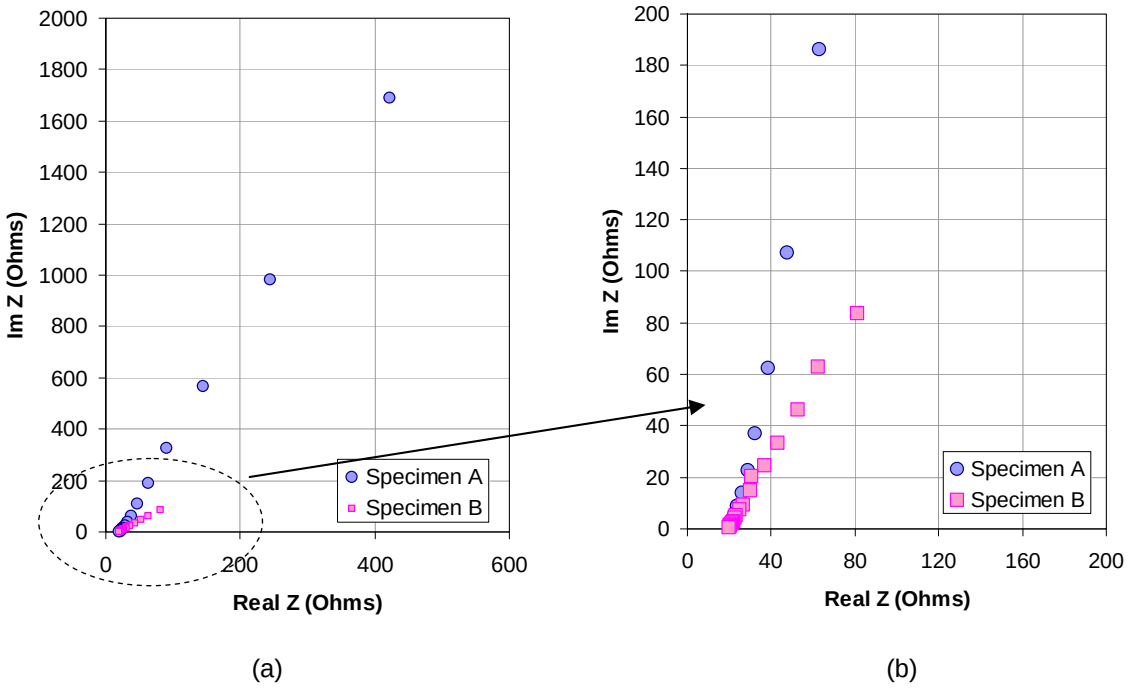

Figure 3-6: The Nyquist plot of impedance determined using ERE (b) Enlarged view of the high frequency response.

Equivalent circuit for the steel concrete interface

Considering the finite intercept and depressed semi-circle in the Nyquist plot of impedance using ERE, an equivalent circuit comprising of a series combination of a resistance (R_e) with a parallel combination of a resistance (R_t) and CPE element was considered for describing the observed response. This circuit shown in Figure 3-7 was first proposed by Sagues et al (1995). R_e and R_t correspond with the electrolyte resistance and charge transfer resistance, respectively. The CPE is a constant phase element used to represent the non-ideal capacitive response of the steel-concrete interface. The CPE

response has been attributed to surface roughness, inhomogeneous spatial distribution of reaction sites and the inherent heterogeneous nature of concrete (Rammelt and Reinhard, 1995). The impedance of a CPE is given as

$$Z_{CPE} = \frac{1}{(j\omega)^n Y_o} \tag{3.1}$$

where Y_o is a parameter with units $\Omega^{-1}s^n$ and $0<n\leq 1$. n = 1 represents an ideal capacitor and $0<n<1$ results in a non-ideal capacitive response.

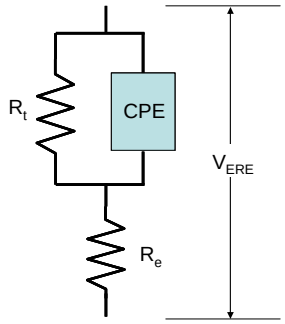

Figure 3-7: Equivalent circuit representation for the steel-concrete interface.

The values of the parameters for the elements of the circuit were obtained by fitting the circuit to the experimental data. The range of values obtained from specimens A and B are shown tabulated in Table 3-1. The electrolyte resistance for both specimens A and B is negligible. Since the surface area of the steel bar is $100cm^2$, the range of R_t is (10^4 -- 10^5) Ωcm^2 and (10^6 – 10^7) Ωcm^2 for specimens B and A, respectively. These values agree very well with the ranges of polarization resistance, R_p, for active and passive steel reinforcement suggested by Feliu et al (1989, 1986). The value of n for the CPE response for the steel in specimen B is in agreement with the values suggested by Sagues et al.

(1995). The values of n for the passive steel in specimen A (without chlorides) suggest that it approaches a pure capacitive response. This can be explained considering the relatively smaller spatial heterogeneity in the passivity of steel.

While the experimental trends from the Nyquist plots strongly suggest the presence of a single arc with a well defined behavior, the incomplete nature of the arcs for both active and passive steel mandates an independent verification of the proposed circuit. The verification for the proposed circuit was obtained using the linear potential scan experiments. A potential sweep where the potential is varied from a fixed value below to a fixed value above the open circuit potential is predominantly confined to the low and medium frequencies, which are of interest from the processes underlying corrosion (Feliu et al. 1998). The time domain response of the chosen circuit, such as that obtained from the linear potential sweep would therefore serve to validate the observations from the frequency sweep measurements. This requires that the parameters obtained from the frequency sweep measurements for the idealized R_t-CPE response provide an acceptable prediction of the measured response in the linear potential sweep.

Table 3-1: Parameters of the Equivalent $R_e(R_t\text{-CPE})$ circuit for passive and active steel

Specimen	R_e (Ω)	Y_o ($\Omega^{-1}s^n$)	n	R_t (Ω)
A (w/o chloride)	10 -- 20	0.005 - 0.008	0.84 - 0.93	10^4 - 10^5
B (with chloride)	10 -- 20	0.01 - 0.02	0.60 - 0.75	700 - 2500

Verification of the parameters using LPR

The potentials measured by the ERE and the SCE (on concrete surface) in a typical linear potential sweep experiment from a specimen of series B (with chlorides) and A

(without chlorides) are shown in Figures 3-8 and 3-9, respectively. The potentials (both SCE and ERE) in the plot are relative to their respective open circuit potentials. The potential measured by the ERE and the SCE are referred to as $V_{ERE}(t)$ and $V_{SCE}(t)$, respectively. It can be seen that while V_{SCE} is suddenly decreased to a value 10mV below the open circuit potential at the initiation of the scan, the corresponding change in V_{ERE} is significantly smaller. V_{ERE} changes more gradually to a more negative potential before starting to increase in the positive direction. The minimum value was reached approximately 20 seconds after starting the scan. Then the potential gradually increases to 10 mV. While initially the potential V_{ERE} lags the applied potential, the potential at the steel-concrete interface approaches the value measured on the surface. After 140 seconds, the value and the rate of change of V_{ERE} and V_{SCE} are identical.

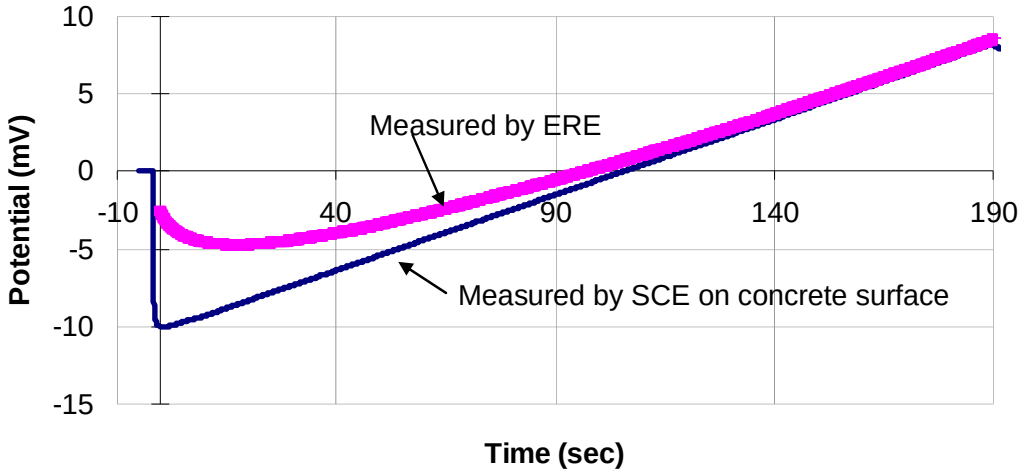

Figure 3-8: Potentials measured by the SCE on concrete surface and the ERE at the steel-concrete interface for specimen of Series B during a linear potential sweep experiment.

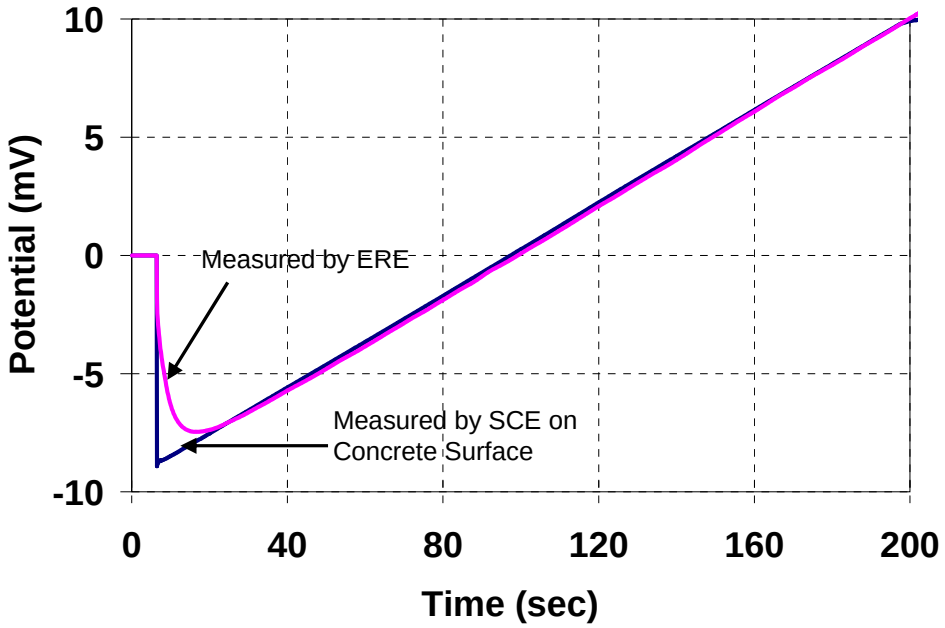

Figure 3-9: Potentials measured by the SCE on concrete surface and the ERE at the steel-concrete interface for specimen of Series A during a linear potential sweep experiment.

Considering V_{ERE} to be the applied polarization at the steel-concrete interface, the total current through the parallel R_t-CPE combination, is obtained as the sum of the currents through R_t and CPE. Thus the total current through the steel concrete interface can be obtained as

$$I(t)=\left[V_{ERE}(0)A(t)+\int_0^t \frac{dV_{ERE}(\tau)}{d\tau}A(t-\tau)d\tau\right]+\frac{V_{ERE}(t)}{R_t} \tag{3.2}$$

where $V_{ERE}(0)$ refers to the potential jump at the initiation of the scan, A(t) is the step response function obtained by applying a unit Heaviside voltage input. A(t) has been obtained by Sagues et al. (1995) as

$$A(t)=\frac{Y_o t^{-n}}{\Gamma(1-n)} \tag{3.3}$$

The current response of the steel-concrete interface was simulated using the $V_{ERE}(t)$ measured from the linear potential sweep measurements. The values of R_t, Y_o and n obtained from the impedance measurement from the same specimen were used in Equation 3.2. A comparison between the measured and predicted current for typical specimens of series A and B are shown in Figures 3-10 (a) and (b), respectively. The parameters obtained from impedance at multiple frequencies appear to provide a close match for the predicted current in the linear potential scan for the same specimen. The match between the experimental and the predicted values provides a powerful validation for the R_t-CPE representation of the steel-concrete interface for both active and passive steel reinforcement.

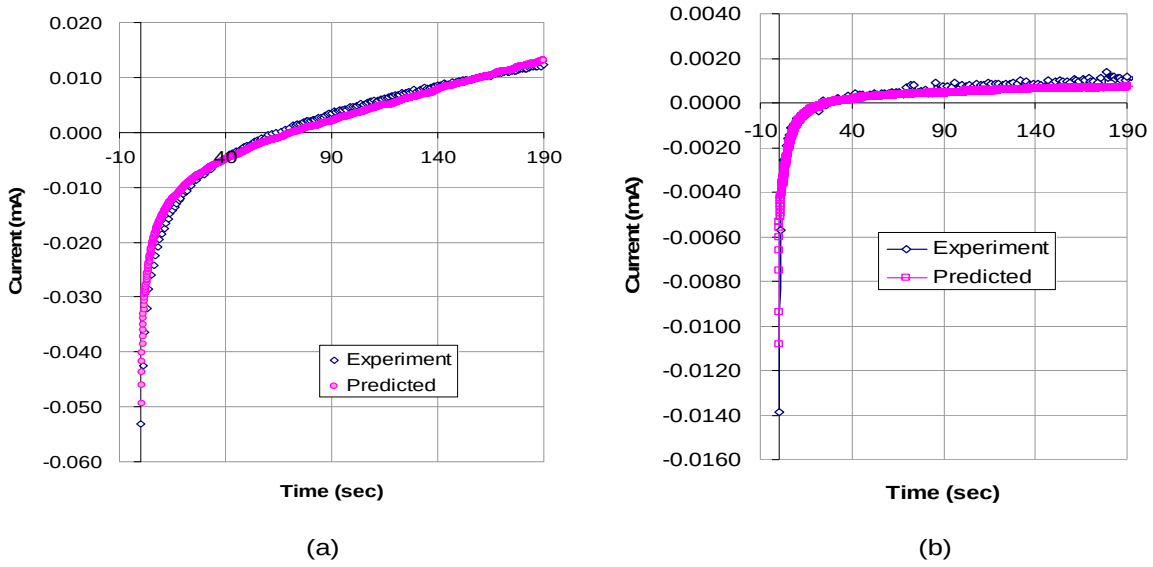

Figure 3-10: A comparison between the measured and the predicted current in a linear potential scan experiment, (a) specimen of Series B. (The values of the parameters: R_t = 1400Ω, Y_o = $0.02\Omega^{-1}s^n$, n = 0.7); (b) specimen of series A (The values of the parameters: R_t = 100000 Ω , Y_o = $0.007\ \Omega^{-1}s^n$, n = 0.9).

It can be seen that there is an almost linear increase in the current between 120 to 180 seconds after the start of the scan. Further, within this time, both V_{ERE} and V_{SCE} are

essentially linear. Therefore, the change in current is directly proportional to the change in the applied potential in this time range. This suggests that after the initial transient response, there is a linear relationship between the applied potential polarization and the measured current. The response of the concrete and the steel-concrete interface can therefore be sufficiently represented using combinations of purely resistive elements within this time period.

3.5 DISCUSSION

The circuit for the steel-concrete interface proposed by Sagues et al (1995) is found to be suitable for modeling its response to transient input. The transient response of the steel-concrete interface can be represented using a charge transfer resistance (R_t) and a CPE which represents the double layer capacitance. Due to factors such as inhomogeneity of the reaction sites and conditions on the steel surface embedded in concrete, the resultant behavior is more closely represented by a non-ideal capacitor. However, for passive steel, the behavior of the interface approaches an ideal capacitor.

Measurements from the concrete surface contain the contributions from concrete superimposed over that of the steel-concrete interface. Since concrete is a very heterogeneous material, this would compound the effect of spatial inhomogeneity of reaction sites on the steel surface. Further, the influence of concrete cannot be clearly deduced from measurements made on concrete surface and it is often difficult to clearly ascribe aspects of the measured response to individual contributions from the concrete and the steel-concrete interface. A comparison of the impedance measurements using

potentials measured on the concrete surface and at the steel-concrete interface proves this point. The diffusive response is evident from the measurements on the surface. This is not witnessed in the measured local response of the steel-concrete interface. The CPE response of the steel-concrete interface is hard to determine from the impedance response obtained by the concrete surface because of the overlapping influence of the apparent diffusive response of concrete.

While the ERE used in this study has previously been used for measuring the potentials of steel embedded in concrete (Phares et al, 2006), the long-term stability of this electrode has not been evaluated. Further, there is a possibility of chloride contamination from the ERE. The measured potentials indicated that the ERE were stable within the period of observations reported in this chapter. There were also no signs of Chloride contamination introduced by the ERE.

Once the response of the steel-concrete interface is understood from local measurements and a proper circuit is ascribed to it, procedures for obtaining the parameters at the steel-concrete interface from external measurements to an external input can be developed. The role of concrete and its influence on external measurements requires careful consideration. The role of internal humidity (dryness) of concrete, in particular, should be evaluated. The internal humidity of concrete may have a significant influence on the CPE and diffusive behavior of the steel-concrete interface. This effect needs to be investigated before procedures for extracting the parameters of the equivalent circuit from external measurements can be developed.

3.6 CONCLUSIONS

From simultaneous potential measurements on the concrete surface and the steel-concrete interface an equivalent circuit representation is developed for the steel-concrete interface. A parallel combination of charge transfer resistance and a constant phase element to represent the double layer capacitance is found to be suitable for both active and passive steel. The main conclusions of the work reported in this chapter are:

1. CPE response is prominent in active corrosion. The value of n for the CPE element was found to be in the range (0.65-0.75).
2. Passive steel exhibits a response which is closer to a pure capacitance.
3. Diffusive response is evident from the measurements on the surface. This is not witnessed from the response of the steel-concrete interface.
4. Concrete has significant influence on the impedance spectrum measured from the concrete surface at both the low and the high frequencies. At low frequencies the presence of diffusion in concrete overlaps with the contribution of the steel-concrete interface.
5. The steel-concrete interface predominantly contributes in the low frequency (at and below 10 Hz) region of the impedance spectrum.

CHAPTER 4
CORROSION IN CRACKED CONCRETE: EVALUATION OF MACROCELL AND MICROCELL RATES USING TAFEL RESPONSE

4.1 INTRODUCTION

The alkalinity of concrete provides good chemical protection to steel against corrosion. Therefore, in the absence of a crack, the steel reinforcement in reinforced concrete structures usually exhibits a prolonged corrosion initiation period (Tutti 1982). The factors influencing corrosion and the methods for determining the rate of corrosion of steel embedded in concrete have been extensively researched (Andrade, 1978, Feliu, 1988, 1989a, 1989b, 1996 and Carino, 1999). Several electrochemical methods for assessing the rate of corrosion, which is assumed to be uniform along the entire length of the steel bar, have also been developed. In these studies, it is implicitly assumed that concrete is a homogeneous material.

Cracks are often introduced in concrete due to the action of loads, restrained shrinkage or thermal gradients (ACI 224R-01). When a crack in concrete intersects the steel reinforcing bar, it provides an easy and fast access for ingress of ions such as chlorides along with oxygen and water to the steel surface, which results is a faster

initiation of corrosion. The main transport mechanism for chloride ingress through a crack is convection due to capillary suction of water, which is faster than the diffusion based-mechanism through concrete cover (Arya 2000). Therefore a crack in concrete introduces a spatial variation in the concentrations of oxygen and chloride ions along the length of steel bar. Formation of crack also produces a discontinuity in the material medium which introduces a barrier for ionic conduction and diffusion of ions across the crack opening. The combined result of these two effects is a spatial inhomogeneity in the electrochemical state of steel along the length of the steel bar. The conditions at steel in the vicinity of the crack favor active corrosion while steel away from the crack remain in a passive state (Raupach 1995).

Relatively little work has been done to study corrosion of steel embedded in cracked concrete. A crack has been shown to produce spatial variations in the potential and the rates of corrosion along the length of the steel bar (Arya 1995, Schiessl and Raupach 1997). The rate of metal loss has been shown to increase significantly in the vicinity of flexural cracks, which intersect the main reinforcement (Otsuki, 2000). Two different mechanisms of corrosion, microcell and macrocell, have been identified in cracked concrete specimens (Arya 1995, Raupach, 1996, Schiessl and Raupach 1997 and Sagues 1996). The two mechanisms primarily differ in the length scales and the physical distance between the underlying reactions. In the microcell mechanism the anodic and cathodic reaction sites are microscopic in size and are located adjacent to each other. Microcell

corrosion produces uniform removal of the steel. In macrocell corrosion, anode and cathode are spatially separated resulting in a galvanic flow of current. In the case of chloride induced corrosion, the anodic reaction is localized, confined to the area of steel where the critical chloride content for depassivation is exceeded. The cathodic reaction may occur in all areas that are not permanently water-saturated (Schiessl and Raupach, 1997). The sites of anodic and cathodic reactions have been observed to be up to a few meters apart (Raupach, 1996). In cracked beams it has been observed that the macrocell corrosion process continues through the formation a small anode located at the crack, which is supported by a large cathode comprising of passive steel in the uncracked concrete around the crack (Schiessl and Raupach 1997). The formation of a macrocell has been shown to result in intense localized metal loss at the anode. At reinforcing bars intersecting flexural cracks, the macrocell rate has been estimated to be up to 70 times higher than the uniform corrosion rate (Otsuki, 2000).

Some studies on the influence of geometric and material parameters on the rate of corrosion in cracked concrete have been reported. Cover depth and quality of concrete have been shown to significantly influence the corrosion rate obtained from the macrocell mechanism. The corrosion rate in cracked concrete was reduced on increasing the concrete quality, increasing the cover depth and addition of a corrosion inhibitor (Berke 1991 and 1993, Raupach 1996). The macrocell corrosion current was found to increase with the crack width (Raupach 1996). Arya (1996) studied the relationship between crack

frequency and reinforcement corrosion and found that decreasing the frequency of cracking resulted in a decrease in total corrosion.

From our current understanding, when there is a crack in the concrete along the length of the steel bar, the total dissolution of steel at the crack is determined by both the macrocell and microcell corrosion processes that might coexist (as shown in Figure 4-1). In this chapter, inhomogeneous corrosion along the length of a steel bar resulting from combined micro and macrocell corrosion reactions is referred to as the macrocell corrosion system. A clear understanding of the relative magnitudes of the microcell and macrocell mechanisms in a macrocell system is currently not available. The role of the microcell mechanism, its contribution to the total metal loss and the relation between the micro and macrocell corrosion rates in terms of the fundamental electrochemical principles are yet not clear. A fundamental comprehension of the state of the macrocell system in terms of the kinetics of the underlying reactions and methods for predicting the contributions of these two mechanisms to the local rate of metal loss also do not exist.

In this chapter, the results of an experimental investigation into the macrocell corrosion system in steel bar in cracked concrete are presented. A corrosion cell comprised of segmental steel bar embedded in concrete with external electrical connections was designed. The potential of the steel bar was monitored using embedded reference electrodes placed close to the steel bar. Prior to establishing the connection, the polarization response of the individual segments, were obtained experimentally to study

the Tafel response. Once connected, the spatial variation in the potential and current along the steel bar were measured. The measured flow of current between the different segments indicated that the steel bar at the location of the crack acts as the macrocell anode while the steel bar located away from the crack is the macrocell cathode. From the measurements of potentials and currents in the system, a representation of the final state of the system is developed using the polarization responses of active and passive steel. A relationship between the microcell and macrocell corrosion at the macrocell anode is developed considering the Tafel behaviors of the active and passive steel. The macrocell potentials of the segments were predicted using the measured macrocell current and the polarization responses of the individual segments.

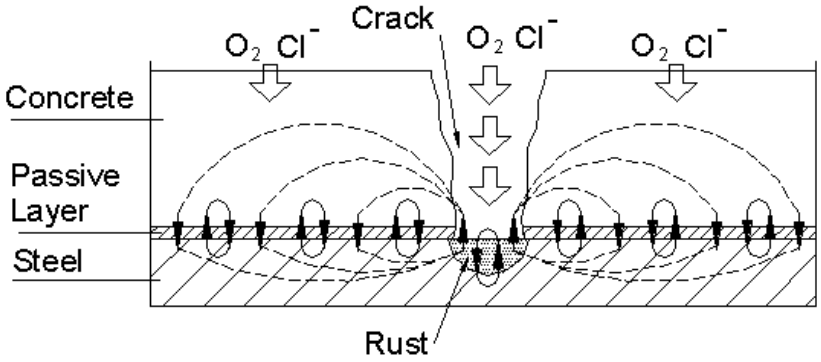

Figure 4-1: Schematic representation of the micro and macro-cell reactions in a steel embedded in cracked concrete.

4.2 OBJECTIVES

The objectives of the work presented in this chapter are

1. To investigate the macrocell corrosion mechanism in cracked concrete using a model macrocell
2. To predict the macrocell response of a steel bar embedded in cracked concrete using the polarization responses of active and passive steel.
3. To evaluate the relative contributions of the macro and micro cell components to the total corrosion of steel located in cracked concrete.

4.3 EXPERIMENTAL STUDY

4.3.1 Materials and Methods

The specimen geometry and dimensions of the concrete specimen are shown in Figure 4-2. An artificial crack was introduced using a plastic insert placed in the middle of the specimen. A segmental steel bar with nine segments was used. The central segment, labeled A, was positioned such that it was centered on the crack. The other segments, labeled C1 to C8, were positioned symmetrically on either side of the central segment. The segments were electrically isolated along the length using Teflon disks. The lengths of segments marked as A, C1, C2, C3 and C4 were equal to 5.1 cm, 7.6 cm, 10.2 cm, 12.7 cm and 15.2 cm, respectively. The segments were connected to external switches such that the electrical connections between the segments could be controlled from the outside (as shown in Figure 4-2).

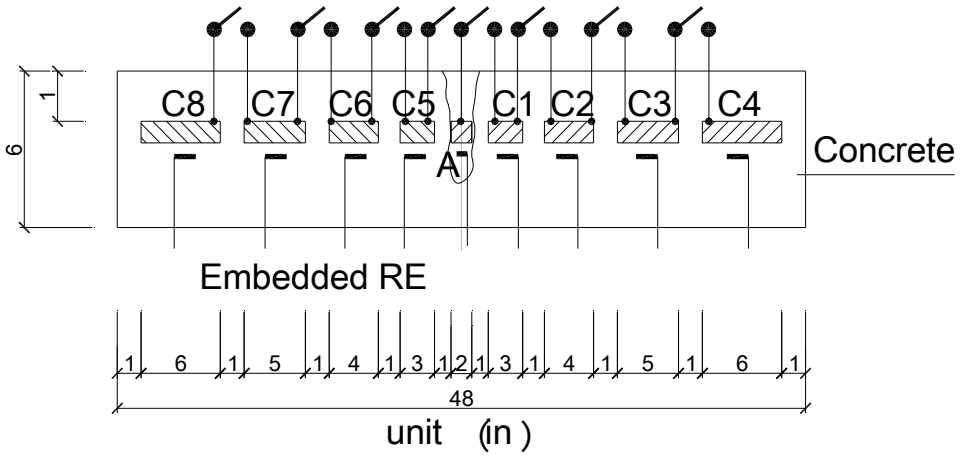

Figure 4-2: Schematic representation of the cracked concrete specimen used in this study.

Type I Portland cement (ASTM C 150) was used for all specimens. The concrete mixture proportions by weight were 1.0 (cement): 1.7 (sand): 2.42 (aggregate) and the water/cement ratio was 0.45. Ordinary tap water was used for mixing the concrete. Coarse aggregate comprised of 10 mm gravel. Air entraining agent, meeting the requirements of ASTM C 494, was also used at the recommended dosage to achieve 6% entrained air content.

The concrete cover depth was equal to 25.4 mm. Plain carbon steel bars with diameter equal to 12.7 mm were used. The steel bars were cleaned with acetone and polished using 600-grit Sic chapter. Electrical connections were made with each steel bar by soldering a copper wire close to one of its ends. Embedded Ag/AgCl reference electrodes were installed close to each steel segment prior to placing the segmental bar in the form. The embedded reference electrode is referred to “ERE” in this thesis.

The specimen was demolded 24 hours after casting and cured in a 100% relative

humidity (RH) chamber for 90 days following which it was subjected to periodic wetting and drying cycles. Each wetting-drying cycle involved three days of wetting followed by a four-day drying period. During wetting, the specimen was subjected to 100% RH at 23ºC. Drying comprised of exposure to the laboratory environment, which was maintained at 50% RH and 23ºC. At 90 days of age, the specimen was subjected to 3-point flexural loading to initiate a crack along the plastic insert. During the loading procedure, as the crack faces moved apart, the plastic insert was pulled out from the concrete. A photograph showing the closeup view of the crack, which initiated from the notch created by the plastic insert, after unloading the specimen is shown in Figure 4-3. The crack width was measured at three locations on the surface of the concrete beam using a hand-held microscope which provides 50X magnification. The crack widths were measured on the front and the back faces. The average crack widths at depths equal to 0 cm, 4 cm and 6.5 cm from the top of the beam are equal to 0.6, 0.4 and 0.2 mm, respectively. The specimen was unloaded and the wetting-drying cycles were continued for the duration of testing.

Figure 4-3: Photograph showing a closeup view of the crack originating from the plastic insert.

4.3.2 Measurement Procedures

Initially, potential measurements were performed with the external switches in open positions. This configuration is referred to as the “open mode”. Initially, half-cell potential of each segment (A, C1 to C8) was monitored at the end of each drying period using both the ERE and a saturated calomel reference electrode (SCE) placed on the concrete surface. Before each measurement, the concrete specimen was covered with a thin sponge soaked in 3% NaCl solution. When the half-cell potentials recorded from the different segments were found to be stable (values were constant after several wetting-drying cycles), polarization tests were conducted for each individual segment.

Measurements included linear polarization resistance (LPR) and Tafel behavior. The polarization measurements were conducted using a stainless steel counter electrode (CE). The tests were conducted using a PAR 2263™ Potentiostat/Galvanostat. For LPR measurements, potential scans were initiated 10 mV below the rest potential up to a value 10 mV above the rest potential at a scan rate of 0.1 mV/s. Tafel measurements were performed at a rate of 10 mV/minute. For the steel segments located away from the crack (C1 through C8), the Tafel behavior was obtained under cathodic polarization[1] up to 300 mV below the rest potential. The Tafel behavior of the steel segment at the crack (segment A) was obtained under anodic[2] polarization up to 200 mV above the rest potential.

Following the polarization tests, the potentials of the individual segments were monitored for four additional wetting-drying cycles. The electrical connections were then established between the segments at the end of the wetting period of the fourth wetting-drying cycle. The configuration where all the adjacent segments are electrically connected is referred to as the "closed mode". After connecting the steel segments, transient current between the individual segments were continuously measured and recorded. Continuous measurements were performed until the end of the drying period of the same cycle. Following this, the data acquisition system was disconnected without

[1] Anodic polarization: the potential is changed in the anodic (or more positive direction) causing electrons to be withdrawn from the working electrode.

[2] Cathodic polarization: the working electrode becomes more negative and electrons are added to the surface, in some cases causing electro-deposition.

affecting the electrical connections. The electrical contacts were kept in a waterproof container when the specimen was introduced into the chamber for wetting. The current was measured at discrete points of time during each subsequent drying period.

The setup for measuring the macrocell current through each segment in the closed mode is shown in Figure 4-4. The electrical connections between the segments were established using 10 Ohm precision resistors. The current between the segments was determined by dividing the potential drop measured across the resistor by the magnitude of the resistance. During the continuous measurements, data were collected using a high speed data acquisition system (IOtech^{TM} WaveBook^{TM}). Channels, labeled as Ch1 to Ch8, were used to collect the potential drop across the precision resistors. All channels were simultaneously sampled, discretized and recorded at a sampling rate equal to 10 Hz. Current measurements during drying periods within subsequent wetting-drying cycle were made manually. Potentials across the precision resistors and the half-cell potentials were measured using a high-precision, hand-held multi-meter.

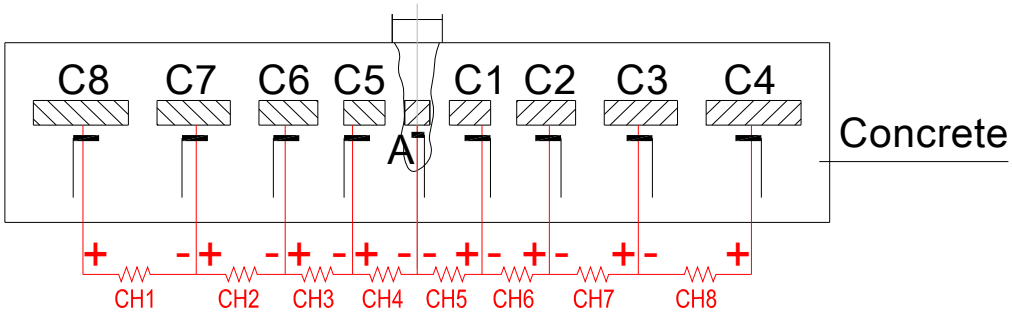

Figure 4-4 Test setup for macrocell current measurement.

4.4 EXPERIMENTAL TEST RESULTS

The experimental results from the measurements performed on specimens in the open and closed modes are presented in this section.

4.4.1 Open Mode Measurements and Data Processing

Half-cell and polarization measurements were performed on individual segments in the open-mode configuration.

Half-cell Measurements in the Open Mode

The potentials of the individual segments at different instances of time after introducing the crack are shown in Figure 4-5. The potentials obtained using an SCE placed on the concrete surface are plotted in the figure. In the open-mode, the potentials of the individual segments were found to reach stable values 6 months after introducing the crack. The potentials remained relatively constant with continued wetting-drying cycles. In the stable states, the differences in the steady half-cell potentials of the segments C1 through C4 and C5 through C8 were not significant. There was however a large difference in the potentials of the segment located at the crack when compared with the potentials of the segments away from the crack.

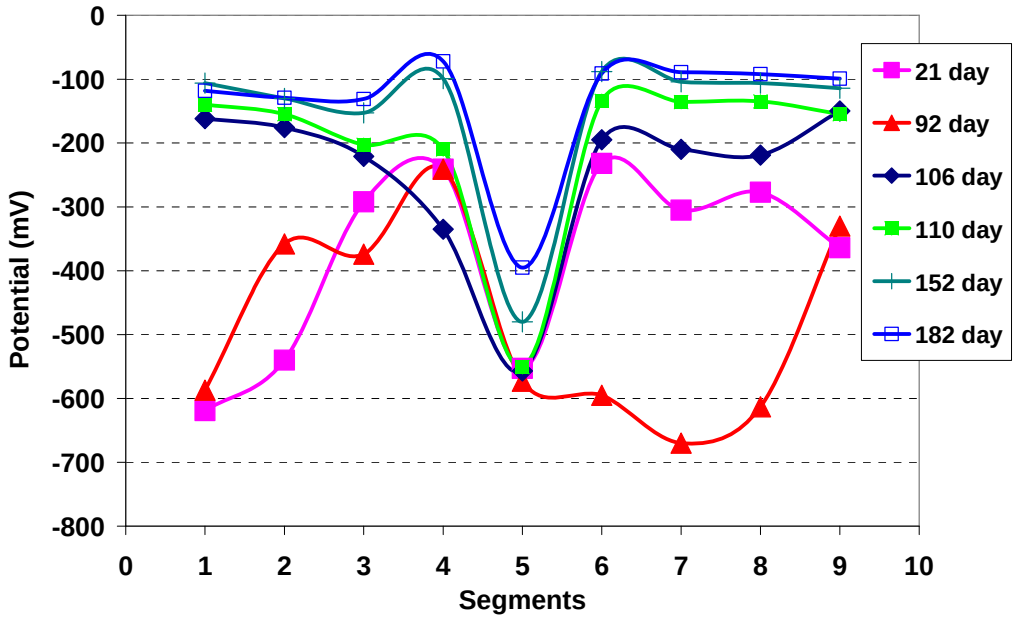

Figure 4-5: Half-cell potentials of the different segments in the open mode.

The potentials of the different segments obtained using both the SCE and the ERE, six months after introducing the crack are shown in Figure 4-6. It can be seen that the potentials obtained using both reference electrodes are consistent. In the open mode, the potential difference between the segment at crack and segments away from crack is in the range 250 ~ 300 mV. The measured potentials from the open mode suggest that the steel segment at crack is undergoing active corrosion while the steel segments away from the crack are in a passive state.

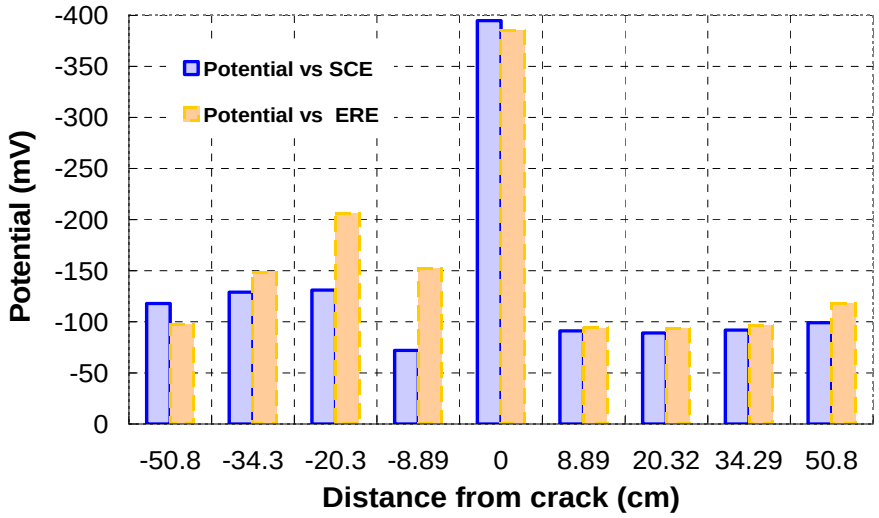

Figure 4-6: The potential profile of segments in open mode

LPR Measurements in the Open Mode

Typical polarization response from segment A, six months after introducing the crack is shown in Figure 4-7. The potential ramp was applied in the vicinity of the rest potential measured using the SCE on the concrete surface. A plot of the potential versus the total applied current is shown in the figure. The polarization resistance, R_p, was determined using the procedure proposed by Gonzalez et al. (1985). According to this procedure, the slope of the curve at the beginning of potential scan is equal to $R_e^{/}$ and the slope close to the peak of the ramp is equal to $(R_e^{/}+R_p^{/})$. $R_e^{/}$ and $R_p^{/}$ denote the total effective resistance of the medium and the total polarization resistance of the steel. Linear polarization resistance, R_p, is obtained by multiplying the $R_p^{/}$ with the surface area of the polarized steel bar.

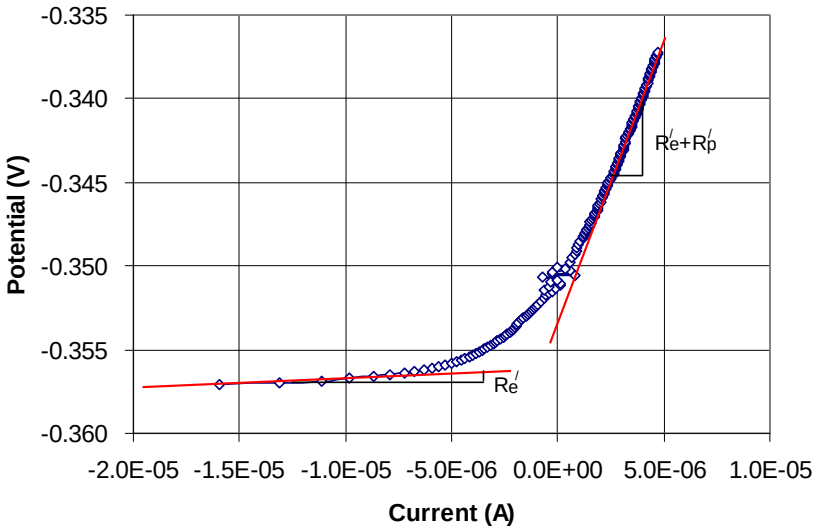

Figure 4-7: Typical polarization curve obtained from segment A

Polarization scans were performed using both ERE and the SCE as reference electrodes. The average values of R_p and R_e obtained from the potential sweep measurements of all the segments are listed in Table 4-1. The magnitude of R_e at the location of the crack is comparable to the value of R_e obtained for concrete. It should be noted that the low value of R_e obtained for concrete indicates a conductive medium. It can be seen that the values of R_p for all the segments obtained using ERE and SCE are comparable. Further, R_p of segment A is in the order of 10^4 Ωcm^2. This value is consistent with reported values by Feliu and Gonzalez (1989) for steel undergoing active corrosion resulting from uniform microcell mechanism. The magnitude of R_p of steel away from crack is in the order of 10^6 Ωcm^2, which is consistent with the findings of Feliu and Gonzalez (1989) for steel in a passive state. The values of R_p are also in agreement with the recorded half-cell potentials in indicating the active and passive states of the steel bars

Table 4-1: R_e and R_p values of segments A and C from LPR measurements

		A	C1 and C5	C2 and C6	C3 and C7	C4 and C8
From SCE	R_e (Ω)	250	220	300	260	250
	R_p (Ωcm^2)	2.9e4	3.2e6	2.2e6	2.5e6	2.8e6
From ERE	R_e (Ω)	240	320	170	280	250
	R_p (Ωcm^2)	3.0e4	2.4e6	2.5e6	2.0e6	1.9e6

Tafel Behavior in the Open Mode

Typical Tafel behaviors of segments A and C2 under cathodic and anodic polarization, respectively are shown in Figures 4-8(a) and (b), respectively. During the test, the potential of the working electrode was measured using the SCE reference electrode on the concrete surface. From the measured response it appears that there is no deviation from the Tafel slope even at a large polarization. There is no indication of the influence of concentration polarization on the Tafel behavior. The Tafel behaviors of the individual segments C1 through C8 were nominally similar. The values of Tafel constants, exchange current densities and rest potentials for the different segments are compiled in Table 4-2. For segment A, the Tafel constant, exchange current density and rest potential are identified as β_m, i_{corr}^{A} and E_{corr}^{A}, respectively. The average and standard deviation of values obtained from multiple scans are given in the table. For segments C1 through C8, the Tafel constant, exchange current density and rest potential are identified as β_Z^*, $i_{O,C}$ and $E_{O,C}$, respectively. The average and standard deviation of the values of these constants obtained from all the segments and from multiple scans are provided in the

table.

Table 4-2: Values of the Tafel parameters in open mode

	Segments C			**Segment A**		
	$E_{O,C}$ (mV)	$i_{O,C}$ (μA/cm^2)	β_Z^* (mV/ Decade)	E_{corr}^A (mV)	i_{corr}^A (μA/cm^2)	β_m (mV/ Decade)
Average	-67.7	0.0166	205.0	-398.0	1.182	434.7
Standard Deviation	17.5	7.8e-4	21.0	38.4	0.164	36.9

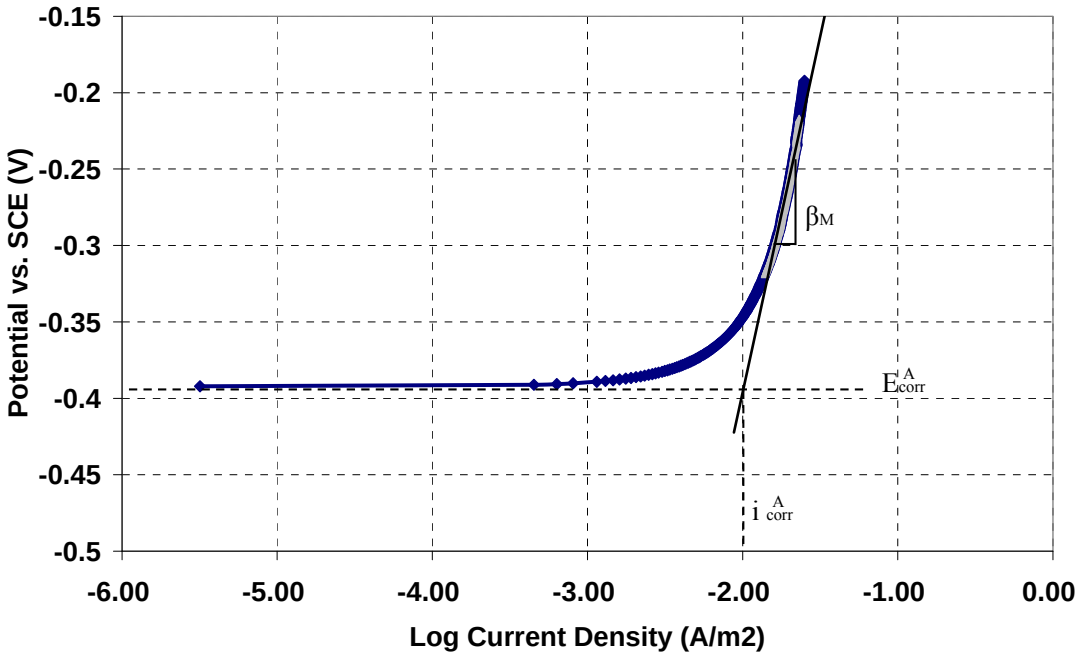

(a)

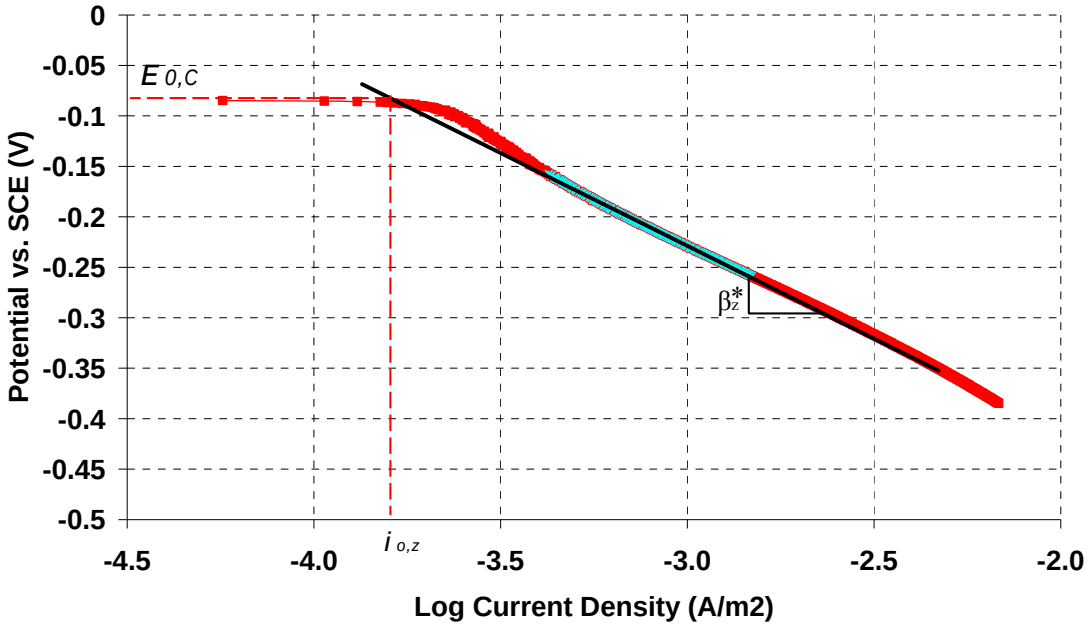

Figure 4-8: Tafel response (a) of Segment A (b) of Segment C2

4.4.2 Closed Mode Measurements and Data Processing

Electrical connections were established immediately at the end of a wetting period within a wetting-drying cycle. After establishing the electrical connections, transient current was recorded continuously till the end of the drying period. The collected data was filtered using a Butterworth filter to remove high frequency noise. Current measurements were obtained at the beginning, in the middle and at the end of each drying period in subsequent wetting-drying cycles.

Corrosion Macrocell measurements in Closed mode

The total macrocell current measured within the first drying period after connection

is shown in Figure 4-9. The total macrocell current is the sum of the currents measured between segment A and C1 (I_1) and segments A and C5 (I_2). It can be seen that immediately after connection, there is a large current, approximately 340 μA, which flows between the segments. There is a gradual decrease in the measured macrocell current with time. The value of the macrocell current appears to reach an asymptotic value approximately equal to 24 μA after 100,000 seconds. It appears that after 100,000 seconds, there is no significant change in the macrocell current up to the end of the drying period. In this macrocell, the direction of current flow indicated that segment A acts as the anode and segments C1 through C8 on either side of the crack form the cathode. The total current at the end of the drying period was equal to 24 μA (0.024 mA).

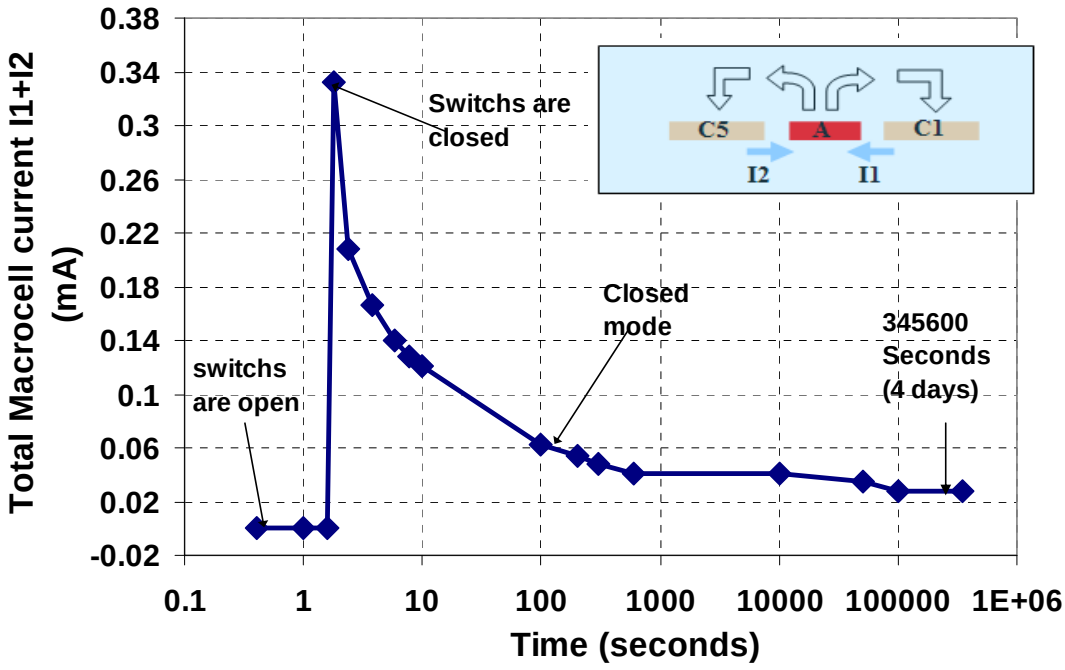

Figure 4-9: The transient behavior of total macrocell current between steel segments.

The currents I_1 and I_2 measured during the drying period of different wetting-drying

cycles in the closed mode are shown in Figure 4-10. It can be seen that the macrocell currents on either side of the crack steadily increase with the number of wetting and drying cycles and appears to reach a steady state value after 35 days. It can be surmised that the macro-cell attains a steady state when the values of current are approximately constant within drying periods of successive wetting-drying cycles. The steady state current between the anode and the cathodes located on either side is approximately equal to 20 μA. There was a slight variation in the measured current at beginning and the end of the drying period within one wetting and drying cycle. These differences could be attributed to minor changes in the concrete moisture condition and resistivity with drying. The steady-state macrocell current distribution between the different segments measured at the end of the drying period of the wetting-drying cycle is shown in Figure 4-11. The current entering each segment has been calculated as the difference of the measured current at the two ends.

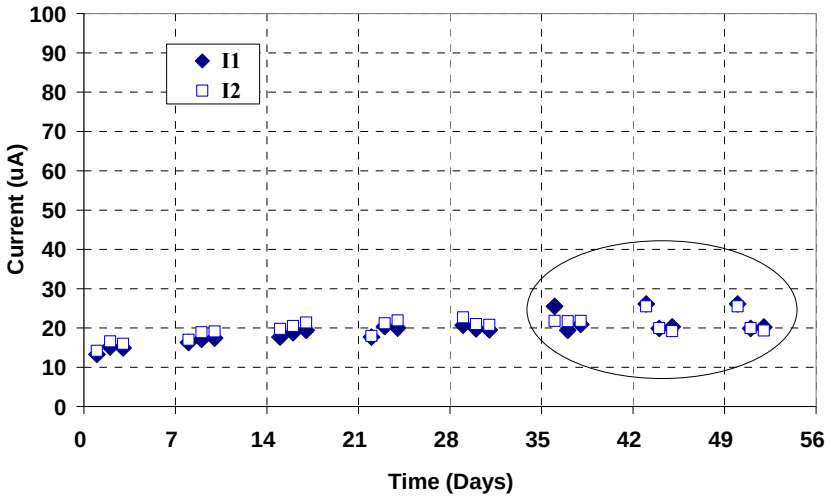

Figure 4-10: Time history of measured macrocell current

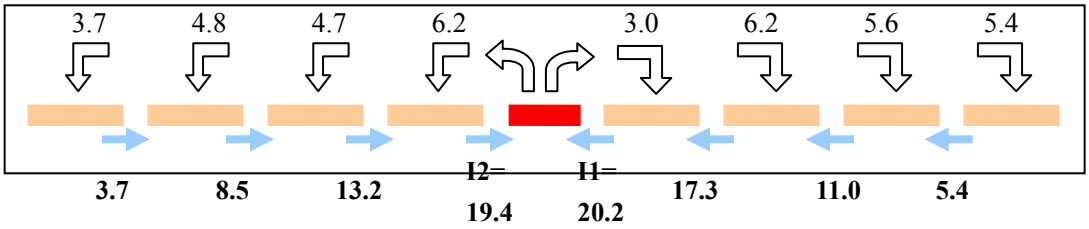

Figure 4-11: Steady-state macrocell current distribution in the specimen

Once the measured currents indicated a macro-cell steady-state, the potentials of the segments were measured. The values of potentials recorded using the embedded ERE after 56 days in the closed mode are shown in Figure 4-12. The open-mode potentials are also plotted in the figure for comparison. The shift away from the potential in open configuration is apparent from the graph. At macrocell steady state, the potential difference between segment A and segments C1 through C8 decreases when compared to the open mode. The potential difference between the different segments of the cathode does not appear to be significant. The average values of the potentials obtained at the end of two wetting drying cycles at steady state are shown in Table 4-3. It can be seen that the potential of the steel segment A is elevated above the potential associated with active microcell corrosion (obtained previously in the open state). The potential of the segments C1 through C8 are depressed below the potential for passive steel in concrete (obtained previously in the open mode). The potential difference between the anode and the average potential of the cathodes can be taken to be a constant value equal to 52 mV.

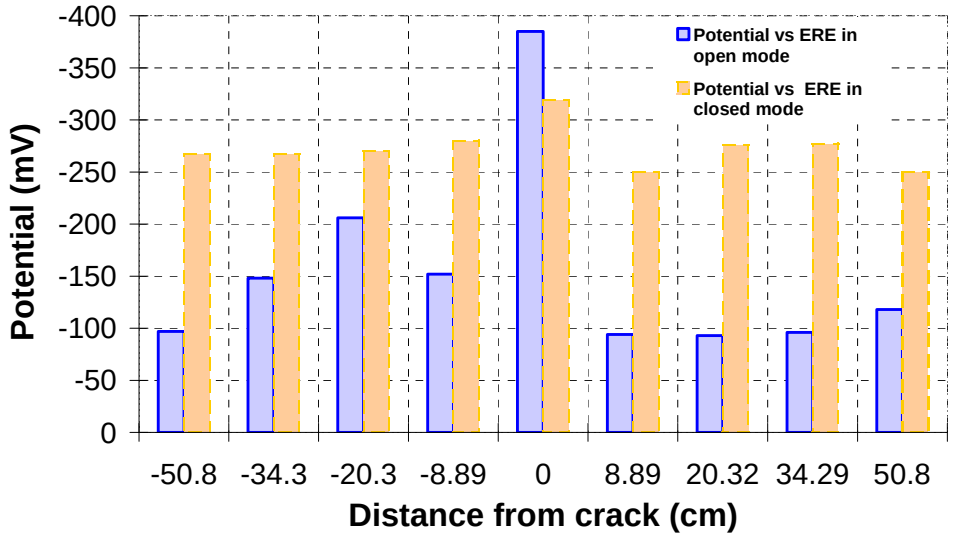

Figure 4-12: Half-cell potential profile of specimen at open and closed mode.

Table 4-3: Half-cell potentials of segments at macro-cell steady state

Potential\segment	C8	C7	C6	C5	A	C1	C2	C3	C4
By ERE (mV) (closed mode)	-267	-267	-270	-280	-319	-250	-276	-277	-250
By ERE (mV) (open model	-97	-148	-206	-152	-385	-94	-93	-96	-118

4.5 ANALYSIS OF RESULTS

The current recorded at the end of the drying period after several wetting-drying cycles indicates that the system attains a steady state. The state of the system at the end of the drying period can thus be treated as a fixed state for the purpose of analysis. At this stage, the steel at the crack is polarized anodically away from its rest potential in the open mode. Similarly the steel away from the crack is polarized cathodically away from its rest potential. Since steel in active and passive states have well-defined polarization behavior

obtained in the Tafel plots, the response of the entire system can be predicted using the individual polarization behaviors of active and passive steel inside concrete. An interpretation of the observed macrocell in terms of the polarization responses of the active corroding steel located at the crack and the passive steel located away from the crack is now attempted. The polarization response of the individual segments before connection are examined and used to predict the state of the system after connection.

4.5.1 State before Connection

The polarization response of the active and the passive steel embedded in concrete are examined using the Evans diagram for each. The relationship between the applied over-potential and the current densities in each electrode are studied.

Response of the Passive Steel to Applied Over-Potential

In the open mode, the passive steel located away from the crack can be classified as a non-corroding electrode (Stern and Geary 1957). In such an electrode, at equilibrium the current densities associated with oxidation ($\vec{i}_Z^*$) and reduction ($\overleftarrow{i}_Z^*$) are equal and may be expressed in the form

$$\vec{i}_Z^* = \overleftarrow{i}_Z^* = i_{0,C} \tag{4.1}$$

where $i_{0,C}$ is the exchange current density. The potential of the cathode at equilibrium is defined as equilibrium potential or rest potential ($E_{0,C}$). When the reaction rate is controlled by activation energy, the relationship between current density and potential (E)

may be written as

$$E = E_{0,C} - \beta_Z^* \log\left(\frac{\vec{i}_Z^*}{i_{0,C}}\right) \tag{4.2a}$$

$$E = E_{0,C} + \beta_Z^* \log\left(\frac{\overleftarrow{i}_Z^*}{i_{0,C}}\right) \tag{4.2b}$$

where β_Z^* is the Tafel constant. Figure 4-13 illustrates the relationship between the oxidation and reduction rates and the exchange current density at equilibrium potential and the effect of overpotential on the rates of the individual reactions. The difference between the oxidation and reduction currents is equal to the applied cathodic current, i_{app}^C such that

$$i_{app}^C = \vec{i}_Z^* - \overleftarrow{i}_Z^* \tag{4.3}$$

The cathodic polarization response which gives the relationship between i_{app}^C and E is given as

$$E = E_{0,C} - \beta_Z^* \log\left(\frac{i_{app}^C + \overleftarrow{i}_Z^*}{i_{0,C}}\right) \tag{4.4}$$

If E is sufficiently removed from the equilibrium potential $\overleftarrow{i}_Z^*$ becomes insignificant.

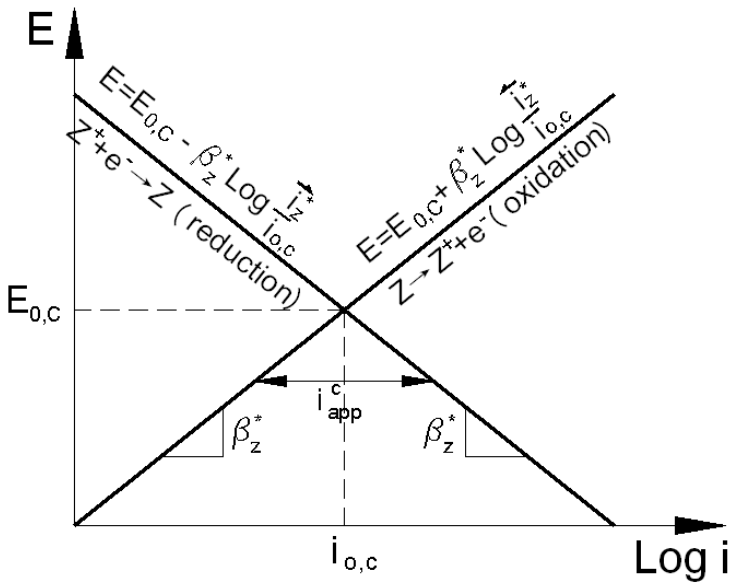

Figure 4-13: Relationship between voltage and current for the anode and cathode reactions of a non-corroding electrode system.

Polarization Response of the Steel Undergoing Active Microcell Corrosion

In the open mode, the steel segment located at the crack undergoes active microcell corrosion and can be considered to be a corroding electrode (Stern and Geary 1957). There are now two co-existing electrochemical reactions corresponding to the oxidation-reduction system of the metal (iron) and the oxidation-reduction system of second (the reducing) species.

$$M \Leftrightarrow M^{+} + e^{-} \tag{4.5a}$$

$$Z^{+} + e^{-} \Leftrightarrow Z \tag{4.5b}$$

For corrosion of steel embedded in concrete, the two reactions involved have been identified as the oxidation of iron and the reduction of Oxygen, respectively (Raupach, 1996).

$$F_e \Leftrightarrow F_e^{2+} + 2e^- \quad \text{and} \quad \frac{1}{2}O_2 + H_2O + 2e^- \Leftrightarrow 2(OH)^- \tag{4.6}$$

Each reaction has its own exchange current density and Tafel slope as shown in Figure 4-14.

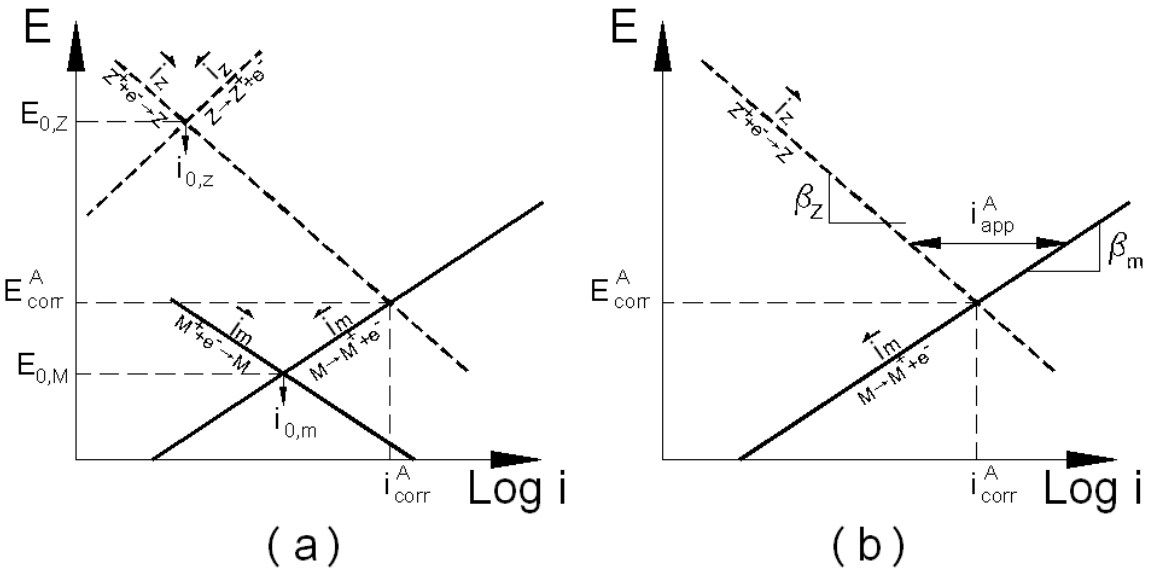

Figure 4-14: (a) Relationship between potential and current density of a corroding electrode system consisting of two co-existing electrochemical reactions.

(b) Simplified relationship ignoring $\vec{i}_m$ and $\overleftarrow{i}_Z$

The potential-current relationship for each reaction can be expressed as

Z reduction : $E = E_{0,Z} - \beta_Z \log\left(\frac{\vec{i}_Z}{i_{O,Z}}\right)$ and Z oxidation: $E = E_{0,Z} + \beta_Z \log\left(\frac{\overleftarrow{i}_Z}{i_{O,Z}}\right)$

Metal reduction: $E = E_{0,M} - \beta_M \log\left(\frac{\vec{i}_M}{i_{O,M}}\right)$ and Metal oxidation: $E = E_{0,M} + \beta_M \log\left(\frac{\overleftarrow{i}_M}{i_{O,M}}\right)$

where $\vec{i}_m$ is the rate of reduction of Fe^{2+}, $\overleftarrow{i}_m$ is the rate of oxidation of Fe, $\vec{i}_Z$ and $\overleftarrow{i}_Z$

are the rates of reduction and oxidation of the species Z, respectively. β_z and β_m are the Tafel constants of the individual reactions.

The steady state corrosion potential (E_{corr}^{A}) can be obtained from the two reactions considering

$$\vec{i}_Z + \vec{i}_m = \bar{i}_Z + \bar{i}_m \tag{4.7}$$

When the corrosion potential is sufficiently removed from equilibrium potential the individual reduction $\vec{i}_m$ and $\bar{i}_Z$ become insignificant in comparison to $\bar{i}_m$ and $\vec{i}_Z$. This has been shown to be the case for the corrosion of steel in concrete (Stern and Geary, 1957). Thus at equilibrium, the corrosion current density is obtained as

$$\vec{i}_Z = \bar{i}_m = i_{corr}^{A} \tag{4.8}$$

where i_{corr}^{A} is the corrosion current density.

The relationship between the potential (E) and applied current for a corroding system under anodic polarization can be obtained considering the metal oxidation and the supporting reduction reaction.

$$E = E_{corr}^{A} + \beta_m \log\left(\frac{i_{app}^{A} + \bar{i}_z}{i_{corr}^{A}}\right) \tag{4.9}$$

where i_{app}^{A} is applied anodic current density.

4.5.2 State after Connection

The galvanic response obtained after electrically connecting segment A with segments

C1 through C8 can now be obtained considering the overpotential response of the active and passive steel. The state of the system comprising the corroding and non-corroding electrodes at macrocell steady state is predicted assuming:

(a) The potential of macrocell cathode is uniform across the length of the cathode.

(b) The polarization response of all segments of cathode is identical.

(c) The entire length of segment A acts as the macro-cell anode.

(d) The current density across the entire Segment A is uniform.

The Potential–current density relations for the active steel at the crack and the passive steel away from the crack are plotted in Figure 4-15. The values of β_Z^*, $i_{0,C}$ $E_{0,C}$, β_m, i_{corr}^A and E_{corr}^A from Table 4-2 for the anodic and cathodic segments from the experimental Tafel response measurement were used in the plot. The value of β_z for Segment A was estimated from the measured R_p and β_m using the relationship

$$R_p = \frac{\beta_m \beta_z}{I_{corr} 2.3(\beta_m + \beta_z)} \tag{4.10}$$

Considering R_p=2.9e4 Ωcm^2, I_{corr}= 23.9 μA (from Table 4-1), Area of A=20 cm^2 and β_m = 434 mV/decade (from Table 4-2), the value of β_z, for Segment A was calculated to be 99 mV/decade.

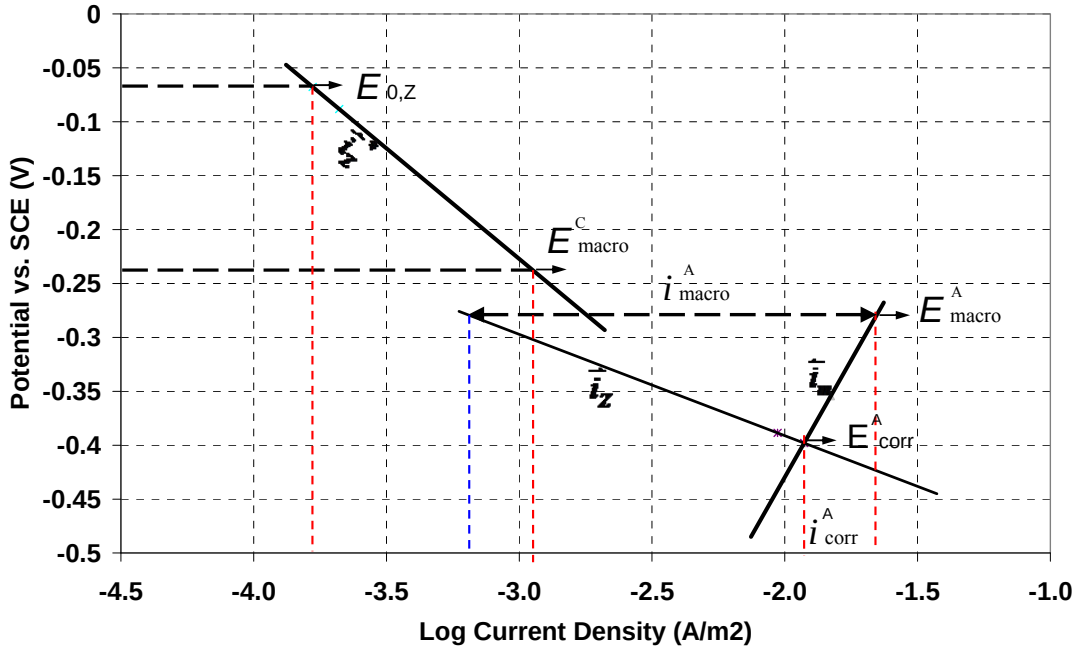

Figure 4-15: E-i relationship of reaction pair at anode and cathode at macrocell steady state.

At the macrocell steady state, the total galvanic current flowing through the anode is equal to the total galvanic current through the entire length of cathode, given as

$$(\vec{i}_Z^{\,*} - \vec{i}_Z^{\,*})A_{cathode} = (\vec{i}_m - \vec{i}_Z)A_{anode} = I_{macro} \tag{4.11}$$

where A_{Anode} and $A_{Cathode}$ are the areas of the anode and the cathode, respectively and I_{macro} is the total macrocell current.

Since the exchange current density of the cathode is insignificant compared to the exchange current density of the anode, if the potential of the cathode is sufficiently removed from its rest potential, the $\vec{i}_Z^{\,*}$ can be ignored. The condition at macrocell

steady state can now be written as

$$(\vec{i}_Z^{\,*})A_{cathode} = (\bar{i}_m - \vec{i}_Z)A_{anode} = I_{macro} \quad (4.12)$$

Using this condition, the potentials for the individual reactions at the macrocell steady state can now be predicted. Considering the measured steady state, macrocell current equal to 40 μA, the final state of the system is shown in Figure 4-15. The predicted potentials obtained from the polarization responses of the anode and the cathode, are equal to -280 mV and -240 mV, respectively. This indicates a steady state potential difference between the anodic and cathodic segments equal to 40 mV which compares favorably with the measured value of 52 mV. The difference between the potential measured experimentally and the corresponding value obtained from the Tafel response can be attributed to the simplifying assumptions used in the analysis.

At macrocell steady state

$$I_{macro} = i^A_{macro} A_{anode} \quad (4.13)$$

where i^A_{macro} is the macrocell current density at the anode and is equal to the i^A_{app} from the polarization response of a corroding electrode. Therefore, at the anode in the macrocell steady state,

$$\bar{i}_m = i^A_{macro} + \vec{i}_Z \quad (4.14)$$

where $\bar{i}_m$ represents the rate of metal loss. In the macrocell, the oxidation of Fe is supported by both the macrocell current (i^A_{macro}) and the reduction reaction associated with

the local microcell ($\vec{i}_Z$). The microcell current density which corresponds to a local balance of oxidation and reduction reactions at the anode is equal to $\vec{i}_Z$. If the potential of the anode, E^A_{macro}, is sufficiently removed from E^A_{corr}, then $\vec{i}_Z$ becomes insignificant in comparison to $\vec{i}_m$. In this situation, the microcell contribution to the corrosion at anode is insignificant. Using a similar argument, it can be shown that the rate of microcell at the cathode is equal to $\vec{i}^*_Z$. However since $\vec{i}^*_Z$ is insignificant compared to $\vec{i}^*_Z$, it can be assumed that the current density at cathode is entirely associated with the macrocell.

The microcell and macrocell currents at the anode and cathode were calculated and are shown in Table 4-4. The current densities were calculated using equation (4.14) and the total currents were obtained by multiplying the current densities by the areas of the respective steel segments. The microcell current densities obtained in the open mode were also calculated and multiplied with the areas of the segments to obtain the total current. These values are also listed in the table for comparison. It can be seen that at macrocell steady state, there is a significant decrease in the microcell corrosion rate at both anode and cathode. The microcell current at cathode dropped from 0.66 μA to 0 μA (insignificantly small) when the macrocell was formed. Microcell current at anode decreased from 23 μA to 1.3 μA. The macrocell current of cathode however increased from 0 to 4.5 μA while the macrocell current at anode increased from 0 to 40 μA. At the macrocell steady state the ratio of macrocell component to microcell component in anode was 31. The ratio of the macrocell current to the microcell current at the macrocell anode

appears to compare favorably with the value estimated by Otsuki et al (2000).

Table 4-4. Comparison of Macrocell component and microcell currents

		Microcell current (μA)	**Macrocell current (μA)**	**Ratio of i_{macro}/i_{micro}**
Cathode C2	In open mode	0.66	0	0
	In close mode	0	4.5	
Anode A	In open mode	23	0	0
	In close mode	1.3	40	31

4.6 DISCUSSION

Analysis in Section 4.5 demonstrates that the macro-cell response of steel in cracked concrete can be predicted with sufficient accuracy considering the polarization responses of the individual active and passive steel inside concrete. The electrochemical polarization response of the macrocell anode and macrocell cathode also provides an insight into the micro and macrocell responses at macro-cell steady state. The analysis presented here is however based on simplifying assumptions. While it provides an insight into the macrocell mechanism, more realistic analysis should consider the following:

1. Galvanic activity within the anode – It was assumed that the entire segment located at the crack functions as the macrocell anode. This could only be verified using visual evidence. Direct determination of this would require the use of very small segments at the crack, which is experimentally very challenging. There is a

possibility of a non-uniform distribution of potential along the length of this central segment, which can potentially result in galvanic current flow between parts of the same segment. Under this condition, a macrocell can form along the length of the segment and the actual size of the anode will be smaller than the entire length of the segment. The possibility of a macrocell along the length of this segment needs to be explored.

2. The potential difference along the cathode – It was assumed that the potential along the entire length of cathode after the formation of the macrocell is uniform. The variation in potential between the different segments of the cathode was ignored in the analysis. Realistically, in a continuous steel bar, one can expect a continuous variation in the potential with distance from the crack.

3. Average Tafel behavior for the cathode – The electrochemical polarization response of all the segments of the cathode was assumed to be identical. Variations in the local steel behavior can potentially influence the local current distribution.

At macrocell steady state, there is a constant potential difference between the anode and the cathode, which drives the macrocell current. The actual steady state potential difference would be influenced by two factors: (a) the area of anode to the area of cathode, and (b) the concrete resistivity and the effective resistivity of the conductive path between the two electrodes. The importance of the areas of the anode and cathode in a macrocell

system was first pointed out by Arya (1995). In this analysis the lengths of the macrocell anode and cathode were predetermined by the experimental arrangement. The final equilibrium of the macrocell was determined using the condition that the total macrocell current is the through the macrocell anode is equal to the total macrocell current through the macrocell cathode. Since the Evans diagram is plotted in terms of current densities, the actual areas of the anode and cathode are very significant in determining the final equilibrium of the system. However, if we consider a macrocell system with combined micro and macrocell corrosion reactions, for a given ratio of area of macrocell anode to the area of macrocell cathode, it is obvious from the Evans diagram that as the macrocell current density at the anode increases the microcell current density will decrease. Thus one can conclude that for a given macrocell system, as the macrocell activity increases, the rate of microcell will decrease.

The resistivity of concrete is another factor would have a direct influence on the macrocell behavior. The variation of the effective resistivity of the concrete medium between the anode and different locations of the cathode could potentially influence the current distribution along the length of the steel bar. A proper evaluation of the influence of these factors requires a model for the system which considers the effective medium resistivity. This is presented in next chapter. An effective circuit model which allows for evaluating the influence of parameters such as the effective resistance of the conductive path between the anode and cathode on the macrocell response is presented.

4.7 CONCLUSIONS

The results of an experimental program investigating the macrocell formation in a steel bar embedded in cracked concrete are presented in this chapter. Based on the results obtained, the following conclusions can be drawn:

1. The corrosion of steel in cracked concrete is spatially inhomogeneous. The steel in the vicinity of the crack undergoes active corrosion, while the steel away from the crack is in a passive state. A macrocell corrosion system is setup along the length of the steel bar. Both macrocell corrosion and microcell corrosion mechanisms exist simultaneous in macrocell corrosion system.

2. In the macrocell system, there is a steady potential difference between different locations of the steel bar relative to the crack. There is a macrocell current distribution along the length of the steel bar relative to the crack.

3. In the macrocell system, the potential of the steel located close to the crack is elevated above the value for steel undergoing microcell corrosion. The potential of steel away from the crack is depressed below the potential of passive steel in concrete.

4. The polarization responses of passive steel in concrete and of steel undergoing microcell corrosion can be combined to predict the final state of the macrocell corrosion system.

5. In the macrocell corrosion system established along the length of the steel bar in cracked concrete, the macrocell corrosion mechanism is the dominant component contributing significantly to local metal loss at the crack. Macrocell corrosion rate can be 30 times of the microcell corrosion rate.

6. In macrocell corrosion system, for a given ratio of area of the anode to the area of cathode, there is a decrease in the microcell current density at the anode with an increase in the macrocell current density.

CHAPTER 5

MODEL OF CORROSION IN CRACKED CONCRETE

5.1 INTRODUCTION AND BACKGROUND

The experimental results in chapter 4 indicate that the corrosion mechanism of steel in cracked concrete is much different from the one in uncracked concrete. When a crack intersects a steel bar both microcell and macrocell mechanisms of corrosion contribute to local metal loss at the crack. An investigation of the two mechanisms considering the Tafel responses of active and passive steel using an Evans diagram indicated that when the rate of macrocell current increases there is a decrease in the contribution from the microcell mechanism to the rate of oxidation of iron (contributing to metal loss) at the crack. Under conditions where the concrete was kept in a moist state, the rate of metal loss from the macrocell mechanism was significantly higher than the metal loss due to the local microcell at the crack. The representation using the Evans diagram was however based on simplistic assumptions and only leads to a qualitative understanding of the relationship between the underlying electrochemical processes resulting in metal loss for a steel bar embedded in cracked concrete. The spatial variations in current and potential along the length of steel bar cannot be predicted using this approach. The actual distribution of macrocell current in the system depends upon the resistance of the

concrete medium. A model with a realistic representation of the effective medium resistance of the current flow path is required to predict the current distribution in the steel bar resulting from the combined influence of both the microcell and macrocell. An equivalent circuit model for predicting the current and potential distributions in a steel bar when the continuity of concrete medium is disrupted by a crack along the length of the bar is presented in this chapter. The current distribution obtained from the proposed model is verified for accuracy using the experimental results from Chapter 4.

The formation of crack produces a discontinuity in the material medium which introduces a barrier for ionic conduction and diffusion of ions across the width of crack. Also, the diffusion rates of ions are different through the concrete cover and through the crack. In cracked concrete, the chloride ions pass through the crack and depassivate the steel in the crack zone while the chloride ions and oxygen are transported by a much slower diffusion mechanism in the uncracked zone. Thus, a crack in concrete introduces a spatial variation in the concentrations of oxygen and chloride ions along the length of steel bar. This results in a spatial inhomogeneity in the state of steel along the length of the steel bar. Steel in the vicinity of the crack undergoes active corrosion while steel away from the crack remain in a passive state. The potential of steel in an active state is lower than that of the passive steel. Therefore, a macrocell involving galvanic charge transfer between active and passive areas is established. A simplified representation of macrocell which involves one anode and one cathode and the galvanic charge transfer mechanism is

shown in Figure 5-1. The essential features of a macrocell in a steel bar placed in cracked concrete, which are required for arriving at a suitable circuit model for the system, are reviewed in the next few paragraphs.

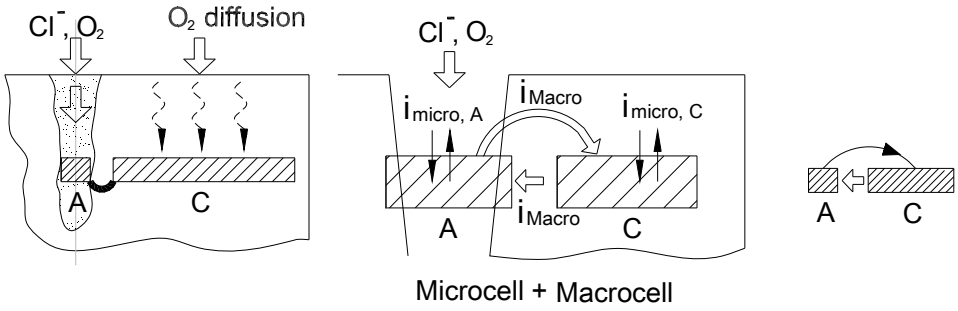

Figure 5-1: Simple representation of macrocell corrosion mechanism

5.2 DRIVING FORCE OF MACROCELL

To understand the driving force for corrosion of steel embedded in cracked concrete, it is essential to understand the corrosion of steel in the local environment located at and away from the crack. This is attempted by considering a segmental steel bar where the steel at the crack has been electrically disconnected from the steel segment embedded in concrete. The local environments at the two steel segments are different; steel in crack is exposed to oxygen and chloride while the steel embedded in concrete has a limited supply of oxygen because of low diffusivity of concrete. Different electrochemical reactions can hence be expected at the two locations. Also, the rate of electrochemical reaction resulting from ion/electron charge transfer across the metal surface will be different at the two locations. This is represented schematically in Figure 5-2 using two

different current densities across the steel-concrete interface located at and away from the crack, $i_{micro,A}$ and $i_{micro,C}$, respectively. This fact was previously verified experimentally and the exchange current densities of the steel located at and away from the crack in the open mode were shown to be different (Figures 4-8 and Table 4-2).

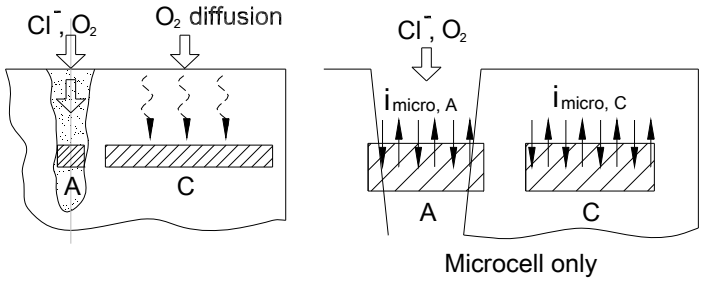

Figure 5-2: Local reactions in separated steel bars

The open circuit potential at the active steel is lower than the potential of passive steel. This potential difference is the driving force for macrocell corrosion (galvanic) current. Once the active and the passive steel are connected, a macrocell is formed and the system will move to a new equilibrium state.

The electrochemical response obtained by combining an active corroding area of steel with a passive one is shown using Evans diagram in Figure 5-3. In this diagram, the rest potentials of the active and passive steel areas before connection are designated as $E_{micro,a}$ and $E_{micro,c}$ respectively. Upon connecting the active and passive steel areas, the following happens:

- Macrocell current flow is established between the active and passive areas. In the resulting cell, the anodically polarized active steel area acts as the macrocell anode.

- The potential of active steel which form the macrocell anode is driven from $E_{micro,A}$ to a more positive value $E_{macro,A}$.
- The potential of passive steel which forms the macrocell cathode changes from $E_{micro,C}$ to a more negative value $E_{macro,C}$.
- The polarization of the active and passive steels will reach equilibrium when the total current through the macrocell anode and macrocell cathode are equal. Thus at equilibrium, $I_{macro,a} = I_{macro,c} = I_{macro}$. Where $I_{macro,c}$ and $I_{macro,a}$ are the macrocell currents through the macrocell cathode and macrocell anode, respectively. I_{macro} refers to the total macrocell current in the system.
- The potential difference between macrocell anode and macrocell cathode, ΔE_r, is due to the resistance of the medium, thus we can obtain the effective resistance due to the medium, R_e as: $R_e = \frac{\Delta E_r}{I_{macro}}$.
- The macrocell current between macrocell anode and macrocell cathode, I_{macro}, is balanced as follows:

$$I_{macro} = I_{macro,a} = i_{macro,A} * Area_{anode} \quad (5.1a)$$

$$I_{macro} = I_{macro,c} = i_{macro,C} * Area_{cathode} \quad (5.1b)$$

where $i_{macro,A}$ and $i_{macro,C}$ are the macrocell current densities, respectively and $Area_{anode}$ and $Area_{cathode}$ are the surface areas of the anode and the cathode, respectively. At equilibrium, the potential difference between the macrocell-anode and the

macrocell-cathode, ΔE_r, therefore provides the driving force for the macrocell, thus functioning like a battery.

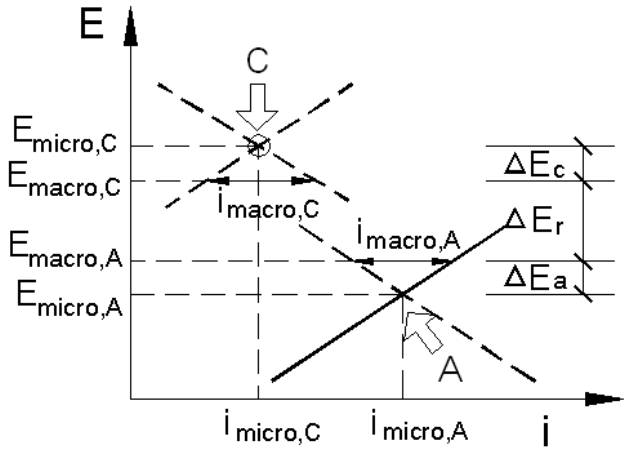

Figure 5-3: Evans diagram of connected anode and cathode

While the Evans diagram representation provides a qualitative understanding of the contribution of the different processes involved in the macrocell, it cannot be used for making quantitative predictions. The macrocell steady state can be predicted using the polarization responses of the active and passive steel if the macrocell current in the system is known. It cannot however, be used to obtain the final equilibrium potentials and macrocell current. The macrocell current in the system would depend upon the effective resistance of the concrete medium. The values of the macrocell current and its distribution along the length of the steel bar would depend upon the effective medium resistance in addition to the potential difference between the anode and the cathode. Therefore, approaches for predicting the equilibrium in a macrocell would require input

of resistance of the medium.

5.3 EQUIVALENT CIRCUIT MODEL OF MACROCELL

Circuit based models which allow for predicting the spatial variation of current and potential along the length of the steel bar have previously been proposed. In this study, it is proposed to use a modified form of the equivalent circuit representation (shown in Figure 5-4) developed by Raupach (1996) to simulate the response of macrocell system. In this representation, the potential difference, ΔE, between the macrocell-anode and macrocell-cathode which provides the driving force for the macrocell is modeled as a battery. Z_a and Z_c represent the equivalent impedances of macrocell-anode and macrocell-cathode, respectively. R_e represents the effective concrete resistance between the macrocell-anode and the macrocell-cathode.

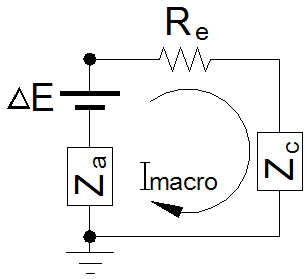

Figure 5-4: Simplified equivalent circuit of macrocell

The main assumptions in the model proposed by Raupach are:

(1) The reaction rate at the surface of the macrocell-anode and the current density at the

macrocell-cathode and macrocell-anode due to galvanic current flow associated with the macrocell are uniform.

(2) The values of Z_c and Z_a are constant, which will not change with a change in the macrocell current.

5.3.1 Equivalent Circuit Representation for Impedance of Steel-Concrete Interface

From the results presented in Chapter 3, the impedance of the steel-concrete interface can be represented using an equivalent circuit a series combination of a resistance (R_e) with a parallel combination of a resistance (R_p) and CPE element (shown in Figure 5-5a). When subjected to a linear potential sweep, the contribution of the CPE to the transient current flow decreased with time and eventually became insignificant. Following the initial transient, where the contribution of the CPE was significant, a linear relationship was obtained between the applied potential and the current indicating that the steady state, long-term response of the steel-concrete interface is purely resistive as shown in Figure 5-5(b).

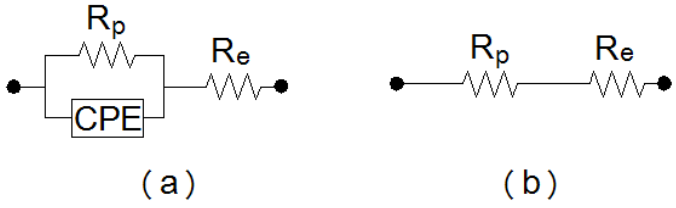

Figure 5-5: Equivalent circuit representation for the steel-concrete interface.

Considering the steady-state macro-cell response in the cracked beam, the impedance of the steel-concrete interface in the equivalent circuit model for the macrocell can be replaced by a resistance as shown in Figure 5-6. The impedance of the steel bar at macrocell anode and cathode are represented by the polarization resistances of steel in the active and passive states, respectively.

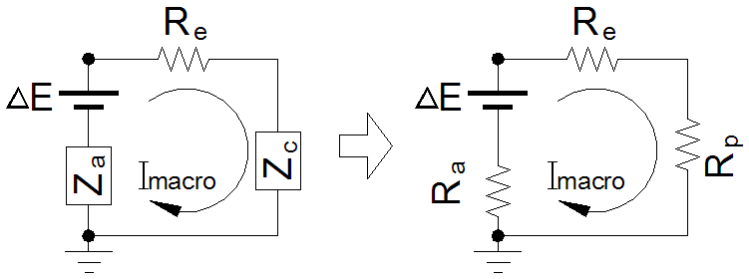

Figure 5-6: Simplified equivalent circuit of macrocell

5.3.2 Proposed Improvements to the Equivalent Circuit Model

The simplified circuit model presented in the previous section provides an acceptable circuit representation of the macrocell. However, additional improvements to the circuit model considering realistic representations of the underlying phenomena are required.

(a) The polarization resistance of the macrocell-anode and macrocell-cathode varies with the current in the system. The effective polarization resistance, R_p^*, at macrocell steady state when a current flows through the steel bar is different from the R_p

measured by LPR techniques when there is no galvanic current flow through the steel-concrete interface.

(b) The current and potential distributions across the length of the steel bar may not be constant and may vary with distance from the crack. This requires a circuit representation, which allows for studying spatial variation in the electric current and potential distributions. For current flow through concrete, the effective medium resistance is not a constant and cannot be represented by a single resistance. The effective medium resistance between the macrocell anode and cathode varies with distance and has to be predicted considering the geometry of the current flow path based on resistivity of concrete.

The proposed improvements are discussed further in the subsequent sections.

Variable Resistance of the Steel-Concrete Interface

The polarization resistance in the macrocell circuit is not a constant which provides a constant relationship between the applied voltage and current. Instead, considering the electrochemical polarization response of an electrode (both corroding and non-corroding), it can be shown that the relationship between the applied potential and current is not linear at a large potential shifts. The exact potential-current relationship for the steel-concrete interface is illustrated considering the electrochemical behavior of the underlying reactions at a corroding electrode. The potential-current relationships of the

anodic and the cathodic reactions are shown using an Evans diagram in Figure 5-7. In the diagram, $E_{micro,A}$ and $i_{micro,A}$ represent the rest potential and the current density of the electrode before the formation of the macrocell, respectively.

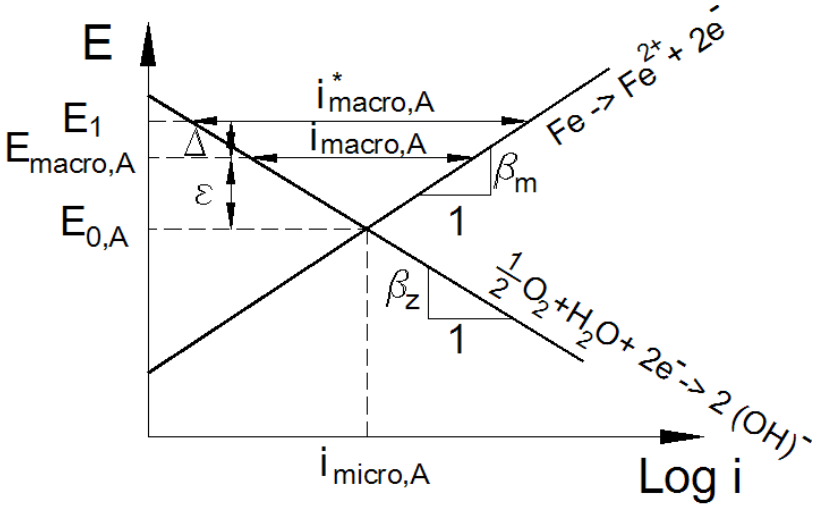

Figure 5-7: Variable polarization resistance: behavior of macrocell anode.

At macrocell equilibrium, the potential of the active steel is raised to $E_{macro,A}$. The macrocell current density through the macrocell-anode (active area) is given by the Butler-Volmer equation

$$i_{macro,A} = i_{micro,A}\left(10^{\left(\frac{\varepsilon}{\beta_m}\right)} - 10^{\left(-\frac{\varepsilon}{\beta_z}\right)}\right) \tag{5.2}$$

where $i_{micro,A}$ is the microcell current density at rest potential, ε is the potential shift from the rest potential to the macrocell equilibrium, β_m and β_z are the Tafel slopes for anodic and cathodic polarization, respectively.

Considering a very small potential perturbation Δ at the macrocell equilibrium, the potential of the active steel is raised to E_1. The new macrocell current density through the macrocell-anode (active area) considering the applied potential perturbation is obtained from the Butler-Volmer equation

$$i^*_{macro,A} = i_{micro,A}\left(10^{\left(\frac{\varepsilon+\Delta}{\beta_m}\right)} - 10^{\left(-\frac{\varepsilon+\Delta}{\beta_Z}\right)}\right) \tag{5.3}$$

A relationship can now be derived between the applied potential perturbation and the change in the current through the electrode. The increment in the current density corresponding to the applied potential perturbation is obtained as

$$\begin{aligned}\Delta i = i^*_{macro,A} - i_{macro,A} &= i_{micro,A}\left(10^{\left(\frac{\varepsilon+\Delta}{\beta_m}\right)} - 10^{\left(-\frac{\varepsilon+\Delta}{\beta_Z}\right)} - 10^{\left(\frac{\varepsilon}{\beta_m}\right)} + 10^{\left(-\frac{\varepsilon}{\beta_Z}\right)}\right) \\ &= i_{micro,A}\left(10^{\left(\frac{\varepsilon}{\beta_m}\right)}\left(10^{\frac{\Delta}{\beta_m}} - 1\right) - 10^{-\frac{\varepsilon}{\beta_Z}}\left(10^{-\frac{\Delta}{\beta_Z}} - 1\right)\right)\end{aligned} \tag{5.4}$$

Since Δ is a very small value, $10^{\Delta} \cong 1+2.3\Delta$, therefore

$$\Delta i = i_{micro,A}\left(10^{\left(\frac{\varepsilon}{\beta_m}\right)}\left(2.3\frac{\Delta}{\beta_m}\right) - 10^{-\frac{\varepsilon}{\beta_Z}}\left(-2.3\frac{\Delta}{\beta_z}\right)\right) = 2.3\Delta i_{micro,A}\left(\frac{10^{\left(\frac{\varepsilon}{\beta_m}\right)}}{\beta_m} + \frac{10^{\left(-\frac{\varepsilon}{\beta_Z}\right)}}{\beta_z}\right) \tag{5.5}$$

The polarization resistance, which relates ΔE and Δi at the macrocell equilibrium, is given as

$$R_p^* = \frac{\Delta E}{\Delta i} = \frac{1}{2.3 i_{micro,A}\left(\frac{10^{\left(\frac{\varepsilon}{\beta_m}\right)}}{\beta_m} + \frac{10^{\left(-\frac{\varepsilon}{\beta_z}\right)}}{\beta_z}\right)} \tag{5.6}$$

The polarization resistance at the rest potential can be obtained from Equation 5.6 when ε=0 and is similar in form to the expression derived by Stern and Geary (1957) for a corroding electrode

$$R_p = \frac{\Delta E}{\Delta i} = \frac{1}{2.3 i_{micro,A}\left(\frac{1}{\beta_m} + \frac{1}{\beta_z}\right)} \tag{5.7}$$

Therefore, the ratio of the polarization resistance of the steel-concrete interface obtained at a large potential shift away from the rest potential to the corresponding value at the rest potential is given as

$$\frac{R_p^*}{R_p} = \frac{\frac{1}{\beta_m} + \frac{1}{\beta_z}}{\frac{10^{\left(\frac{\varepsilon}{\beta_m}\right)}}{\beta_m} + \frac{10^{\left(-\frac{\varepsilon}{\beta_z}\right)}}{\beta_z}} \tag{5.8}$$

Using a similar procedure, the relationship for R_p* at the cathode, when it is subjected to a large potential shift away from its rest potential can be calculated and is given as

$$R_p^* = \frac{\Delta E}{\Delta i} = \frac{1}{2.3 i_{micro,A}\left(\frac{10^{\left(\frac{\varepsilon}{\beta_z^*}\right)}}{\beta_z^*} + \frac{10^{\left(-\frac{\varepsilon}{\beta_z^*}\right)}}{\beta_z^*}\right)} = \frac{\beta_z^*}{2.3 i_{micro,A}\left(10^{\left(\frac{\varepsilon}{\beta_z^*}\right)} + 10^{\left(-\frac{\varepsilon}{\beta_z^*}\right)}\right)} \quad (5.9)$$

The polarization resistance at the rest potential can be obtained from Equation 5.9 when ε=0 and is similar in form to the expression derived by Stern and Geary (1957) for a non-corroding electrode

$$R_p = \frac{\Delta E}{\Delta i} = \frac{\beta_z^*}{(2.3)(2) i_{micro,A}} \quad (5.10)$$

The ratio of the polarization resistance of the passive steel-concrete interface obtained at a large potential shift away from the rest potential to the corresponding value at the rest potential is given as

$$\frac{R_p^*}{R_p} = \frac{2}{10^{\left(\frac{\varepsilon}{\beta_z^*}\right)} + 10^{\left(-\frac{\varepsilon}{\beta_z^*}\right)}} \quad (5.11)$$

The R_p^* of active and passive steel subjected to macrocell current which results in a potential shift away from its rest potential are plotted in Figure 5-8. The values of the Tafel constants obtained previously in Chapter 4 have been used in generating the graphs and are given as: Anode: β_m = 435 mV, β_z = 99 mV; and Cathode β_z^* = 205 mV. It can be seen that the R_p^* of active steel located at the macro-cell anode could be 2.5 times larger than the value of R_p at its rest potential. The R_p^* of cathode on the other hand, decreases for a potential shift away from the passive state.

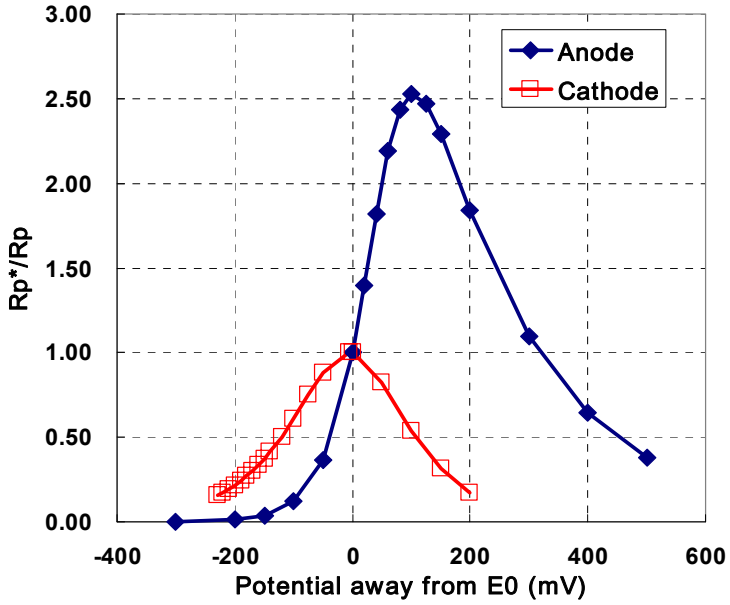

Figure 5-8: Ratio of R_p^* and R_p

5.3.3 Spatial Variation of Macrocell Cathodic Potential and Current Density

From an experimental investigation involving macrocell corrosion of steel in a model macrocell, Elsener (2002) showed that there is a spatial distribution in the measured potential and current between the macrocell anode and cathode (as shown in Figure 5-9). The spatial variation was found to vary with the resistance of the medium.

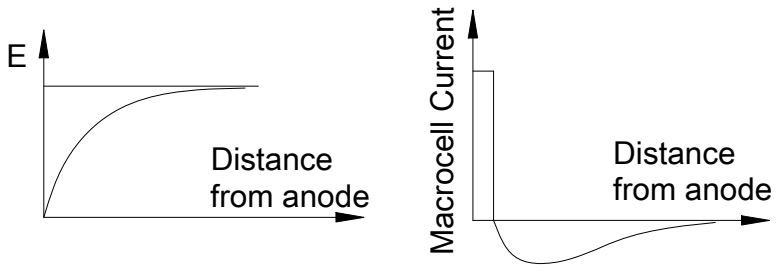

Figure 5-9: Potential and current distribution of macrocell.

To provide a realistic representation of the actual system, the simple model presented by Raupach can be extended to consider the variation in the effective medium resistance from the anode to different points on the steel bar as shown in Figure 5-10. This is analogous to the distributed element circuit model which has been used previously by researchers to study the polarization of bar steel in concrete (Feliu 1989). In this representation, R_{ei} and R_{ci} represent the effective medium resistancees along paths which are parallel and perpendicular to the steel bar, respectively.

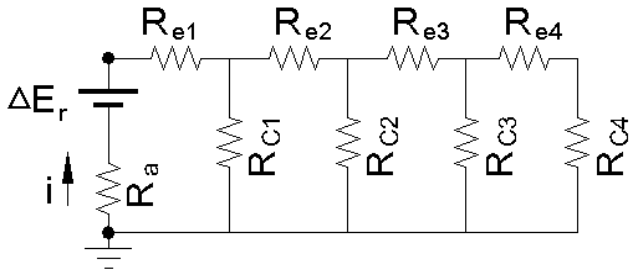

Figure 5-10: Equivalent representation for modeling corrosion of steel bar in cracked concrete.

5.4 EQUIVALENT DISTRIBUTED ELEMENT CIRCUIT MODEL FOR CRACKED BEAM

5.4.1. Symmetry of Model

An equivalent distributed element circuit model is developed for the cracked beam specimen used in Chapter 4. The specimen used for studying corrosion in cracked

concrete comprised of a steel bar placed symmetrically with respect to the crack. A circuit model suitable for representing the resulting macrocell therefore comprises a symmetric placement of resistors as shown in Figure 5-11. An equivalent one-sided distributed element circuit can however be obtained from this symmetric circuit as shown in Figure 5-11. The $R_{e,A}$ in the symmetric circuit can be replaced by two resistances, $2R_{e,A}$, in parallel, which provide the same equivalent resistance. Similarly, $R_{p,A}$ can be replaced by two parallel resistances with values $2R_{p,A}$. The battery in the circuit can also be equivalently replaced by two batteries in parallel with the same voltage E. The current flow through the $R_{e,A}$, $R_{p,A}$ and E will be evenly split into two part as shown in Figure 5-11. Considering symmetry, no current will flow between the two portions. Therefore, the circuit can be simplified as an equivalent one-side circuit as shown in Figure 5-11. The macrocell current predicted by the one-side model is half of the total macrocell current through the entire macrocell corrosion system.

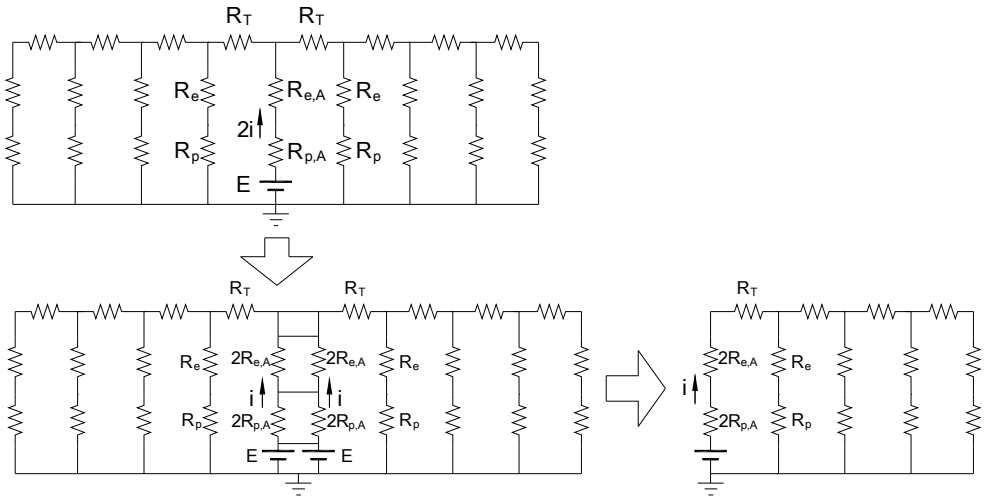

Figure 5-11: Simplified by symmetry: Equivalent One-side Circuit

5.4.2. Concrete Medium Resistivity

To consider the current distribution through the concrete cover depth it is proposed to model the concrete surrounding the steel as being composed of two cover layers, an inner layer and the surface layer. It is also proposed to discretize the concrete medium along the length of the steel bar into smaller segments. The equivalent circuit representation considering the two layer representation of concrete is shown in Figure 5-12. In this representation, each R^*_{pi} represents the resistance of a fixed length of the steel-concrete interface. The values of R^*_{pi} depend upon the applied potential and are obtained using Equations 5.6 and 5.9. In the circuit, $R_{Ti,1}$ and $R_{Ti,2}$ represent the resistances of fixed lengths of concrete in the longitudinal direction for the inner and outer layers concrete, respectively. $R_{ri,1}$ and $R_{ri,2}$ are the resistances of the inner and outer layers, respectively in the radial direction.

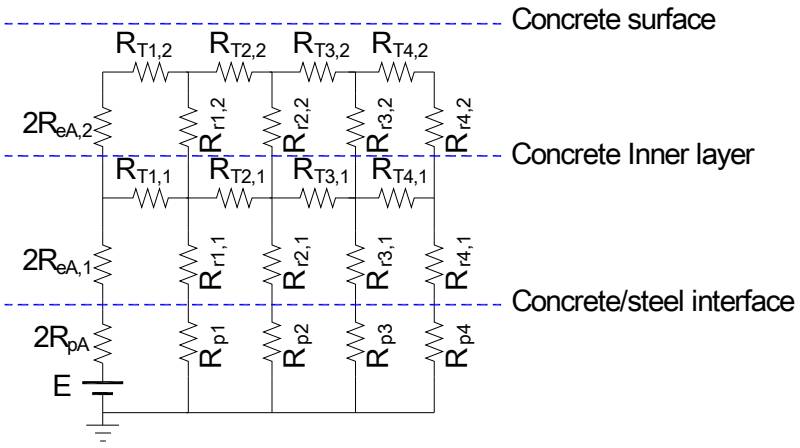

Figure 5-12: Equivalent representation considering two layer concrete resistances.

The effective resistances corresponding to each layer for current flow in a particular direction can be obtained from the geometry of the each layer considering the cross-sectional area perpendicular to current path in a specific direction. The effective concrete resistances, $R_{a,1}$, $R_{a,2}$, $R_{T1,1}$, $R_{T1,2}$, $R_{r1,1}$, $R_{r1,2}$ etc, can be determined from the concrete resistivity ρ and geometry using equation

$$R = \frac{\rho L}{A} \tag{5.12}$$

where ρ is concrete resistivity, L is length of current flow path and A is cross sectional area perpendicular to flow of current.

The resistivity of concrete is a material property which depends upon its moisture state. Since the resistance of the concrete medium has a direct influence on the current distribution, an accurate measurement of resistivity of concrete is essential for a proper estimation of the resistances used in the circuit model.

Concrete resistivity was measured using the procedure developed by Gowers and Millard (1999). Four equally spaced electrodes were placed on the concrete surface in the Wenner configuration as shown in Figure 5-13. A small AC current, *I*, was passed between the two outer electrodes and the potential difference, *V*, between the inner electrodes was measured. The resistivity, ρ, of concrete was obtained as

$$\rho = 2\pi a \frac{V}{I} \tag{5.13}$$

where a is the electrodes spacing

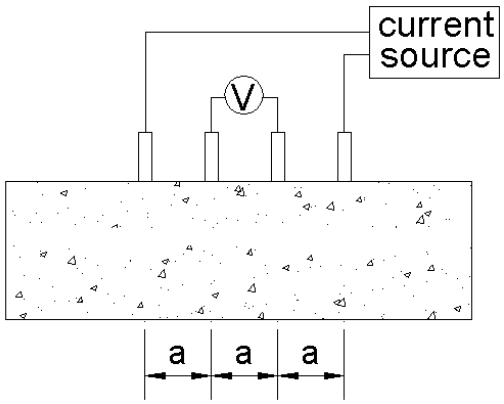

Figure 5-13: Wenner technique for measuring resistivity.

Four stainless steel electrodes (electrode area = 1 in^2) were placed on the concrete surface at a spacing equal to 2 in. Individual sponge sheets soaked in salt water were placed between the electrodes and the concrete surface to provide electrical contact. Alternating current with frequency equal to 30Hz was applied using a function generator. The potential difference between inner electrodes were measured using a high-precision, hand-held multi-meter. Concrete resistivity was measured at four locations as shown in Figure 5-14. The concrete resistivity at the four locations obtained using AC current signals with different shapes and amplitudes are listed in Table 5-1. It can be seen that the resistivity of concrete measured at the four locations is comparable. This suggests that the concrete in the specimen is relatively homogeneous. It is also interesting to note that the resistivity measured across the crack is of the same magnitude as the resistivity obtained from bulk concrete. The average resistivity obtained from multiple readings and from multiple locations is equal to 26 kΩcm, which compares favorably with the value of 10 kΩcm reported by Sagues and Kranc (2001) for moist concrete.

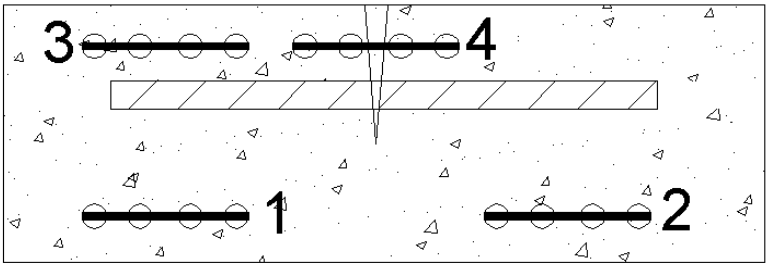

Figure 5-14: Four locations of Wenner electrodes to measure to concrete resistivity.

Table 5-1: Concrete resistivity measurement of specimen

Locations	Wave	Freq & Voltage	V (mV)	I (mA)	R (Ω)	ρ (Ωcm)
1	Sq	30, 0.5 V	43	0.625	67	20 k
		30, 1 V	92	1.27	72	21 k
	Sine	30, 0.5 V	34.7	0.471	73.6	22 k
2	Sine	30, 0.5 V	37.7	0.479	79	24 k
	Sq	30, 0.5 V	58	0.710	81	24 k
		30, 1 V	120	1.425	84	25 k
3	Sq	30, 0.5 V	105	0.868	130	39 k
		30, 1 V	54.5	0.458	119	36 k
4	Sq	30, 0.5 V	30	0.38	78	23 k
		30, 1 V	70	0.784	89	27 k
Average						26 k

5.4.3 Parameters for the Equivalent Circuit Model

The modified distributed element circuit model presented in the previous section to represent the macrocell steady state requires an input of several parameters.

Driving Potential ΔE

As shown in chapter 4, the potential difference between anode and cathode is about 300 mV. It is consistent with the 300 mV potential difference between anode and cathode reported by Raupach (Raupach, 1996).

Equivalent Medium Resistance

The concrete around the steel bar is divided into the inner and outer regions as shown in Figure 5-15(a) and (b). The inner region extends outwards from the outer surface of the steel bar. The outer region extends from outer surface of the inner region to the outer surface of the specimen. The effective medium resistances in the longitudinal direction segments as shown in Figure 5-15(b) (c), can be obtained as

$$R_{t1} = \frac{\rho L}{A_1} \tag{5.14a}$$

$$R_{t2} = \frac{\rho L}{A_2} \tag{5.14b}$$

where L is the distance between center of segments and A_1 and A_2 are the cross-sectional areas of inner region and outer region, respectively.

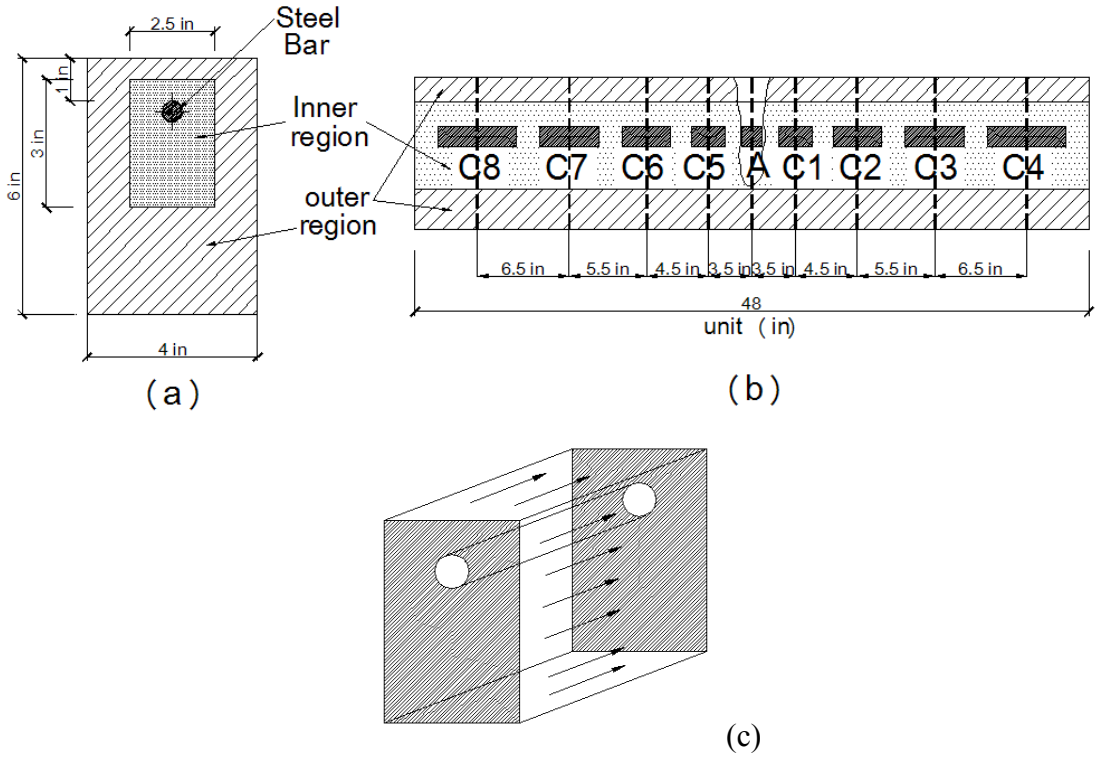

Figure 5-15: the scheme of calculating longitude effective concrete resistance.

The center to center distance between the different segments and the corresponding values of R_t for the inner and outer layers are shown in Table 5-2.

Table 5-2: Value of R_t and distance between centers of segments.

	A to C1 A to C5	C1 to C2 C5 to C6	C2 to C3 C6 to C7	C3 to C4 C7 to C8
Distance between center of segments (cm)	8.89	11.43	13.97	16.51
R_{t2} (Ω)	2171	2792	3412	4032
R_{t1} (Ω)	4777	6142	7507	8871

The effective medium resistance of the inner region in the radial direction extending

from the steel surface to the outer layer is represented by R_{r1}. The current distribution in the radial direction in the inner layer is shown schematically in Figure 5-16. Considering the rectangular geometry, the current distribution in the radial direction does not provide a uniform current density across different locations of the concrete surface perpendicular to the current path. An average value of all transfer paths was calculated as the effective R_{r1}. The cross-section of the inner region was divided into four regions marked as 1, 2, 3 and 4 as shown in Figure 5-16. The current distribution was assumed to be uniform within each region. For each region, the resistance for the current flow through a quarter of steel perimeter to the outer surface of inner layer, was calculated as

$$R_1 = \frac{\rho L}{A} \tag{5.15}$$

where, L is the distance between the outer steel surface to the outer surface of the inner region. The cross sectional area, A was calculated as the average of cross-sectional areas at the two boundaries of the region as shown in Figure 5-16. The effective R_{r1} for the inner region was calculated as the equivalent resistance from a parallel combination of the resistances of the four regions. A similar approach was applied to obtain the effective medium resistance of concrete in the outer layer R_{r2}. The values of R_{r1} and R_{r2} for concrete medium associated with the different segments of steel bar are given in Table 5-3.

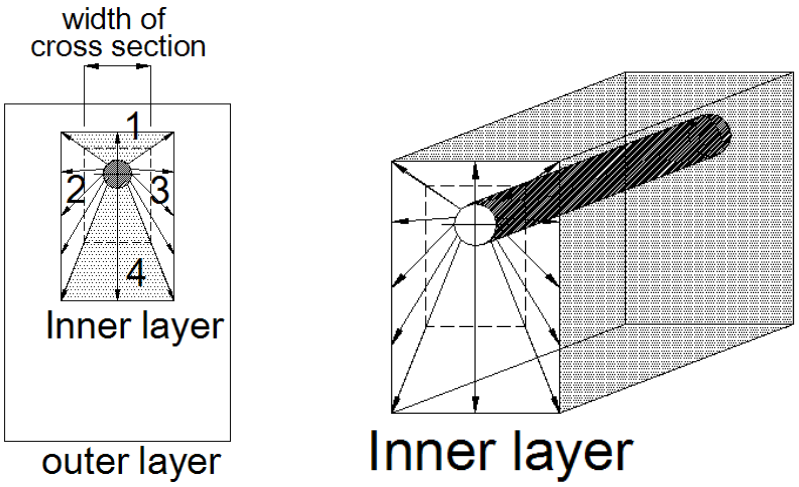

Figure 5-16: the scheme of calculating radial effective concrete resistance.

Table 5-3: Value of radial effective concrete resistance R_r

	A	**C1**	**C2**	**C3**	**C4**
$R_{r,2}$ (Ω)	814	272	204	163	136
$R_{r,1}$ (Ω)	1630	543	407	326	272

Polarization Resistance R_p

The initial values of the resistors associated with the steel-concrete interface can be calculated using the R_P determined from the LPR measurement in the open mode. The R_p values of anode and cathode segments in the open mode are equal to 2.9e4 Ωcm^2 and 2.6e6 Ωcm^2, respectively. Considering the areas of segments A, C1, C2, C3 and C4 are 20 cm^2, 30 cm^2, 40 cm^2, 50 cm^2 and 60 cm^2, respectively, the effective resistances at the steel-concrete interface at the macrocell anode and the different segments of cathode, can be obtained by multiplying the R_p in the open mode by the area of the segment. The initial values of $R_{p,a}$, R_{p1}, R_{p2}, R_{p3} and R_{p4} are equal to 1450 Ω, 86666 Ω, 65000 Ω,

52000 Ω and 43333 Ω, respectively.

5.4.4 Simulation Procedure

In the equivalent distributed element circuit circuit model, the values of the resistors for the steel-concrete interfaces at the anode and the different locations of the cathode depend upon the potential difference across the resistor. The final value of potential difference across the resistor, however, depends upon the value of the resistance. Thus, an iterative procedure given below was used to obtain the final values of potential and resistances in the circuit.

1. The values of R_p at the rest potential (initial potential in the open mode) were used as the initial R_p^*. The model, as shown in Figure 5-17, was used to simulate the system in open mode. When the switch is open, the initial potential crossing the $R_{p,c}$ are 0 and The initial potential crossing the anode, include $R_{p,a}$ and the battery, is -300 mV.

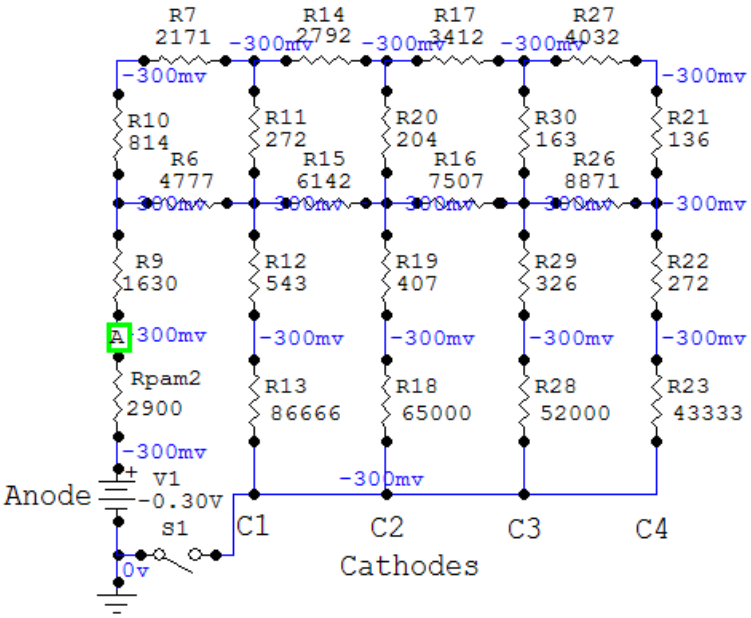

Figure 5-17: Equivalent circuit model of macrocell corrosion system in open mode

2. The switch is closed to simulate the system in closed mode. The values R_p are kept constant, and the potentials across each R_p is obtained from an analysis of the circuit, as shown in Figure 5-18.

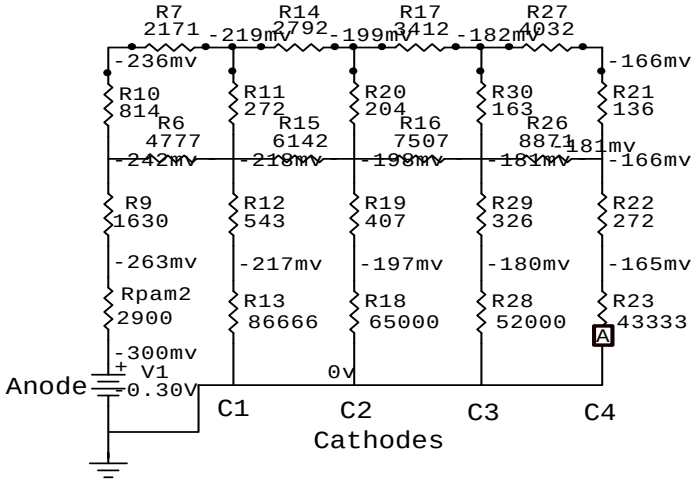

Figure 5-18: Equivalent circuit model of macrocell corrosion system in close mode using initial R_p

3. The potential shifts away from the initial potentials across R_p were recorded. The values of R_p^* were revised according to the potential shift using equations 5.6 and 5.9. The model is revised using the new values of R_p^* for R_p of anode and cathodes.

4. Repeat step 2 to step 4 until convergence in R_p^* is achieved.

5.5 MODEL PREDICTION

The circuit model using initial value of R_p and the analysis result are shown in Figure 5-19. The potential of each node obtained from the model were shown in Figure 5-19. The potential shift of anode from the -300 mV initial potential in open mode was 37 mV; the potential shift of C1, C2, C3, and C4 were -217 mV, -197 mV, -180 mV and -165 mV, respectively. The corresponding revised R_p^* can be obtained using equation 5.8 and 5.11. The revising procedures were repeated until convergence occurred as shown in previous section.

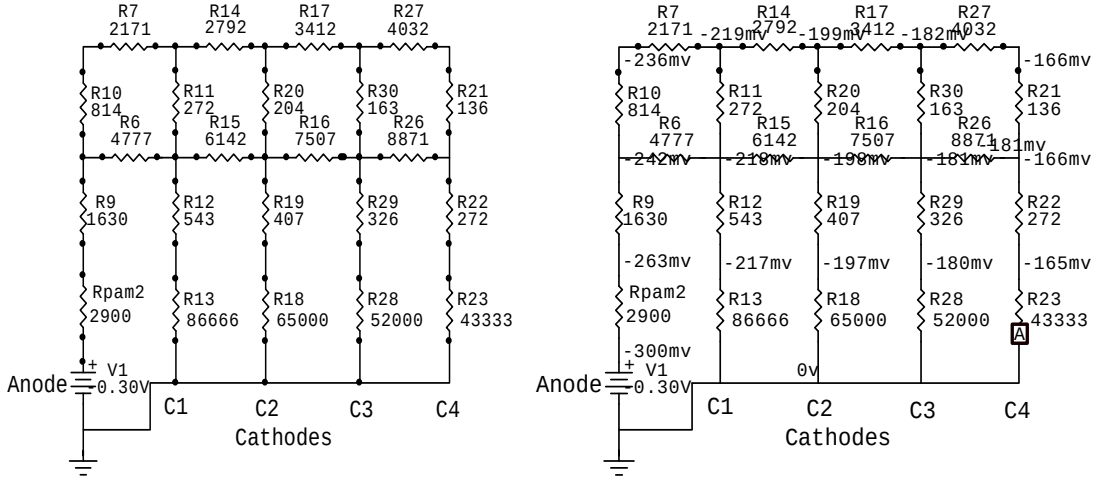

Figure 5-19: Initial model and result

The final model using the converged value of R_p^* is shown in Figure 5-20. When the macrocell cell was established and the macrocell current reached their equilibrium, it can be seen that the R_p^* of the macro-cell anode increased to 2.4 times of the initial value of R_p at its rest potential. The R_p^* of cathodes C1, C2, C3 and C4, on the other hand, decreases to 0.41, 0.5, 0.6 and 0.6 time of their initial value respectively as shown in Table 5-4. The ratio of R_p^*/R_p were increasing along the cathode with distance away from the anode. It is consistence with the decreasing potential shift along the cathode with distance away from the anode as shown in Table 5-4.

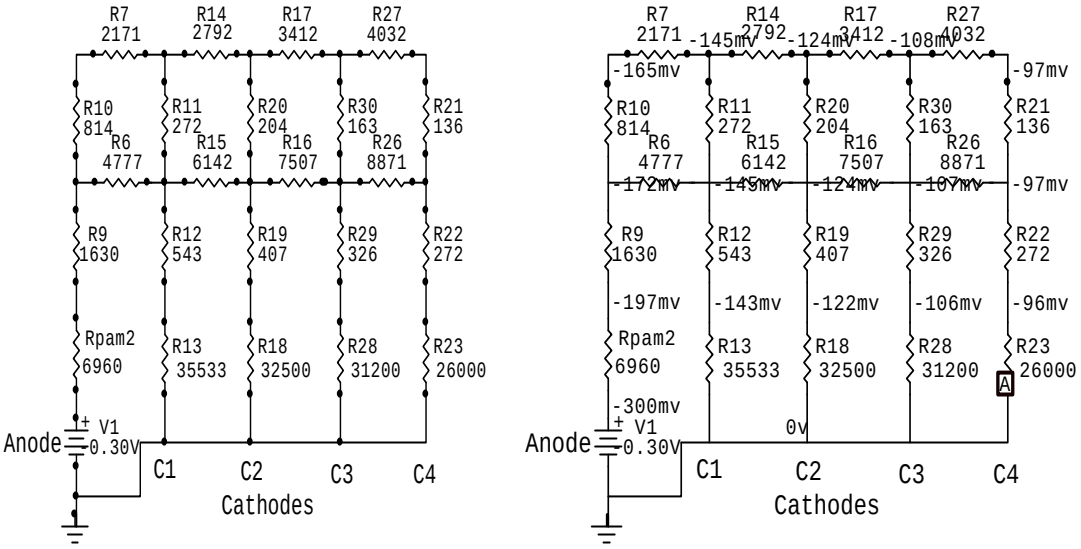

Figure 5-20: Revised model using variable R_p and its result

Table 5-4: the variable R_p^*.

	A	C1	C2	C3	C4
Initial R_p (Ω)	2900	86666	65000	52000	43333
Final R_p^* (Ω)	6960	35533	32500	31200	26000
Ratio R_p^*/R_p	2.4	0.41	0.5	0.6	0.61
Potential shift compare to E_0 (mV)	103	-143	-122	-106	-96

The macrocell current flow between each segment obtained experimentally, are shown in Figure 5-21. The macrocell current distributions obtained from initial and final converged values of R_p are shown in Figure 5-22 and Figure 5-23, respectively. The I_{macro} of anode from each side of cathode obtained from initial model are equal to 12.8 μA; the final converged value of I_{macro} to the anode from cathodes located on each side obtained are equal to 14.9 μA. The predicted value compares favorable with the 20 μA obtained experimentally. It can be seen that the final value using the variable R_p* provide a more accurate prediction of the macrocell current distribution.

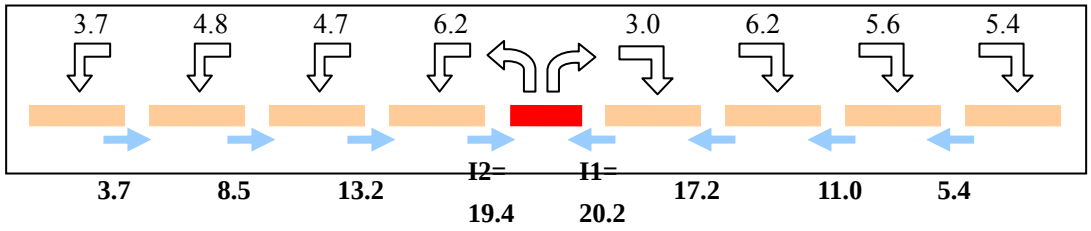

Figure 5-21: Macrocell current: experimental data

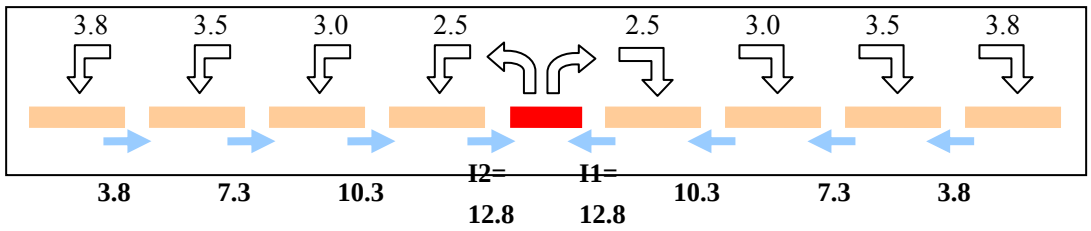

Figure 5-22: Macrocell current: Initial Model prediction

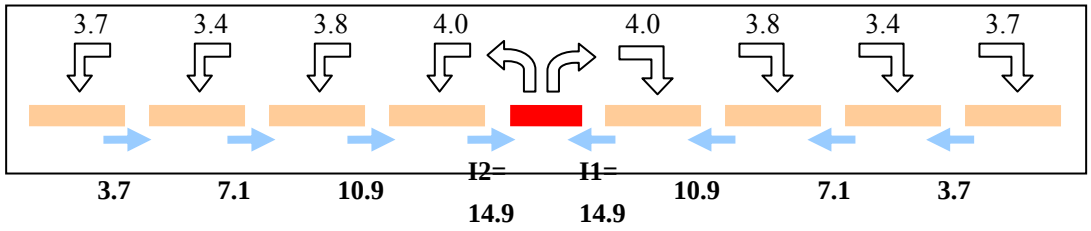

Figure 5-23: Macrocell current: Final Model prediction

The macrocell current density entering each segment across the steel-concrete interface for each segment is shown in Figure 5-24. It can be seen that macro-cell current density at the anode is significantly higher than the corresponding value at different locations of the cathode. The predicted current density compared favorably with the experimental measurement.

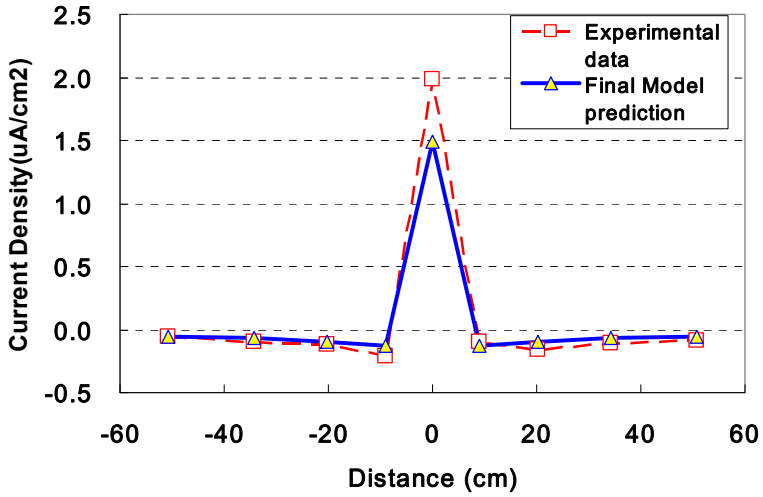

Figure 5-24: Macrocell current density distribution: comparison of experimental data the model prediction.

The possible reason of bias may come from the bias in measurement of R_e, R_p, ΔE

and Tafel constant. For example, the concrete resistivity, a key factor to affect the macrocell magnitude, depends on the concrete moisture content which is a large variable in each measurement. The temperature of lab will also affect the measurements. The sensitivity of those parameters are discussed in the next section.

5.6 PARAMETRIC ANALYSIS

The equivalent distributed element circuit model for the steel bar in cracked concrete provides a convenient way to evaluate the influence of the different parameters on the macrocell current distribution in such a system. The role of parameters which influence the response of the macro-cell can now be identified by varying the magnitude of the control parameter while keeping the magnitudes of all other variables constant. The two key parameters which are known to play a significant role in the macrocell corrosion system are: (a) the resistivity of concrete; and (b) the relative size of anode. A parametric study which investigates of the effect of variation of these parameters on the macrocell is presented in this section.

Concrete resistivity

The effect of concrete resistivity on the macrocell corrosion current density is studied by varying its value while holding the magnitudes of all other variables fixed. Analyses were performed for three different values of resistivity equal to 26, 260 and 2600 kΩcm.

The results of analysis are shown in Figure 5-25. As illustrated in this figure, the macrocell current density at the anode decreases dramatically from 1.5 $\mu A/cm^2$ to 0.45 $\mu A/cm^2$ when the concrete resistivity increases from 26 kΩcm to 260 kΩcm. Further when the concrete resistivity is increased to 2600 kΩcm, the macrocell current density at the anode decreases to an insignificantly small value equal to 0.07 $\mu A/cm^2$.

The effects of concrete resistivity on the macrocell corrosion potential cross the steel/concrete interface are shown in Figure 5-26. As illustrated in this figure, the macrocell corrosion potential of anode goes to more negative from -197 mV to -266 mV to -295 mV when the concrete resistivity increases from 26 kΩcm to 260 kΩcm to 2600 kΩcm. At the macrocell anode, the potential across the steel-concrete interface approaches -300 mV as the resistivity of concrete increases. This suggests that the potential of the macrocell anode approaches a value equal to the potential of active steel undergoing uniform microcell corrosion with an increase in concrete resistivity.

The potential and current distributions in Figures 5-25 and 5-26 indicate that there is a decrease in the spread of the macrocell with an increase in concrete resistivity. As the resistivity of concrete increases, the size of the cathode supporting the anode decreases. The shapes of the potential and current distributions also suggest a very sharp gradient in a very small region close to the macrocell anode, suggesting a more localized behavior when the resistivity of concrete increases. When the concrete resistivity is high enough, the macrocell would become very local and limited to a very tiny region close to crack.

The changes in the current and potential distributions coupled with a decrease in macrocell current density at the anode with an increase in resistivity suggest that the local metal loss at the crack is predominantly due to microcell corrosion mechanism.

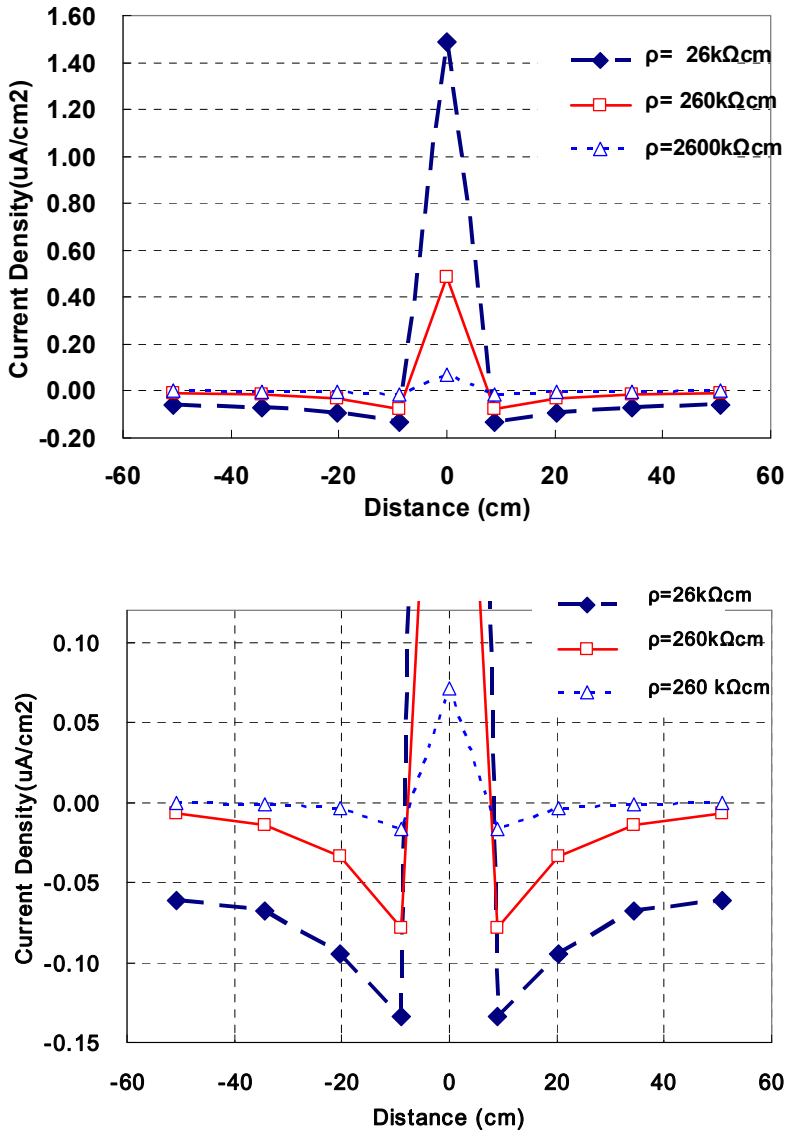

Figure 5-25: the effect of concrete resistivity on macrocell current

These observations can also be explained by Evans diagram presented in Chapter 4, which suggests that the macrocell current density at the anode decreases with an increase

in the microcell current density. When the macrocell current decreases to zero and the macrocell potential return to rest potential, the macrocell corrosion drop to zero and the microcell current increasing to exchange current in the rest potential.

Concrete resistivity is therefore a key factor affecting not only the magnitude of the macrocell corrosion but also the mechanism/existing of macrocell corrosion. In addition, the range/extent of macrocell corrosion is determined by the concrete resistivity.

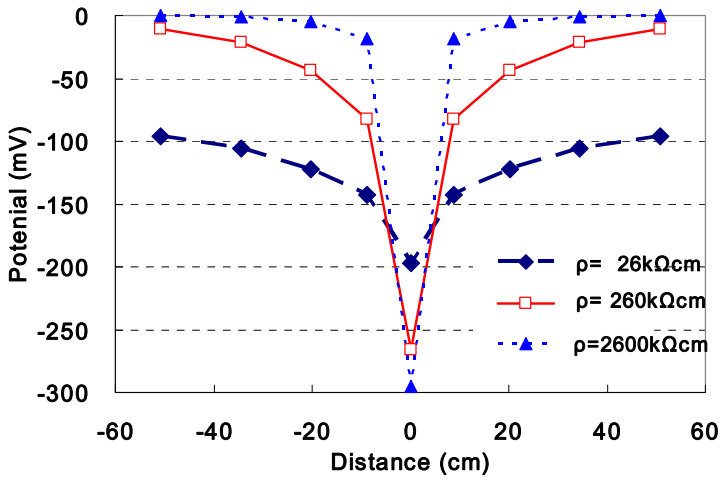

Figure 5-26: the effect of concrete resistivity on macrocell potential at the steel/concrete interface.

Size of Anode (R_{eA}, R_{pA})

The effect of size of anode on the macrocell corrosion current density is studied by varying size of anode from half size to double the size. The results of analysis are shown in Figure 5-27. When the anode size is doubled, the R_{pA} and R_{eA} will be half because the area of anode is doubled. The macrocell current increased from 1.5 $\mu A/cm^2$ to

1.9 μA/cm^2 when anode size is doubled. When the anode size is halved, the R_{pA} and R_{eA} will be doubled because the area of anode is halved. The macrocell current decreased from 1.5 μA/cm^2 to 1.0 μA/cm^2 when anode size is halved. This change is not significant.

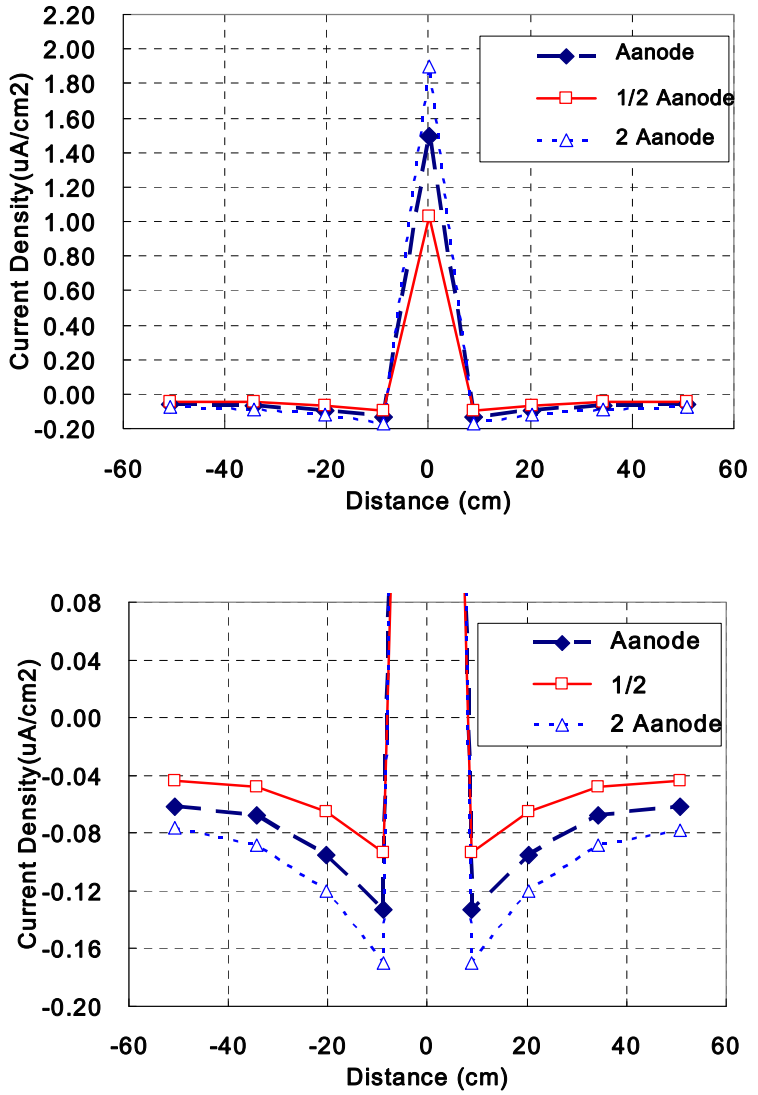

Figure 5-27: the effect of size of anode.

From these result, some conclusions can be draw that:

1. Influence of the size of anode to magnitude of macrocell current is not significant.

2. Influence of the size of anode to the extent of cathodes supporting anode is not significant.

The results can potentially explain why the macrocell current is not dependent on the width of crack as reported previously (Schiessl and Raupach 1997).

5.7 CONCLUSIONS

An equivalent circuit model to simulate the macrocell corrosion of steel in concrete is presented in this chapter. Based on the comparison of experimental data and model prediction, the following conclusion can be drawn:

1. The proposed distributed element circuit model provides favorable prediction of the macrocell corrosion in cracked concrete.
2. The model considering variable R_p, considering the influence of potential shift away from rest potential provides more accurate prediction than the model using initial R_p.
3. Concrete resistivity is a key factor affecting not only the magnitude of the macrocell corrosion but also the mechanism/existing of macrocell corrosion. The magnitude of macrocell corrosion decrease with the increase in the resistivity of the concrete. Therefore, the macrocell mechanism will diminish and return to the microcell mechanism if the concrete resistivity is large enough. In addition, the range/extend of macrocell corrosion is determined by the concrete resistivity.
4. Influence of the size of anode to magnitude of macrocell current is not significant.

Influence of the size of anode to the extent of cathodes supporting anode is not significant. Therefore, the macrocell current are not depends on the width of crack.

CHAPTER 6

POLARIZATION OF MACROCELL

6.1 INTRODUCTION

6.1.1 Background

The experimental results in chapters 3, 4 and 5 indicate that a crack in concrete changes the corrosion pattern along the length of the steel bar when compared to the corrosion of steel in uncracked concrete. Experimental evidence also suggests the possibility of corrosion through the macrocell mechanism where both microcell and macrocell corrosion processes co-exist. Potential and current measurements indicated a localized form of corrosion, around the crack, which would result in a local metal loss. Further, the localized corrosion rate of steel in the vicinity of a crack is much higher than the corrosion rate considering only the microcell process under similar conditions. The contribution of the microcell mechanism to the local rate of metal loss at the crack was shown to be much higher than the contribution of the microcell corrosion process. From an engineering point of view such local reduction in cross section of the rebars is dangerous for the safety of structures.

In macrocell corrosion systems, the average corrosion rate determined from traditional electrochemical measurements have previously been shown to under-estimate

the local corrosion rate by a factor ranging between five and ten (Elsener 2002). Most methods for determining the rate of corrosion rely upon applying external polarization to the system undergoing corrosion. This process is complicated in the case of steel embedded in cracked concrete due to the spatial variations in the resistance of the medium and the rates of corrosion, along the length of the bar. Understanding the response of a steel bar undergoing corrosion, which results from the formation of a macrocell, subjected to external polarization is essential for developing procedures which allow estimating the local corrosion rate in such a situation. Very limited work has been reported in the literature on modeling the polarization response of a macrocell system comprised of combined microcell and macrocell corrosion processes. Kranc and Sagues (2001) developed a numerical model for studying the response of a chloride-induced macrocell in a reinforcing steel bar placed in concrete, which is subjected to external potential polarization. Their model was based on an equivalent circuit representation of the steel bar and the concrete medium. Besides being computationally intensive, the circuit-based model considered only the heterogeneity resulting from oxygen concentration effects along the length of the bar. The influence of exiting current and potential distribution in a macrocell system on the current resulting from imposed potential was not considered in the model. The equivalent circuit model, nevertheless, provides an insight into the behavior of a spatially inhomogeneous system to external polarization. Numerical simulations revealed that the excitation current generated by external polarization enters predominantly the active area at the macrocell anode. This

observation was later verified through laboratory experiments on a model macrocell system comprising of steel bars in aqueous solutions [Elsener et al 1996]. However, the experimental response of steel bar embedded inside cracked concrete, which is subjected to external polarization, has not been reported so far.

In this chapter, results of an experimental program investigating the polarization response of steel in cracked concrete are reported. The experimental program uses the cracked concrete specimen with a segmental steel bar used for investigating the formation of macrocell in Chapter 3. The current flow in the specimen resulting from the external polarization is monitored using the electrical connections between the different segments of steel bars provided from outside the specimen. The potential of the steel bar was monitored using embedded reference electrodes placed close to the steel bar. It is shown that the applied polarization results in a spatial variation in the potential and current along the steel bar. The circuit-based model which was previously calibrated using the macrocell current measurements is used to predict the polarization response of the cracked concrete system. The results of the analysis indicate that due to the low polarization resistance of the active steel close to the crack, the applied current is confined to the active area.

6.1.2 Objectives

The objectives of the work presented in this chapter are

1. To determine the influence of external polarization (potential) on the response of the macrocell corrosion system in cracked concrete.
2. To establish an analytical/numerical procedure to determine rate of corrosion in cracked concrete from external measurement.
3. To develop procedures for obtaining the parameters in the model representation of the steel in cracked concrete.

6.1.3 Background on External Polarization Measurement on Macrocell System

Once macrocell steady state is reached, a macrocell current will flow through the anode and cathode. External polarization applied to such a system is shown schematically in Figure 6-1. When an external potential is imposed on the concrete surface using a CE, the imposed external potential will polarize the macrocell system and change the potentials of the macrocell anode and cathodes. At the same time, the imposed current will flow from the CE to the steel bar. Changes in the current distribution in the macrocell system in response to external potential polarization therefore result from two effects: (a) the change in the macrocell current due to potential shifts in the anode and cathode; and (b) additional current in the system due to external polarization. To evaluate the first effect, it is known from the previous analysis that the macrocell current in the system depends upon the polarization responses of the active and passive steel. The macrocell current depends upon the potentials of the anode and the cathode. Shifts in the potentials

of the anode and cathode in response to external polarization would produce changes in the macrocell current. The additional current due to external polarization would depend upon the local polarization resistances of the steel-concrete interfaces at different locations along the length of the steel bar and the medium resistance of concrete between the working electrode and the steel bar.

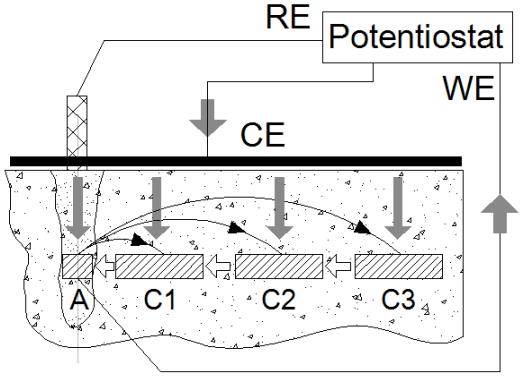

Figure 6-1: Schematic of macrocell corrosion under external polarization.

6.2 EXPERIMENTAL PROCEDURE

The concrete beam specimen with the segmental steel bar used previously for studying the formation of macrocell was used for polarization measurements. Polarization resistance measurements were conducted on the specimen once the macrocell steady state was reached. The polarization response of the macrocell system was investigated using three different test configurations: (a) small counter electrode (CE) at crack; (b) small CE away from crack; (c) large CE at crack, shown in Figure 6-2. Stainless steel plates were used as CE in all measurements. The small CE had a length equal to 5cm while the length

of the large CE was equal to the length of the beam specimen. For all measurements, an SCE placed on the concrete surface in the center of the CE was used as reference electrode (RE). Polarization experiments were conducted at a scan rate of 0.1 mV/s. Potential scans were initiated 10 mV below the open circuit potential up to 10 mV above the corrosion potential.

In the experimental setup all electrical connections were established using 10 Ω precision resistors. The currents in the system were determined by dividing the potential drop across the resistor by the magnitude of the resistance. As shown in Figure 6-2, Channel 1, labeled as Ch1, was used to collect the current flow between the CE and steel bar. The other channels, labeled as Ch2 to Ch7, were used to record the currents between segments C3-C4, C2-C3, C1-C2, A-C1, A-C5 and C5-C6, respectively. Data were collected from 14 seconds before the start of a potential sweep up to the end of the polarization using a high speed data acquisition system (IOtech™ WaveBook™). All channels were simultaneously sampled, discretized and recorded at a sampling rate equal to 100 Hz.

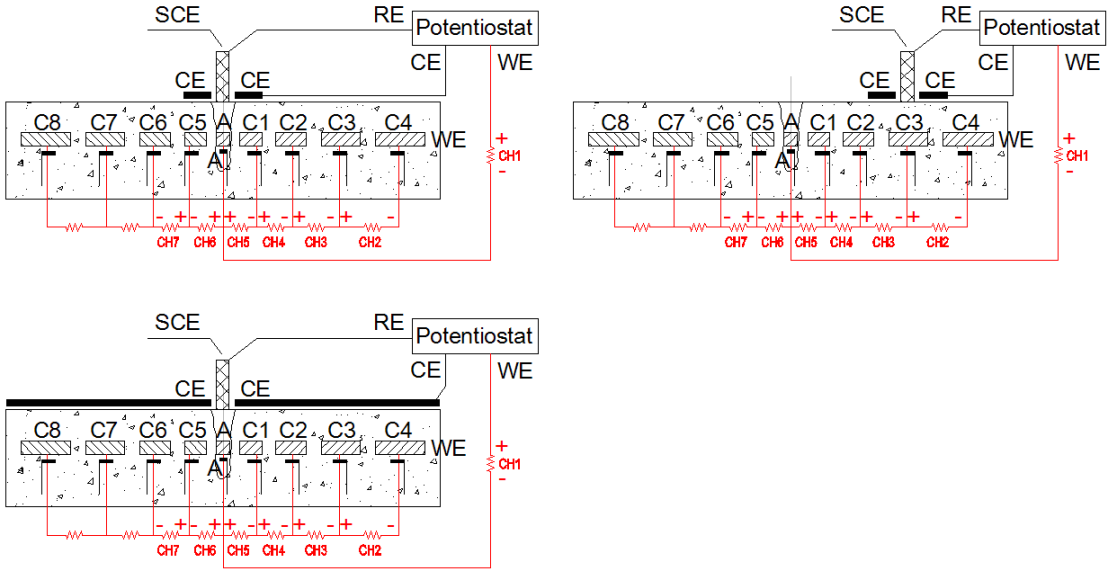

Figure 6-2: Test configurations used for polarization of macrocell. (a) small CE at crack; (b) small CE away from crack; (c) large CE at crack.

6.3 RESULTS

6.3.1 Data Processing

The collected data was filtered using a Butterworth filter to remove high frequency noise. A typical raw signal recorded by the data acquisition system which clearly shows the high frequency noise is shown in Figure 6-3. The filtered data is shown also in the figure, where the variation in the current resulting from the applied polarization can be clearly identified.

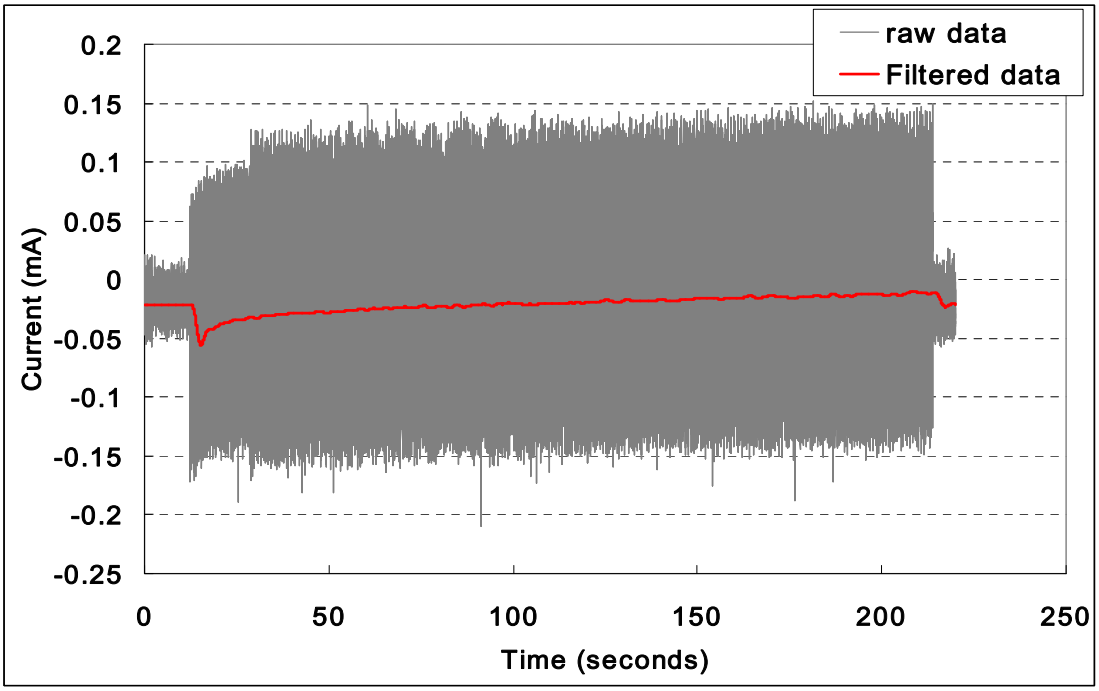

Figure 6-3: The raw data and filtered signal for imposed current measured by Channel 1.

The currents between the steel segments from a typical polarization test involving the large counter electrode are shown in Figure 6-4. The values of current in the first 14 seconds correspond to the steady state macrocell current distribution between the segments. During the test, the additional transient currents between the segments C3-C4, C2-C3, C1-C2, A-C1, A-C5 and C5-C6, are introduced due to the applied polarization. The total current, from the CE to the entire steel bar, measured by the potentiostat is also shown in the figure for comparison. In this graph, the potential scan for the LPR started at 14 seconds. It can be seen that there is an almost linear increase in the current between 50 to 200 seconds (36 to 186 seconds after the start of the scan). The change in current is therefore directly proportional to the change in the applied potential in this time range.

This suggests that between 50 to 200 seconds, there is a linear relationship between the applied potential polarization and the measured currents. In this time period, the applied potential, corresponding to 36 to 186 seconds of the potential sweep, varied from 6.4 mV below to 8.6 mV above the open circuit potential of the macro-cell in the steady state. Therefore, there is a 15 mV change in the external potential (with respect to the RE) during the linear period.

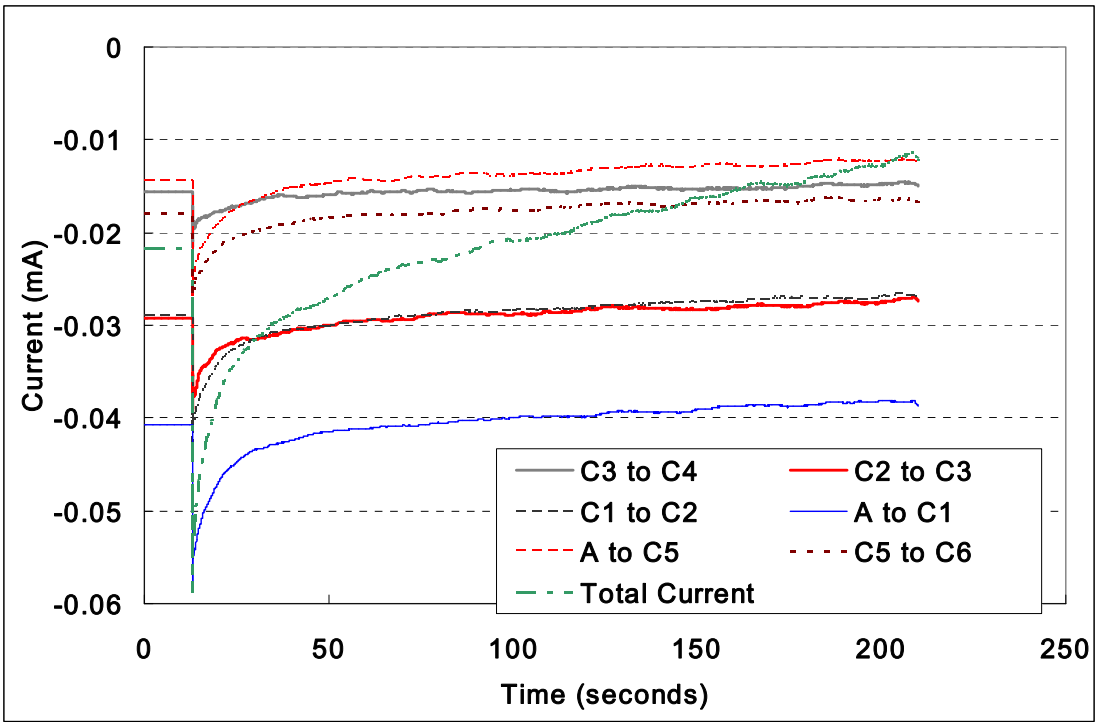

Figure 6-4: The imposed current flow through CE and current distribution between segments C3-C4, C2-C3, C1-C2, A-C1, A-C5 and C5-C6 during the polarization test.

The experimental response from all three test configurations indicated that the measured currents between the segments increased as a linear function of time between

36 and 186 seconds after initiating the scan. The time period, when measured current response indicated a linear increase with time is referred to as the linear time period in the following sections. The current increments between the beginning and end of the linear time period, which correspond to an applied potential increment of 15 mV, were calculated using a trend line which was fit to the measured currents during this time period. Data from the three test configurations in the linear time period were compiled and are presented next.

6.3.2 Results

Large CE at Center

In the case when the large CE was used to apply the polarization to the macrocell system, increments in measured currents in the linear time period are shown in Figure 6-5(a). The total current increment from CE to the entire steel bar was equal to 13.5 μA. The current increment between the segments A-C1 and A-C5 are equal to 3.1 μA and 2.3 μA, respectively. The current entering (or leaving) a steel segment through the steel-concrete interface during the linear time period were calculated as the difference between the measured currents recorded across its ends and are shown in the figure. The current flow directly from the CE to the anode is therefore equal to 8.1 μA, which implies that 60% of imposed external current flows directly to the macrocell anode while only 40% of applied current flows to the cathodes as shown in Figure 6-5(b).

Therefore, in spite of the relatively small area of anode when compared with the area of the entire cathode, during polarization, a significant portion of the imposed current from the CE flows through the anode.

The current density during the linear time period for each segment was calculated as the current flow to a segment through the steel-concrete interface divided by the surface area of the segment. The distribution of imposed current density for each segments are plotted in Figure 6-5(c). It is obvious that the current density at the anode is significantly higher than the current densities at the cathode. It should be noted that the area of the anode is significantly smaller than the area of the total cathode while the current through the anode is higher than the total current through the cathode. This translates into an order of magnitude difference between the current densities at the anode and the cathode during the applied polarization.

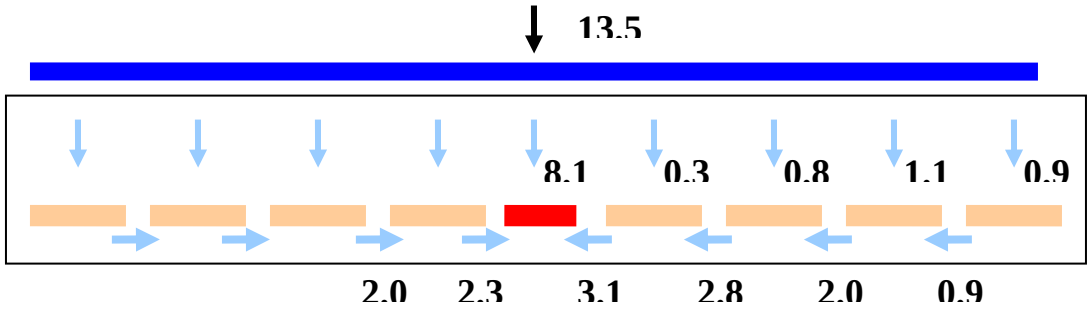

Figure 6-5(a): Imposed current distribution due to 15 mV potential change using large CE at crack (all currents in μA).

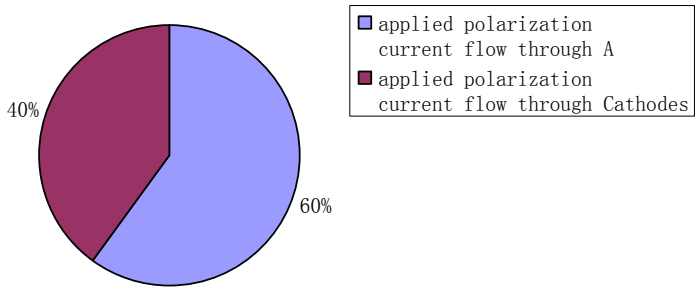

Figure 6-5(b): Comparison of applied polarization current flow through anode and cathodes

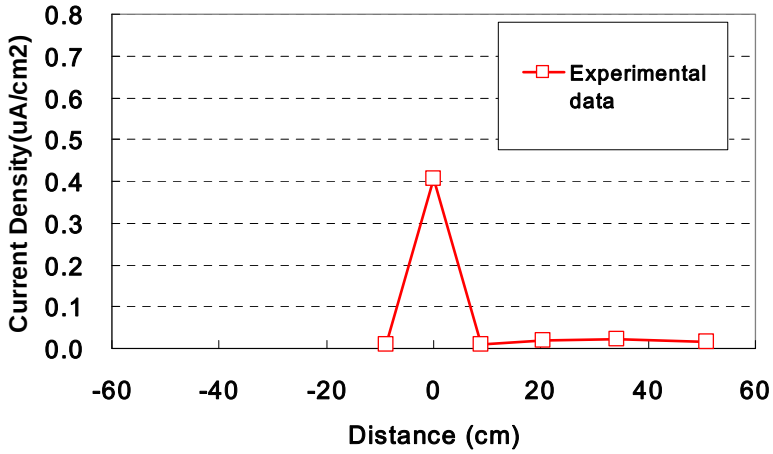

Figure 6-5(c): Current density distribution of applied polarization: (Large CE at crack)

Small CE at Crack

The increments of currents in the linear time period recorded from the case when a small CE placed above the crack was used to apply the polarization to the macrocell system, are shown in Figure 6-6(a). The total current from CE to the entire steel bar, was equal to 11.8 μA. It is interesting to note that while there is a significant difference in the size of the CE when compared with the previous case, there is a small difference in the total current between the two cases. The current increment in the linear time period

between the segments A-C1 and A-C5 are equal to 1.1 µA and 1.1 µA, respectively. In this case, the current flow directly from the CE to the anode is 9.6 µA, which implies 81% of imposed external current flows through anode while only 19% of current flow to the cathodes.

The distribution of imposed current density at each segment, are plotted in Figure 6-6(b). It is obvious that the current density at the anode is significantly higher than the current density at cathode. Further, the value of the current density through the anode is comparable to the previous case.

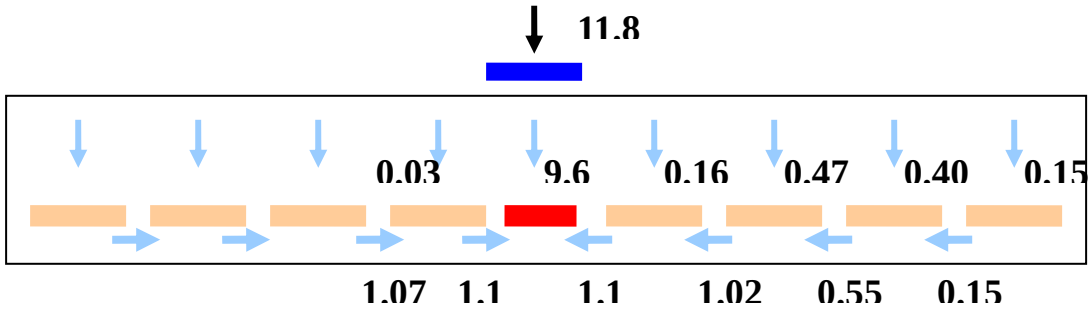

Figure 6-6(a): Imposed current distribution due to external polarization potential using small CE at crack.

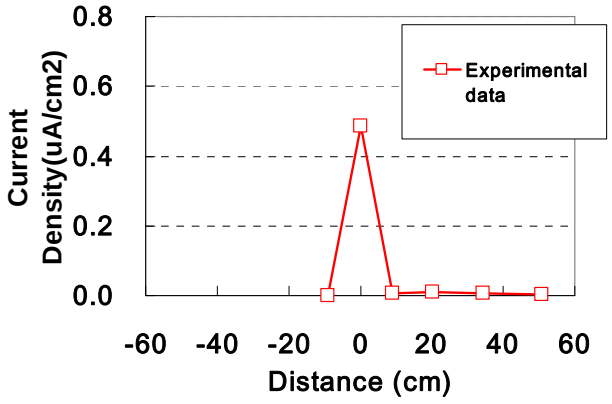

Figure 6-6(b): Current density distribution of applied polarization: (small CE at crack)

Small CE away from the Crack

The currents in the linear time period recorded from the case when a small CE placed away from the crack was used to apply the polarization to the macrocell system are shown in Figure 6-7(a). The total current increment in the linear time period, from CE to the entire steel bar, was equal to 3.3 µA. The current increment in the linear time period between the segments A-C1 and A-C5 are equal to 1.37 µA and -0.15 µA, respectively. Therefore, the current flow from the CE to the anode is 2.1 µA which implies that 64% of imposed external current flows through anode while only 36% of current flows to the cathode.

The distribution of imposed current density for each segments are plotted in Figure 6-7(b). It is obvious that even in this case the current density at the anode is significantly higher than the current density at cathode.

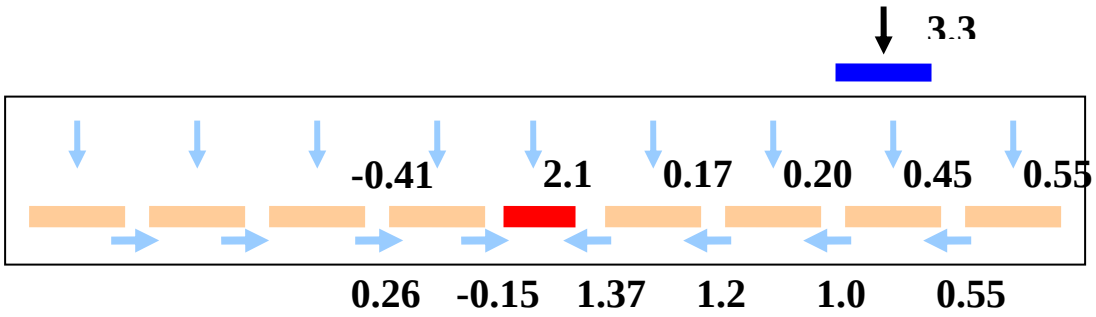

Figure 6-7(a): Imposed current distribution due to 15 mV potential change using small CE away from the crack.

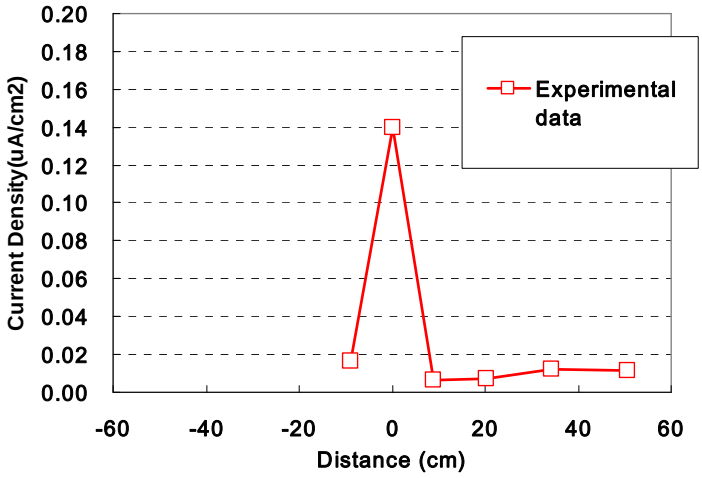

Figure 6-7(b): Current density distribution of applied polarization: (small CE away from crack)

Results from all three cases indicate that the current density through the anode is significantly higher than the current density through the cathode. Further, comparing the cases of large CE and small CE placed above the crack, there is no significant difference in the applied current. This suggests that the anode in a macrocell system plays a dominant role in determining the polarization response of the entire system. Even in the case when the CE was placed away from the crack, most of the imposed current from the CE flows through the anode. The observed current distributions from the three cases suggest that the macrocell anode offers little resistance to current flow and acts as a short circuit for flow of current.

6.4 SIMULATION OF POLARIZATION RESPONSE

6.4.1 Equivalent Circuit for Polarization of Macrocell

The equivalent distributed element circuit model for the macrocell system presented in chapter 5 is now modified to study the response of the macrocell corrosion system subjected to external polarization. External polarization to the macrocell system can be represented as an applied potential to the circuit. This is illustrated in Figure 6-8(a) for the case when external polarization of macrocell is applied using small CE at the crack. As shown in Figure 6-8(b), the current distribution in the macrocell corrosion system subjected to external polarization is a combination of the existing macrocell current and the current distribution resulting from the imposed potential polarization. In this representation, at macrocell steady state, V_0 is the potential measured between the steel bar and the concrete surface at the location of the crack. V_o is produced as a result of macrocell potential difference, E, between the anode and the cathode (the driving force of the macrocell). V_s is the imposed external potential increment applied on the concrete surface by the CE. The potential between the steel bar and the concrete surface at the crack during the polarization will therefore be equal to V_0+V_s. Experimental evidence suggests a linear relationship between the applied potential and the measured currents during the linear time period This suggests that the response of the entire system can be represented using linear elements such as resistances. The response of system subjected to macrocell battery E and external polarization V_s is equal to the sum of response of the

resistance network subjected to macrocell battery E and the response of the resistance network subjected to V_s as shown in Figure 6-8(c). Similar approach can be use to simulate the external polarization of macrocell using small CE at crack and small CE away from the crack.

The total applied external potential imposed by CE on the macrocell system is varies from a value ranging between 10 mV below to 10 mV above the macrocell equilibrium potential. During the linear time period the total change in applied potential is equal to 15 mV. The 15 mV potential shift is insignificant when compared with the potential difference of 300 mV provided by the macrocell battery. Further, during the linear time period, the macrocell system subjected to external polarization can be treated as a linear system. It is therefore reasonable to assume that during the polarization the values of R_p for the steel-concrete interface at the anode and the cathodes will remain constant at values obtained at macrocell steady state.

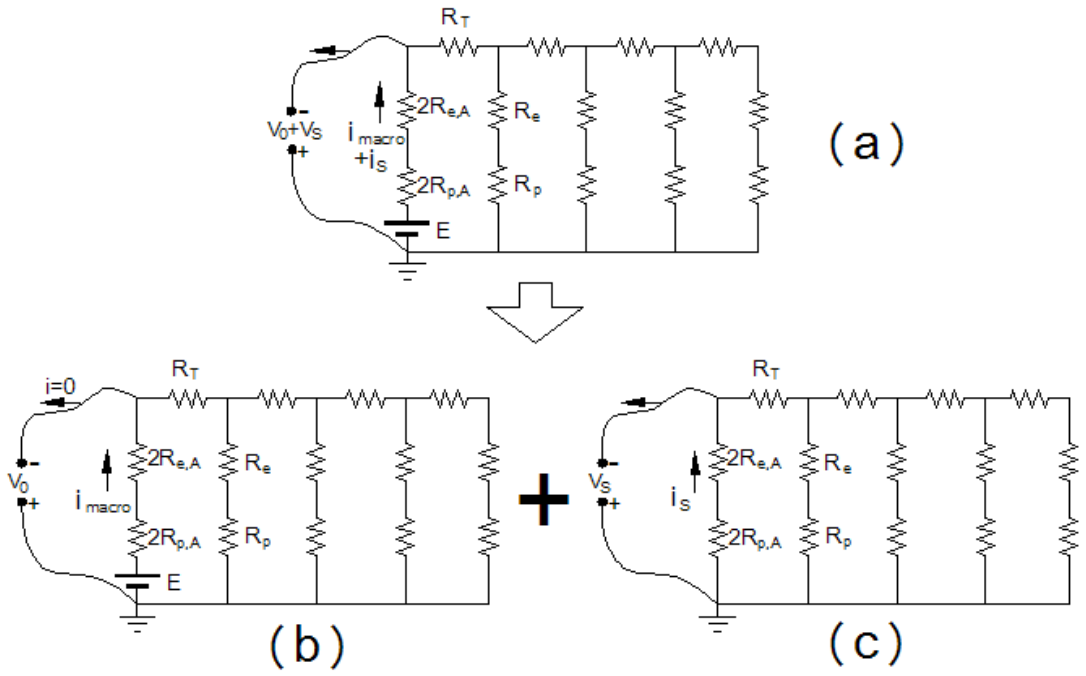

Figure 6-8: (a) equivalent circuit for external polarization on macrocell; (b) equivalent circuit for macrocell steady state; (c) equivalent circuit for system shift from macrocell steady state under external polarization.

The two-layer distributed element model with a battery proposed previously to represent the response of the macrocell system is now utilized to simulate the polarization response of macrocell subjected to external polarization. The circuit is appropriately modified to reflect the influence of the applied polarization for each of the cases considered. The results of the analysis are presented next.

6.4.2 Simulation Results

Large CE at crack

The circuit diagram for determining the response of the macrocell to external

polarization using large CE is shown in Figure 6-10(a). The large CE over the specimen surface functions as an equi-potential surface and therefore provides a short circuit to the longitudinal resistance at the concrete surface as shown in Figure 6-9.

During the polarization test, the reference electrode (SCE) was placed on the concrete surface right above the crack. The crack was filled with salt water which results in a conductive path of low resistance from the concrete surface to the steel/concrete interface. Therefore, there is no significant IR drop in the potential recorded by the RE; the potential recorded by the RE is equal to the potential drop across the steel/concrete interface. It can therefore be assumed that during the linear period of the potential scan, a 15 mV potential change was applied across the steel-concrete interface. In the simulation, the applied potential V_s was varied to obtain a 15mV potential drop across the resistor R_{pa}, representing the steel-concrete interface. It was found that a 15mV drop across the R_{pa} was achieved when Vs was equal to 20mV. In the circuit, this is represented as a battery which provides a potential difference of 20mV across the CE and the anode.

The imposed current predicted by the model is illustrated in Figure 6-10(a). The total induced current in the system to the applied incremental potential is equal to 9.4 μA. It can be seen that the change in the polarization current predicted by the circuit compares favorably with that measured experimentally (13.5 μA). Further, the change in the current between the anode and cathodes on either side are 2.5 μA, which agrees well with the measured values of 2.3 μA and 3.1 μA. Therefore, it can be concluded that the linear

polarization response of the macrocell can be accurately captured using the equivalent circuit. The equivalent circuit also allows us to determine the distribution of the applied current through the macrocell anode and the cathode as a result of the external polarization. The model predicts that for a total polarization current of 9.4 μA, 4.4 μA flow through the anode. The results of the analysis indicate that there is a variation in the spatial distribution of the applied current with respect to the crack. The current imposed by the application of external polarization is primarily confined to the active area located at the crack.

The distribution of imposed current density for each segment obtained experimentally and from the model prediction is plotted in Figure 6-10(b). The current densities predicted by the circuit compares favorably with that measured experimentally.

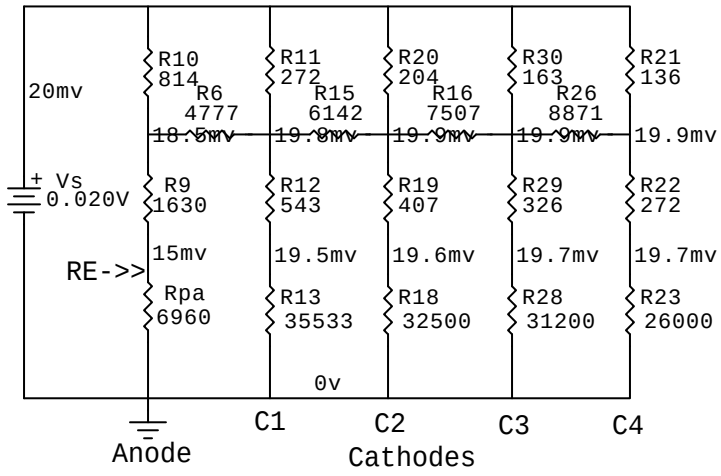

Figure 6-9: Model of external polarization using large CE at crack

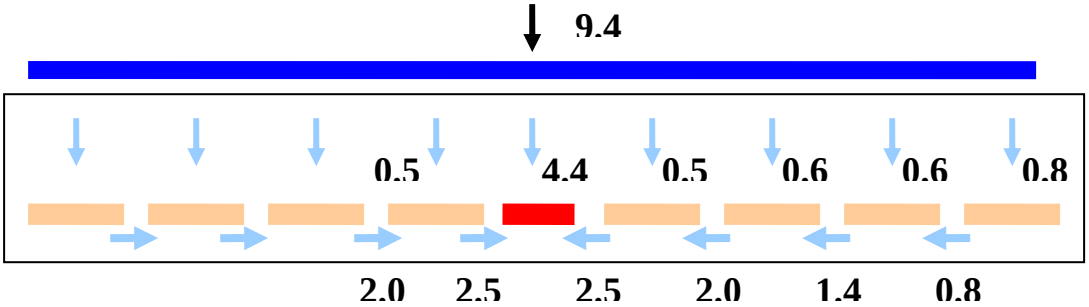

Figure 6-10(a) Model prediction of external polarization using large CE at crack

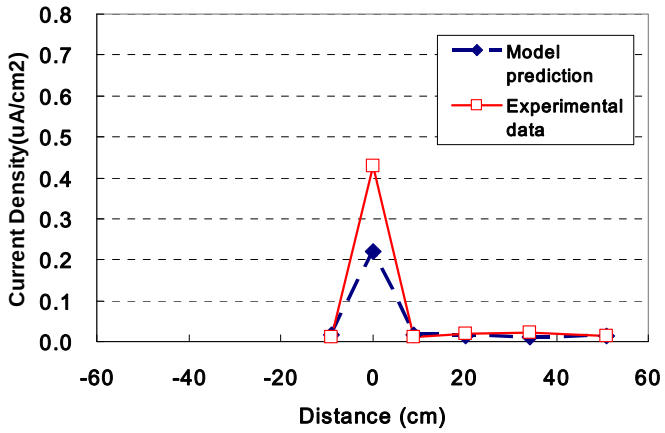

Figure 6-10(b): Imposed current density distribution by external polarization using large CE at crack.

Small CE at crack

The circuit diagram for determining the response of the macrocell to external polarization using small CE at crack is shown in Figure 6-11(a). Using an argument similar to that presented for large CE, it was found that the Vs corresponding to 15 mV potential difference between RE and steel-concrete interface was equal to 21 mV. The predicted imposed current by the model is shown in Figure 6-11(b). The change in the polarization current, 8.0 μA, predicted by the circuit compares favorably with that

measured experimentally (11.8 μA). Further, the change in the current between the anode and each side of cathode are 1.8 μA, which agrees well with the measured value of 1.1 μA and 1.1 μA.

The model predicts that for a total polarization current of 8.0 μA, 4.4 μA flow through the anode. The distribution of imposed current density for each segments from experimental data and model prediction are plotted in Figure 6-11(c). The imposed current predicted by the circuit also compares favorably with that measured experimentally. The results of the analysis indicate that there is a variation in the spatial distribution of the applied current with respect to the crack. The current imposed by the application of external polarization is primarily confined to the active area located at the crack.

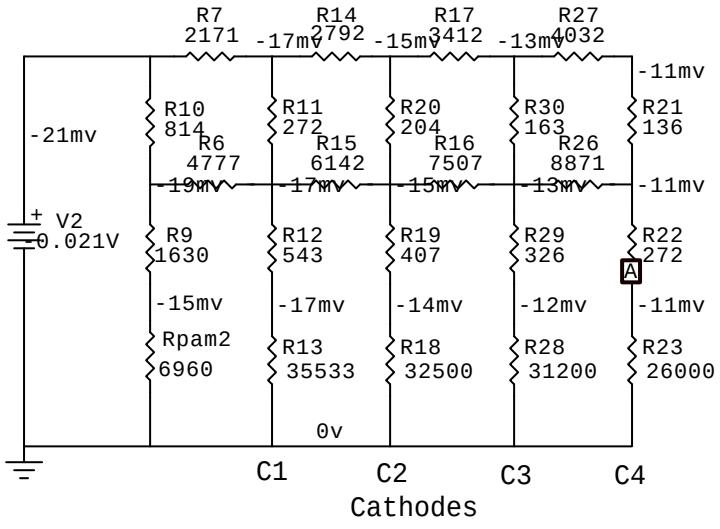

Figure 6-11(a): Model of external polarization using small CE at crack

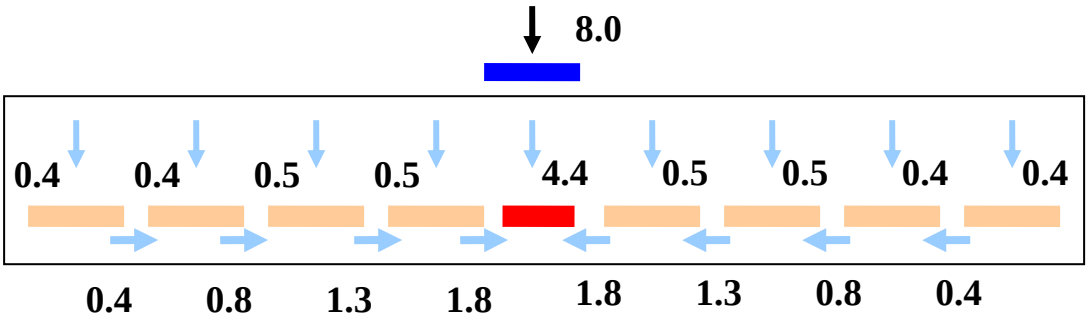

Figure 6-11(b): Model prediction of external polarization using small CE at crack

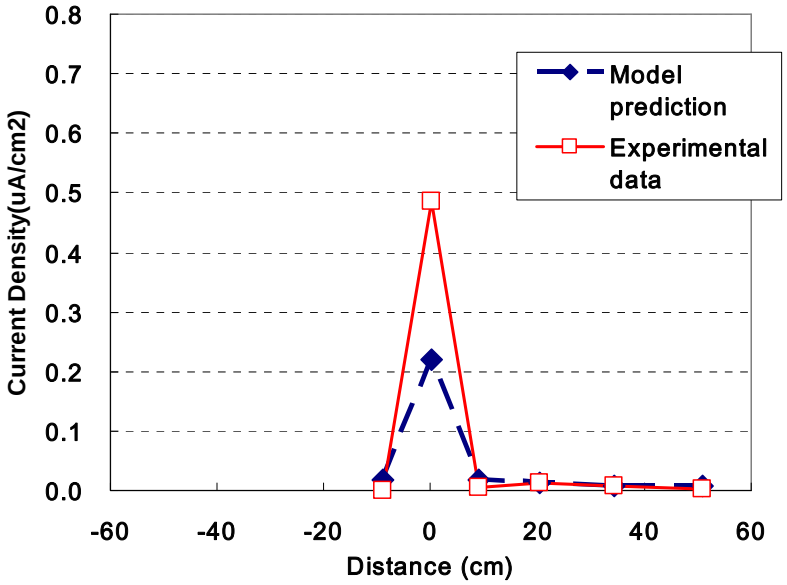

Figure 6-11(c): Imposed current density distribution by external polarization using small CE at crack.

Small CE away from crack

In this case, because the CE was placed on one side of the cathode, the corrosion system does have symmetry along the crack. Therefore, the full equivalent circuit with both left and right side was used to simulate the response of macrocell undergoing

external polarization. The circuit diagram for determining the response of the macrocell to external polarization using small CE away from the crack is shown in Figure 6-12(a). The reference electrode (SCE) was placed on the concrete surface right above the C3. During the LPR measurement, Vs, which equal to the potential between RE and steel-concrete interface, will be 15 mV during the LPR sweep in the linear time period.

The predicted imposed current by the model was illustrated in Figure 6-12(b). It can be seen that the change in the polarization current, 3.0 μA, predicted by the circuit is compares favorably with that measured experimentally (3.3 μA). Further, the predicted change in the current between the anode and left side and right side of cathodes are 0.4 μA and 1.5 μA, respectively, which agrees well with the measured value of -0.15 μA and 1.37 μA. Therefore, it can be concluded that the linear polarization response of the macrocell can be accurately captured using the equivalent circuit. The equivalent circuit also allows us to determine the currents through the macrocell anode and the cathode as a result of the external current due to the polarization. The model predicts that for a total polarization current of 3.0 μA, 1.1 μA flow through the anode. The distribution of imposed current density for each segments from experimental data and model prediction were plotted in Figure 6-12(c). It is obviously that the imposed current predicted by the circuit is compares favorably with that measured experimentally. The results of the analysis indicate that there is a variation in the spatial distribution of the applied current with respect to the crack. The current imposed by the application of external polarization

is primarily confined to the active area located at the crack.

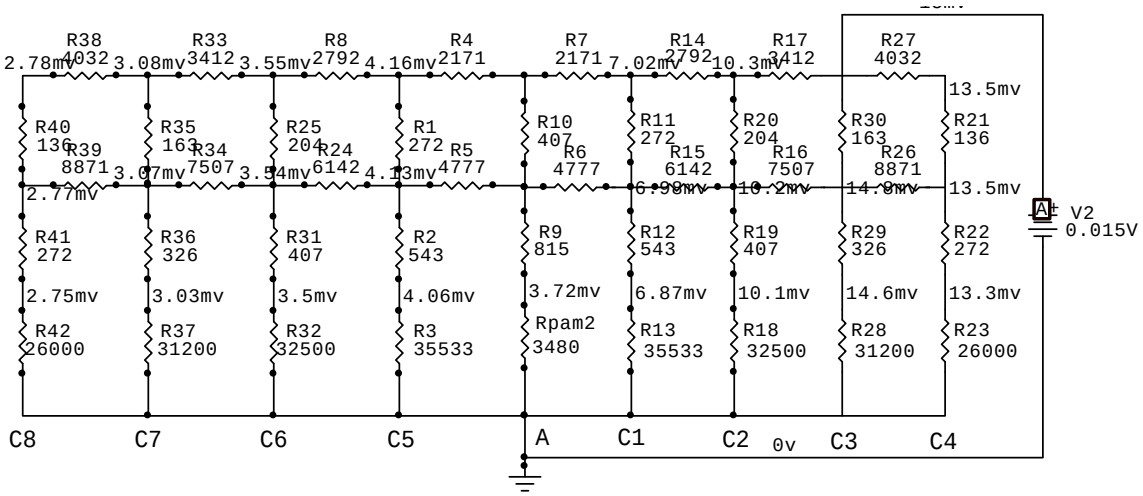

Figure 6-12(a): Model of external polarization using small CE away from the crack

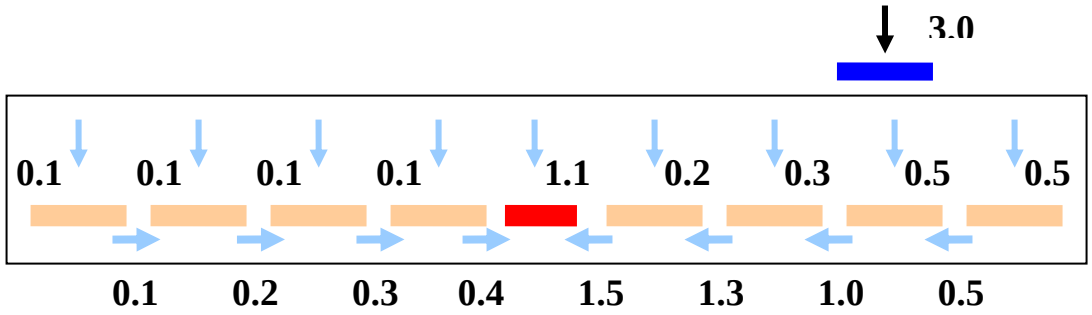

Figure 6-12(b): Model prediction of external polarization using small CE away from the crack

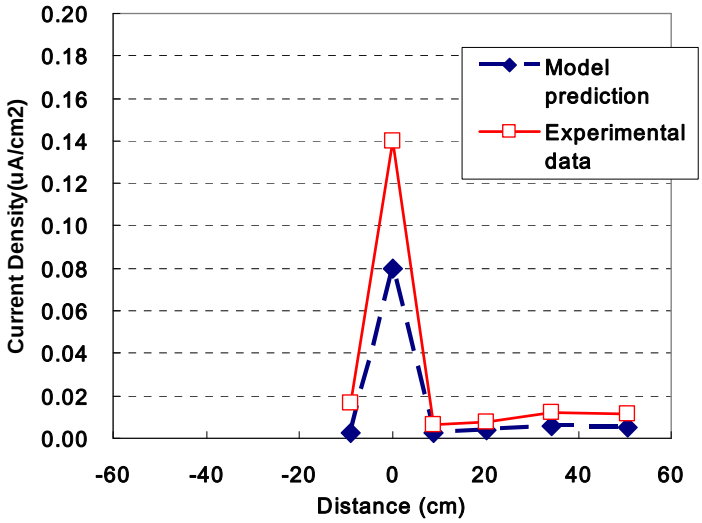

Figure 6-12(c): Imposed current density distribution by external polarization using small CE at crack.

6.5 DISCUSSION

As shown in chapter 5, concrete resistivity plays an important role in the macrocell system. Further, concrete resistivity is also a key factor in determining the LPR response of the macrocell corrosion system. Considering the case when polarization was applied using the large CE, 22% of the imposed current, flowed through the cathode. This indicates that the role of the cathode is not insignificant and cannot be ignored while determining the polarization response of the macrocell corrosion system. However, the contribution of the cathode decreases when the concrete resistivity increases. When the concrete resistivity is very large, the concrete medium forms a barrier for current flow to the cathode. In this case, the anode will be isolated and all of imposed current will flow towards the anode. The LPR behavior of isolated anode will be similar to that of active

steel located at the crack undergoing microcell corrosion.

From the results presented in the previous section, it appears that the linear polarization response of the macrocell can be accurately captured using the proposed equivalent circuit. The distribution of current through the macrocell anode and the cathode as a result of external polarization can also be determined using the equivalent circuit model. It appears that during polarization, the distribution of the applied current is not uniform across the length of the steel bar; a significant portion of the current flows to the macrocell anode. Therefore, the use of linear polarization to estimate the corrosion of steel in cracked concrete requires a careful consideration of the localized area of active steel located at the crack. The influence of the non-uniform current distribution in the presence of the crack is similar to the problem associated with LPR measurements in large structures. Feliu (1988) reported that when LPR is applied to real large size structure, the main difficulty is related to the non-uniform distribution of the electrical signal applied to the reinforcement when the surface area of the CE is much smaller than that of the reinforced concrete structure to be tested. In this case, it was found that the apparent R_p, obtained from LPR measurement, underestimates the corrosion rate.

6.5.1 Interpreting Corrosion Rate from LPR Data in Macrocell Corrosion System

The polarization resistance of steel in cracked concrete estimated using a large counter electrode under the assumptions of uniform corrosion would severely

under-estimate the local corrosion rate. This is illustrated considering the case when a large CE was used to polarize the specimen. If the results obtained from the LPR test were interpreted assuming uniform corrosion along the length of the steel bar, the value of the polarization resistance underestimates the actual rate of metal loss at the crack. Considering the total area of the steel bar ($A=L\pi\phi$) equal to 466 cm^2, the measured increments in potential (ΔE) and total applied current (ΔI), the apparent R_p is obtained as

$$R_{p,a} = (\Delta E/\Delta I)*A = 15\ mV/13.5\ \mu A*466\ cm^2 = 520000\ \Omega cm^2.$$

Considering accepted practice for interpreting the LPR data (Table 2-2 in Chapter 2), because $R_p > 260{,}000\ \Omega cm^2$, this indicates that the steel is in a passive state and $i_{corr} < 0.1\ \mu A/cm^2$. The corrosion rate for the apparent polarization resistance obtained using Stern-Geary equation is given as

$$i_{corr} = B/R_p = 26\ mV/520000\ \Omega cm^2 = 0.05\ \mu A/cm^2.$$

As per ASTM G102, a corrosion rate of 0.05 $\mu A/cm^2$, corresponds to a metal loss of 0.58 μm/Year. However, the actual local corrosion rate obtained previously in chapter 4 was equal to 2 $\mu A/cm^2$, which corresponds to 23.2 μm/Year metal loss. In this case, interpretation of the LPR data assuming uniform corrosion underestimates the real corrosion rate by a factor of 40.

6.5.2 Application of the Circuit Model to Field Measurements

Field measurement of macrocell corrosion for real structures is significantly more difficult than the controlled laboratory study presented here. The specimen discussed in chapters 4 and 5 uses a segmental steel bar with external connection which provides an easy access to measure the macrocell current flow through anode and each of the cathodic segments, thereby allowing for a direct determination of the spatial variation of current along the steel bar. In real structures, however, it is impractical to break the steel bars for measuring I_{macro} and other means of determining the macrocell current directly do not currently exist. This is compounded by the problem of using a technique such as LPR for determining the rate of corrosion, since the distribution of the imposed current between the macrocell anode and cathode is not readily determinable. In LPR measurements on a steel bar embedded in cracked concrete, only the total imposed current and potential shift of steel at the crack produced by the external polarization can be determined with certainty. The equivalent circuit model can provide a fundamental insight into interpreting the LPR response of a macrocell corrosion system in cracked concrete.

An implementation of the equivalent circuit model for a steel bar in cracked concrete, is now developed, which can then be used to interpret the response of the system to applied polarization. Using the model, the macrocell current in the system can be determined from the measured LPR response. Some key issues required for implementing the model, related to parameters which are not readily available, are now discussed.

The resistances of the concrete medium R_t and R_r, can be determined using the concrete resistivity and from the known geometry of the structure. The concrete resistivity (ρ), can be measured in field using the approach discussed in chapter 5. The R_{pc} can be obtained using the typical R_p value for passive steel (as shown in chapter 5) multiplied by the area of cathode. The length and area of cathode can be obtained from design drawing or from field measurements. Typically the total area of connected steel forms the cathode. The typical R_p value for active steel is also known. The area of anode, required for determining R_{pa}, is however unknown. The value of V_s, the applied external potential for achieving a known potential change registered by the RE is also unknown. From the experimental results presented here it is known that the applied polarization primarily results in a change in the potential at the anode. The potential measured by the RE reflects the change in potential across the steel concrete interface at the anode. Thus, in the model the values of R_{pa} and V_s can be varied until the applied V_s produces a desired change of potential across the R_{pa}. The model with the parameters obtained in the manner described could be used to obtain a first estimate of the rate of macrocell corrosion.

The procedure of determining the equivalent circuit model for the macrocell corrosion system for steel bar embedded in cracked concrete is now illustrated considering the case of the LPR experiment using the large CE. The model for this system is developed using the procedure discussed before and the results are compared

with the actual experimental values. From the LPR experiment using large CE at crack as shown in Figure 6-5(a), the total imposed current was equal to 13.5 μA and the potential between RE and steel was 15 mV. In the model, shown in Figure 6-13, the R_{pc} at the cathode were determined using the typical value of R_p for passive steel equal to 2.6e6 Ωcm^2. In the simulation, the applied potential V_s and R_{pa} were varied to obtain a 13.5 μA total current and 15 mV potential shift across R_{pa} by the external polarization. The values of V_s and R_{pa} were determined to be 23.8 mV and the 4000 Ω, respectively. The results of the analysis are shown in Figure 6-14. The predicted current of 7.6 μA to the anode agrees very favorably with the experimental value of 8.1 μA. The 3 μA current flow to each side of cathode is also very close to 2.7 μA measured experimentally. It appears that the simplistic assumptions not withstanding the proposed implementation of the equivalent circuit model provides reasonable prediction of the polarization behavior of the macrocell corrosion system.

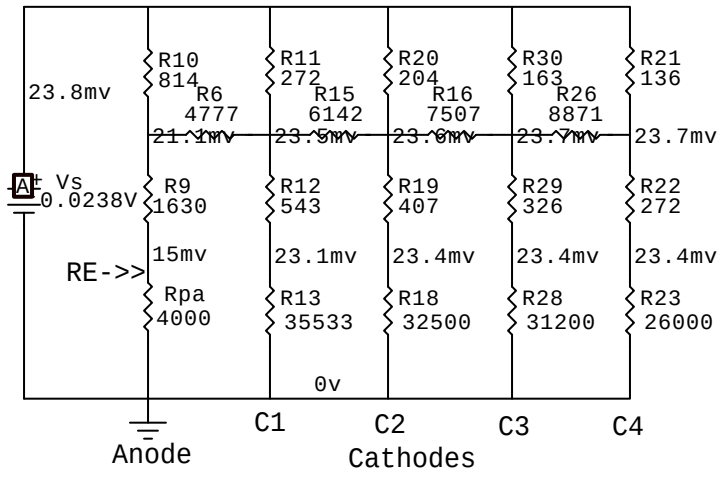

Figure 6-13: Model for the macrocell using known parameters

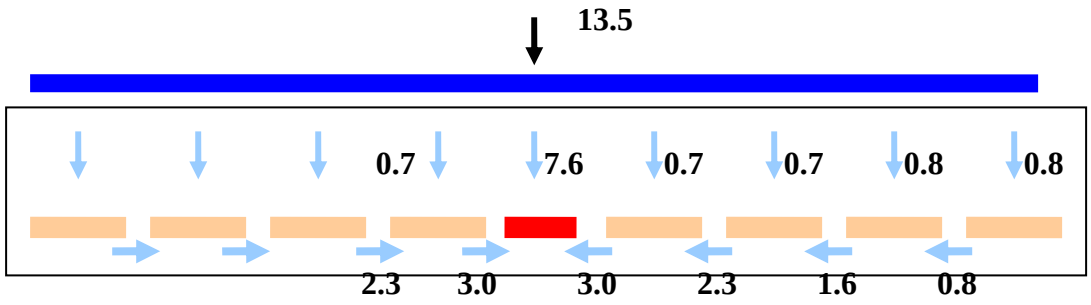

Figure 6-14: Imposed current predicted by model

Once the model is established and the R_{pa} is determined from a polarization test, the macrocell current can be determined by introducing the 300 mV battery in the circuit. The equivalent circuit for the macrocell is shown in Figure 6-15. The predicted macrocell currents in the macro-cell corrosion system are shown in Figure 6-16. The predicted macrocell current from the anode to cathodes on either side of the crack is equal to 17.4 μA. The predicted value compares favorably with the 20 μA obtained experimentally. Considering model symmetry discussed in chapter 5, the R_{pa}^{*} of the anode is equal to 4000/2 = 2000 Ω. Considering the 70 mV potential shift from the rest potential as shown in Figure 6-15, the R_{pa}^{*}/R_p ratio is equal to 2.2 by equation (5.8). Therefore, the real R_p at rest potential can be obtained as

$$R_p = 2000/2.2 = 908\ \Omega$$

The area of anode can be determined using the typical polarization resistance of active steel as shown in chapter 4.

$A = 2.9e4\ \Omega cm^2 / 908\ \Omega = 31.9\ cm^2$

The predicted 31.9 cm^2 anode area compares favorable to the 20 cm^2, the actual size of the anodic segment. The macrocell current density is equal to 34.8 μA/31.9 cm^2 = 1.1 μA/cm^2. The corresponding metal loss is equal to 12.8 μm/year, which compares favorably with 23.2 μm/year obtained experimentally.

The comparison of metal loss obtained from the proposed approach and regular LPR is shown in Table 6-1. It can be seen that the proposed approach provides a more accurate prediction of the metal loss than the regular LPR. The prediction using the proposed implementation of the equivalent circuit is significantly improved when compared with the conventional interpretation of data.

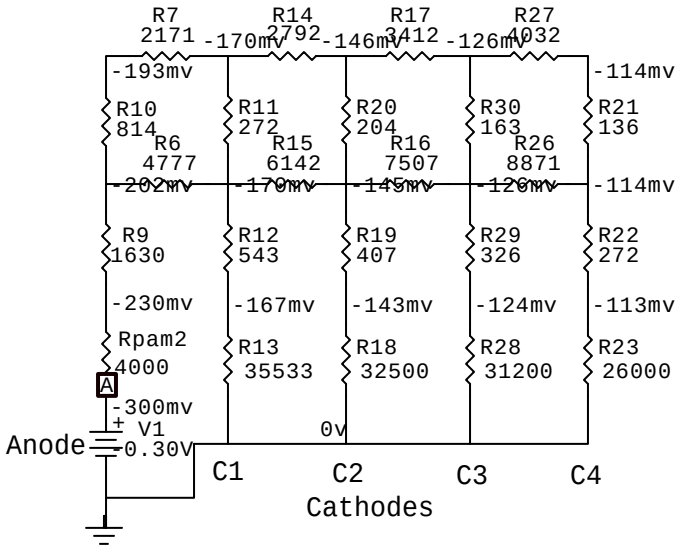

Figure 6-15: Model to predict the macrocell corrosion current.

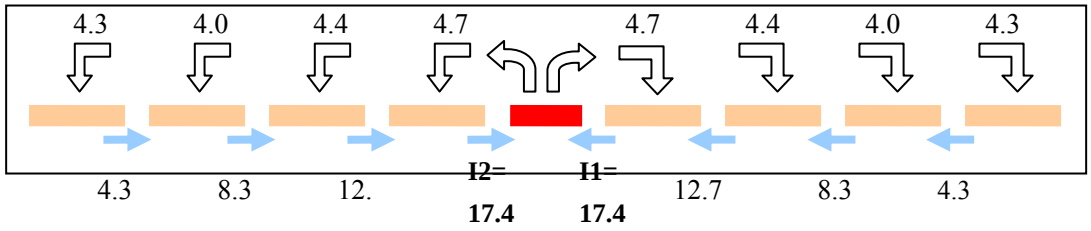

Figure 6-16: Macrocell current predicted by the model

Table 6-1: Comparison of metal loss obtained from experiment to proposed approach and regular LPR

	Metal loss (μm/year)	Accuracy
Experiment	23.2	--
Proposed approach	12.8	55%
Conventional interpretation of LPR	0.58	2.5%

The proposed implementation of the equivalent circuit model provides an approach for determining the rate of metal loss in a steel bar embedded in cracked concrete. Additionally this method also allows for estimating the size of the anode and the total macrocell current from field measurements, which are not available using conventional means. The procedures outlined here for implementing the equivalent circuit model provide a first estimate and do not account for changes in R_p of the cathode due to potential shift produced by the macrocell. Improved estimates of the macrocell current can be obtained by revising the value of R_p based on the values of potential predicted by the model. The proposed approach for implementing the equivalent circuit model

nevertheless provides reasonable estimates of metal loss and presents a significant advancement of the current state of the art. The value of R_p and for the cathode can be adjusted iteratively until convergence is achieved.

6.6 CONCLUSIONS

The results of an experimental program investigating the polarization response of steel embedded in cracked concrete are presented in this chapter. A distributed element model, derived from the equivalent circuit model for the macrocell corrosion system, is presented for simulating the polarization response of the macrocell system. An approach to obtain the macrocell corrosion rate in the field measurement is proposed. Based on the results obtained, the following conclusions can be drawn:

1. There is a spatial variation in the applied current with respect to the crack. The current imposed by the application of external polarization is confined to the active area close to the crack.

2. The modified distributed element model obtained from the equivalent circuit model for the macrocell corrosion system provides a more accurate prediction of the polarization response of the macrocell system than existing models.

3. It is expected that the implementation of the equivalent circuit model for field applications will lead to an improved estimate for predicting the rate of corrosion in

cracked concrete. The size of the anode and the macrocell corrosion current can be estimated using the prescribed procedure.

CHAPTER 7
CONCLUSIONS

Importance of the Subject

Corrosion of reinforcing steel in cracked concrete is a localized phenomenon, which is initiated by the easy access of ions to the steel surface at the location of the crack. Local depassivation of steel at the crack results in a very rapid initiation of corrosion, which is sustained by both the microcell and macrocell mechanisms. The macrocell corrosion system which is established along the length of the steel bar results in a spatial variation of potential and a distribution of current relative to the location of the crack. The rate of metal loss at the crack due to the combined micro and macrocell mechanisms is significantly higher than the rate predicted considering uniform microcell corrosion. Predicting the local rate of metal loss using established electrochemical techniques which utilize external polarization has been shown to be unreliable. Fundamental understanding of several issues, which have prevented the development of reliable procedures to interpret data from a polarization test and infer the local rate of metal loss are: (a) a representation of macrocell corrosion system in terms of the kinetics of the reactions involved is not available; (b) the relationship between the microcell and macroell mechanisms is not understood; (c) the response of the macrocell system to applied

polarization has not been investigated to date.

In this study an experimental investigation of the macrocell corrosion system in a reinforcing bar in cracked concrete is presented. An equivalent circuit model for the macrocell corrosion system, which allows for interpreting the polarization response of macrocell system, is developed. Finally, a procedure for implementing the equivalent circuit model for predicting the rate of local metal loss in a macrocell corrosion system is presented.

Summary of the work

The focus of work presented in this thesis is the experimental investigation and theoretical study to investigate the behavior and mechanism of corrosion of steel rebar in cracked concrete. First, a circuit representation for the steel-concrete interface is determined using measurements from a reference electrode at the concrete surface and an embedded electrode near steel-concrete interface. Second, the relationship between magnitudes of the microcell and macrocell corrosion rates in a macrocell system is determined. A representation of the macrocell corrosion system is developed using the polarization responses of active and passive steel in concrete in Evan diagram. Third, an equivalent circuit model is presented to simulate the spatial variations of current and potential in the macrocell system. A variable polarization resistance is introduced to capture the real behavior of the steel-concrete interface which is removed from its rest potential. From a parametric analysis, key factors which influence the formation and state

of macrocell are identified. Fourth, the polarization response of steel in cracked concrete are studied experimentally and simulated using the proposed distributed element model. Finally, a practical approach for field implementation the equivalent circuit model to predict the LPR response of a macrocell corrosion system is developed.

The key findings of the research presented in this thesis are:

1. A parallel combination of charge transfer resistance and a constant phase element (CPE) to represent the double layer capacitance is found to be suitable for both active and passive steel. CPE response is prominent in active corrosion. The value of n for the CPE element was found to be in the range (0.65-0.75). Passive steel exhibits a response which is closer to a pure capacitance.
2. Concrete has a significant influence on the impedance spectrum measured from the concrete surface at both the low and the high frequencies. At low frequencies the presence of diffusion in concrete overlaps with the contribution of the steel-concrete interface. The steel-concrete interface predominantly contributes in the low frequency (at and below 10 Hz) region of the impedance spectrum.
3. The CPE behavior of the steel-concrete interface only affects the response during the initial portion of the potential sweep in LPR measurement. In the latter part, a purely resistive response is obtained from both the concrete and the steel-concrete interface. A model considering a simplified representation using with pure resistances is sufficient for modeling the polarization response of steel embedded in concrete.
4. The macrocell system can be interpreted combining the Tafel behavior of the active

steel and passive steel. The relationship between the potential and the macro and microcell currents can be obtained from the Tafel polarization responses of the active steel and passive steel in cracked concrete. The relationship between the macrocell and microcell corrosion rates can be studied using the Tafel representation. In the macrocell corrosion system established along the length of the steel bar in cracked concrete, the macrocell corrosion mechanism is the dominant component contributing significantly to local metal loss at the crack. Macrocell corrosion rate can be 30 times the microcell corrosion rate. In macrocell corrosion system, for a given ratio of area of the anode to the area of cathode, there is a decrease in the microcell current density at the anode with an increase in the macrocell current density.

5. The proposed distributed element model provides favorable prediction of the macrocell corrosion of steel in cracked concrete. Variable R_p, considering the influence of potential shift away from rest potential, provides a more accurate prediction than the model using initial R_p.
6. Concrete resistivity is a key factor affecting not only the magnitude but also the existence of the macrocell corrosion.
7. The proposed implementation of the equivalent circuit model provides an approach for determining the rate of metal loss in a steel bar embedded in cracked concrete. Additionally this method also allows for estimating the size of the anode and the total macrocell current from field measurements, which are not available using

conventional means. There is a twenty-fold increase in the accuracy of predictions when compared to the conventional interpretation of LPR data.

8. The proposed approach advances our understanding of the localized corrosion mechanism in cracked concrete and provides a practical way for in-site evaluation of the macrocell corrosion rate.

Suggested Future Work

Certain structures, especially highway bridges, are subjected to both fatigue loading and corrosion. Corrosion of steel in structural members subjected to repeated loading has not been investigated to date. Research studies which report on the influence of fatigue loading on the corrosion of steel embedded in concrete are currently not available in the literature. Repeated loading produces a periodic opening and closing of the crack resulting in a periodic change in the oxygen diffusion through the crack and an increasing debonding of steel rebar close to the crack surface. This load induced effect can potentially change the environment in the steel bar close to the crack face when compared with a cracked beam subjected to static loading. Therefore, a change in the mechanism and/or rate of corrosion can be expected in cracked beams subjected to repeated loading. This area is a prospective area for future study.

BIBLIOGRAPHY

1. ACI, *Control of Cracking in Concrete Structures*, ACI 224R-01, 2007
2. ACI, *Protection of Metals in Concrete against Corrosion*, ACI 222R-01, 2007
3. Aligizaki, Kalliopi.K., *PhD Thesis: Modeling of concrete cracking due to corrosion of embedded reinforcement*, PSU, 1999
4. Alonso, C., Andrade, C. and Diez, J.M., *Factors controlling cracking of concrete affected by reinforcement corrosion*, Mat's and structures, v31, pp. 435-441, 1998
5. Al-tayyib, A., Khan, M.S., *Corrosion rate measurements of reinforcing steel in concrete by electrochemical techniques*, ACI Mat's J, v85, pp. 172-177, 1988
6. Andrade, C. and Gonzales, J.A., *Quantitative Measurements of Corrosion Rate of Reinforcing Steels Embedded in Concrete Using Polarization Resistance Measurements*, Werkstoffe und Korrosion, v29, pp. 515-519, 1978
7. Andrade, C., Alonso, M.C., *Values of corrosion rate of steel in concrete to predict service life of concrete structures*, ASTM STP 1194, 1994
8. Arya, C., *Supercover concrete*, Concrete, v28, n4, pp. 30-31, 1994
9. Ayra, C, *Influence of cathode-to-anode area ratio and separation distance on galvanic corrosion currents of steel in concrete containing chlorides*, Cement and Concrete Research, v25, n5, pp. 989-998, 1995
10. Ayra. C, *Influence of crack frequency on reinforcement corrosion in concrete, Cement and concrete research*, v26, n3, pp. 345-353 , 1996
11. Atimay, E., and Ferguson, P. M., *Early Chloride Corrosion of Reinforced Concrete—A Test Report*, Materials Performance, V. 13, No. 12, 1974, pp. 18-21.
12. Bard, A.J. and Faulkner, L.R., *Electrochemical Methods: Fundamentals and Applications*, John wiley & sons, 2001
13. Beeby, A. W., Corrosion of Reinforcing Steel in Concrete in Its Relation to Cracking, The Structural Engineer (London), V. 56A, No. 3, 1978, pp. 77-81.
14. Berke, N.S., Dallaire, M.P., Hicks, M.C., Grace, W.R. and Company-Conn, *Effect of calcium nitrite on the corrosion fatigue of steel in cracked concrete*, Corrosion 91, No. 550, 1991
15. Berke, N.S., Dallaire, M.P., Hicks, M.C., Hoopes, R.J., *Corrosion of steel in cracked concrete*, Corrosion 93, No. 322, 1993

16. Berke, N.S., Dallaire, M.P., Hicks, M.C., Hoopes, R.J., *Corrosion of steel in cracked concrete*, Corrosion 91, 1991

17. Bertolini, L., Elsener, B., Pedeferri, P and Polder, Rob B., *Corrosion of Steel in Concrete: Prevention, Diagnosis, Repair*, Wiley-VCH, 2003

18. Borgard, B., Warren, C. Somayajiu, S. and Heidersbach, R., *Correlation between corrosion of reinforcing steel and voids and cracks in concrete structures*, Transportation Research Record 1211, pp.1-11, 1989

19. Broomfield, J.P., *Corrosion of Steel in Concrete: understanding, investigation and repair*, Routledge mot E F & N Spon , 1997

20. Broomfield, J.P., *Assessing corrosion damage on reinforced concrete structures Corrosion and corrosion protection on steel in concrete, V.1, Proceeding of international conference*, University of sheffield, UK, R.N. Swamy, ed , pp. 1-25 , 1994

21. Carino, N.J., *Nondestructive techniques to investigate corrosion status in concrete structures*, J. Performance of Construction Facilities, v13, n3 , pp. 96-106, 1999

22. Crane, A.P., *Corrosion of reinforcement in concrete construction*, Society of chemical industry, 1983

23. Crentsil, K. K. S., Glasser, F. P., and Irvine, J. T. S., *Electrochemical Characteristics of Reinforced Concrete Corrosion as Determined by Impedance Spectroscopy*, British Corrosion Journal, v27, pp. 113–318, 1992

24. Darwin, D., Manning, D., Hognestad, E, Beeby, A. Rice, P. and Ghowrwal, A, *Debate: crack width, cover and corrosion*, Concrete International, pp. 20-35, 1985

25. Derrien, F., Chahbazian, G., Carpio, J., Raharinaivo, A., *Cathodic polarization behavior of steel in solutions simulating concrete*, Cement and Concrete Research v20, 1990

26. Dhouibi, L., Triki, E., Raharinavo, A., *The application of electrochemical impedance spectroscopy to determine the long-term effectiveness of corrosion inhibitors for steel in concrete*,Cement and concrete composites, v24, pp. 35-43, 2002

27. Dhouibi-Hachani, L., Triki, E., Grandet, J., Raharinaivo, A., *Comparing the steel-concrete interface state and its electrochemical impedance*, Cement and Concrete Research, v26, n2, pp. 253-266, 1996

28. Elsener, B., *Macrocell corrosion of steel in concrete-implications for corrosion monitoring*, Cement and concrete composites, v24, pp. 65-72, 2002

29. Elsener, B., *Half-cell potential mapping to assess repair work on RC structures*, Construction and Building Mat's, v15, pp. 133-139, 2001

30. Elsener, B., *Corrosion rate on reinforced concrete structures determined by electrochemical*

methods, Mat's Science forum Vols, v192-194, pp. 857-866 , 1995

31. Elsener, B., *Corrosion rate of steel in concrete-from laboratory to reinforced concrete structures in Corrosion of Reinforcement in Concrete, Monitoring, Prevention and Rehabilitation*, ed. J. Mietz, B. Elsener and R. Polder The Institute of Materials IOM Communications, London, pp. 92 – 103 , 1998

32. Feliu, S., *On-site determination of the polarization resistance in a reinforced concrete beam*, Corrosion Eng., v44, n10, pp. 761-765, 1988

33. Feliu, S., *Polarization resistance measurements in large concrete specimens: mathematical solution for a unidirectional current distribution*, Mat's and structures, v22, pp. 199-205, 1989

34. Feliu, S., *Determining polarization resistance in reinforced concrete slabs*, Corrosion science, v29 n1, pp. 105-113, 1989

35. Feliu, S. and Gonzalez, J.A., *The determination of the corrosion rate of steel in concrete by a non-stationary method*, Corrosion Science, v26, n11, pp. 961-970, 1986

36. Feliu, V., Gonzalez, J.A., Andrade, C., Feliu, S., *Equivalent circuit for modeling the steel-concrete interface. 1. experimental evidence and theoretical predictions*, Corrosion science, v40, n6, pp. 975-993, 1998

37. Federal Highway Administration (FHWA), *Corrosion Costs and Preventive Strategies in the United States*, Report FHWA-RD-01-156, September 2001.

38. Fontana, M.G., Corrosion engineering, McGraw-Hill, 1986

39. Ford, S.J., Shane, J.D. and Mason, T.O., *Assignment of features in impedance spectra of the cement-paste/steel system*, Cement and concrete research, v28, n12, pp. 1737-1751, 1998

40. Francois, R., Arliguie, G., *Effect of microcracking and cracking on the development of corrosion in reinforced concrete members*, Magazine of Concrete research, v51, n2, 1999

41. Gjørve, O. E., Vennesland, ∅., and El-Busaidy, A. H. S., *Diffusion of Dissolved Oxygen Though Concrete*, NACE, Paper No. 17 , 1976

42. Gonzalez, J.A., Feliu, S., Rodriguez, P. Ramirez, E., Alonso, C. and Andrade, C., *Some questions on the corrosion of steel in concrete-part 1: when, how and how much steel corrodes*, Matreials and Structures, v29 Jan-Feb, pp. 40-46, 1996

43. Gonzalez, J.A., Molina, A., Escudero, M.L., Andrade, C., *Errors in the electrochemical evaluation of very small corrosion rates-1. polarization resistance method applied to corrosion of steel in concrete*, Corrosion science, v25, n10, pp. 917-930, 1985

44. Gonzalez, J.A., Molina, A., Escudero, M.L., Andrade, C., *Errors in the electrochemical evaluation of very small corrosion rates-2. other electrochemical techniques applied to corrosion of steel in concrete*, Corrosion Science, v25, n7, pp. 519-530, 1985

45. Gowers, K.R. and Millard, S.G., *Measurement of Concrete Resistivity for Assessment of Corrosion Severity of Steel Using Wenner Technique*, ACI Mat's J., n96, pp. 536-, 1999

46. Gulikers, J., Schlangen, E., *Numerical analysis of galvanic interaction in reinforcement corrosion*, Corrosion of reinforcement in concrete , 1996

47. Jaggi, S., Bohni, H., Elsener, B., *Macrocell corrosion of steel in concrete- experiments and numerical modeling*, Eurocorr 2001, 2001

48. John, D.G., Searson, P.C. and Dawson, J.L., *Use of Impedance technique in studies on steel in concrete in immersed conditions*, British corrosion journal, v16, n2 , pp. 102-106, 1981

49. Jones, D.A., *Principles and prevention of corrosion*, Prentice Hall, 1996

50. Kolluru V. Subramaniam and Mingdong Bi, *CPE Behavior of Steel-Concrete Interface: Experimental Validation*, Corrosion, (in review)

51. Kranc, S.C. and Sagues, A.A., *Detailed modeling of corrosion macrocells on steel reinforcing in concrete*, Corrosion science, v43, pp. 1355-1372, 2001

52. L.L. Shrier, G.T. Burstein, R.A. Jarman, *Corrosion*, Butterworth-Heinemann, 1994

53. Lorentz, T., French, C., *Corrosion of reinforced steel in concrete: effect of mat's, mix composition, and cracking*, ACI Mat's J, v92 , pp. 181-190, 1995

54. Macdonald, D.D., *The point defect model for the passive state*, J of electrochemical society, v139, n12, pp. 3434-3450, 1992

55. Macdonald, D.D., Mckubre, M.C.H. Urquidi-macdonald, M., *Theoretical assessment of AC impedance spectroscopy for detecting corrosion of rebar in reinforced concrete Corrosio*n, v44, n1, pp. 2-7, 1988

56. Macdonald, D.D., Urquidi-macdonald, M., Rocha-Filho, R.C., *Determining polarization resistance of rebar in reinforced concrete*, Corrosion, v47, n5, pp. 330-335, 1991

57. Macdonald, J. Ross , *Impedance Spectroscopy - Emphasizing Solid Materials and Systems*, John Wiley & Sons , 1987

58. Mailvaganam, N.P., and Alexander, T., *selection of repair materials with expert advice*, concrete repair bulletin, pp. 12-15, 1996

59. Martin, H., and Schiessel, P., *The Influence of Cracks on the Corrosion of Steel in Concrete*, Preliminary Report, RILEM International Symposium on the Durability of Concrete, Prague, V. 2., 1969.

60. McCarter, W.J. and Garvin, S, *Dependence of electrical impedance of cement-based materials on their moisture condition*, J. Phys. D: Appl. Phys, v22, pp. 1773-1776, 1989

61. Mingdong Bi and K. Subramaniam, *Corrosion of Steel in Cracked Concrete: Experimental*

Investigation Using External Polarization, the 3rd International Conference on Construction Materials, Canada, 2005

62. Mingdong Bi and K. Subramaniam, *The Corrosion of Steel in Cracked Concrete: Experimental Investigation Using External Polarization*, NACE Corrosion 2006, San Diego, 2006

63. Mohammed, T.U, Hamada, H. and Yamaji, T , *Concrete after 30 years of exposure-part ii: chloride ingress and corrosion of steel bars*, ACI Mat's J, v101, n1, pp. 13-18, 2004

64. Mohammed, T.U, Hamada, H. and Yamaji, T , *Concrete after 30 years of exposure-part I: Mineralogy, Microstructures, and Interfaces*, ACI Mat's J, v101, n1, pp. 3-12, 2004

65. Mohammed, T.U., Otsuki, N., Hamada, H., *Oxygen permeability in cracked concrete reinforcement with plain and deformed bars*, Cement and Concrete Research, v31, pp. 829-834, 2001

66. Mohammed, T.U., Otsuki, N., Hamada, H., Yamaji, T., *Chloride-induced corrosion of steel bars in concrete with the presence of gap at steel-concrete interface*, ACI Mat's J, v99, 2002

67. Monteiro, P.J.M., Morrison, H.F., Frangos, W., *Nondestructive measurement of corrosion state of reinforcing steel in concrete*, ACI Mat's J, v95, n6, pp. 704-709, 1998

68. Montemor, M.F., Simos, A.M.P. and Ferreira, M.G.S., *Chloride-induced corrosion on reinforcing steel: from the fundamentals to the monitoring techniques*, Cement and concrete composites, v25, pp. 491-502 , 2003

69. NACE, *Laboratory corrosion testing of metals for the process industries*, NACE standard TM-01-69 (1976 Version)

70. Olek, J., Martin, F., *Prediction of corrosion rate using electrochemical impedance and electrochemical noise*, Cementing the future

71. Otsuki, N., Miyazato, S., Diola, N.B. and Suzuki, H., *Influences of bending crack and water-cement ratio on chloride-induced corrosion of main reinforcing bars and stirrups*, ACI Mat's J, v97, n4, pp. 454-464, 2000

72. Paulsson-Tralla, J., Silfwerbrand, J., *Estimation of chloride ingress in uncracked and cracked concrete using measured surface concentrations*, ACI Mat's J, v99, n1, pp. 27-36, 2002

73. Payer, J.H., Boyd, W.K., Dippold, D.B. and Fisher, W.H., *NBS EM DASH BATTELLE COST OF CORROSION STUDY (70 BILLION!) EM DASH 1*, Materials Performance, v19, n5, 1980

74. Ping Gu, J.J. Beaudoin, Min-Homg Zhang and V.M. Malhotra, *Performance of reinforcing steel in concrete containing silica fume and blast-furnace slag ponded with sodium chloride solution*, ACI mat's J, v97, n3 , pp. 254-262, 2000

75. Ping Gu, J.J. Beaudoin, Min-Hong Zhang and V.M. Malhotra, *Performance of steel reinforcement in Portland cement an high fly ash concretes exposed to chloride solution*, ACI mat's J, v96, n5,

pp. 551-558, 1999

76. Ping Gu, S. Elliott., R. Hristova, J.J. Beaudoin, R. Brousseau, and B. Balock, *A study of corrosion inhibitor performance in chloride contaminated concrete by electrochemical impedance spectroscopy*, ACI mat's J, v94, n5, pp. 385-395, 1997

77. Princeton applied research, *Basic of Electrochemical impedance spectroscopy*, PAR application notes, AC-1

78. R.W. Revie Editor, *Uhlig's Corrosion Handbook*, Wiley, 2000

79. Raharinaivo, A, Genin, J.M., *Mechanism of chloride actions on steel corrosion in concrete, Fourth international conference of durability of building mat's and components*, Singapore, pp. 575-581, 1987

80. Raharinaivo, A, Guilbaud, J., Chahbazian, G., Derrien, F, *The electrochemical behavior of steel under polarization in porous media simulating concrete*, Corrosion science, v33, 1992

81. Raphael, M., and Shalon, R., *A Study of the Influence of Climate on Corrosion of Reinforcement*, Proceedings, RILEM Symposium on Concrete and Reinforced Concrete in Hot Countries, Building Research Station, Haifa, 1971, pp. 77-96.

82. Raupach, M., *Chloride-induced macrocell corrosion of steel in concrete- theoretical background and practical consequences* , Construction and building mat's, v10, 1996

83. Raupach, M., *Corrosion of steel in the area of cracks in concrete - laboratory tests and calculations using a transmission-line-model*, Corrosion of Reinforcement in Concrete Construction, Edited by C.L. Page, P. Bamforth and J.W. Figg SCI Books from the Royal Society of Chemistry, pp. 13-23, 1996

84. Raupach, M., *Investigations on the influence of oxygen on corrosion of steel in concrete-part 1*, Mat's and structures, v29, pp. 174-184, 1996

85. Sagues, A.A., *Electrochemical impedance of corrosion macrocells on reinforcing steel in concrete*, Corrosion 90, No. 132, 1990

86. Sagues, A.A. and Kranc, S.C. *On the Determination of Polarization Diagrams of Reinforcing Steel in Concrete*, Corrosion, v48, pp. 624-633, 1992

87. Sagues, A.A. and Kranc, S.C., *Computer modeling of effect of corrosion macrocells on measurement of corrosion rate of reinforcing steel in concrete, Techniques to access the corrosion activity of steel reinforced concrete structures*, ASTM STP 1276 , pp. 58-73, 1996

88. Sagues, A.A., Pech-Canul, M.A., Shaid, A.K.M., *Corrosion macrocell behavior of reinforcing steel in partially submerged concrete columns*, Corrosion science, v45, pp. 7-32, 2003

89. Schiessl, P., *Corrosion of steel in concrete--report of the technical committee 60-CSC RILEM*, Chapman and Hall, 1989

90. Schiessl, P., Raupach, M , *Laboratory studies and calculations on the influence of crack width on chloride-induced corrosion of steel in concrete*, ACI mat's J, v94, n1, pp. 56-62, 1997

91. Stern, M., Geary, A.L., *Electrochemical polarization, 1. A theoretical analysis of the shape of polarization curves*, J of electrochemical society, v104, n1, pp. 56-63, 1957

92. Stratfull JR, Corrosion NACE, 13, 173t , 1957

93. Transportation research board special report 235, *Highway deicing: comparing salt and calcium magnesium acetate*, Transportation Research Board, National research council, Washington DC, 1991

94. Tremper, B., *The Corrosion of Reinforcing Steel in Cracked Concrete*, ACI JOURNAL, Proceedings V. 43, No. 10, June 1947, pp. 1137-1144.

95. Tuutti, K. , *Corrosion of steel in concrete*, Swedish cement and concrete research institute, 1982

96. U.S. Department of transportation , *Corrosion detection in reinforced concrete bridge structure, user manual*, U.S. Department of transportation, Federal highway administration, Demonstration project No.84 , 1992

97. Uhlig, H.H. and Revie, R., *Corrosion and corrosion control: an introduction to corrosion science and engineering*, John wiley & sons, pp. 74, 1985

98. V. S. Ramachandran, and James J. Beaudoin, *Handbook of analytical techniques in concrete science and technology*, WILLIAM ANDREW PUBLISHING, LLC, 2001

99. Vesikari, E., *Service life of concrete structures with regards to corrosion of reinforcement*, VTT research report 553, Technical research center of Finland, 1988

100. Zhang, J.Y., Monteiro, P.J.M. and Morrison, H.F., *Noninvasive surface measurement of corrosion impedance of reinforcing bar in concrete-part 2: Forward modeling*, ACI Mat's J, v99, n3, pp. 242-249, 2002

101. Zhang, J.Y., Monteiro, P.J.M., Morrison, H.F., *Noninvasive surface measurement of corrosion impedance of reinforcing bar in concrete-part 1: experimental results*, ACI Mat's J, v98, n2, pp. 116-125, 2001